Université Joseph Fourier - Grenoble

Thèse

pour obtenir le grade de

Docteur de l'Université Joseph Fourier

Physique

preséntée et soutenue publiquement par

Roberta ANGELINI

Study of the high frequency dynamics in hydrogen bonded liquid systems by inelastic x-rays scattering: the case of hydrogen fluoride and $(HF)_x(H_2O)_{1-x}$ solutions

Date de soutenance: 19 Juin 2003

Composition du Jury

C. Alba-Simionesco

M. C. Bellissent-Funel

J. F. Legrand

G. Ruocco

F. Sette

G. Viliani

Thèse préparée au sein du laboratoire: European Synchrotron Radiation Facility-Grenoble

A Caterina, Remo e Vittorio,
la mia famiglia

Contents

Introduction **4**

1 Scattering methods to measure atomic density fluctuations **9**

1.1 Introduction 9

1.2 X-rays and light scattering cross sections 10

1.3 X-rays and neutrons: a comparison 18

1.3.1 Inelastic X-rays (IXS) and neutrons (INS) cross sections 18

1.3.2 Kinematics in the (Q, ω) plane for X-rays and neutrons 21

1.3.3 Summary on the peculiarity of the IXS method 24

2 The inelastic X-rays scattering method 27

2.1 Introduction 27

2.2 Basic ideas 28

2.2.1 The triple axis spectrometer 28

2.2.2 High order reflections from perfect crystals 30

2.2.3 Backscattering geometry 33

2.3 Characteristics of the beamline ID16 at the ESRF 36

3 Collective dynamics of liquid systems **44**

3.1 Introduction 44

3.2 Basic definitions 45

3.3 Hydrodynamics 50

3.4 Generalized hydrodynamics 52

3.5 Memory function formalism 53

3.5.1 Continued fraction representation 55

3.5.2 Memory function and density fluctuations . . . 57
3.5.3 Memory function and relaxation processes . . . 59
3.5.4 Damped Harmonic Oscillator (DHO) model . . . 64
3.5.5 Viscoelastic model . . . 65

4 Collective dynamics in hydrogen bonded liquid systems 69
4.1 Introduction . . . 69
4.2 Hydrogen bonded systems . . . 70
4.3 The water case: a recall . . . 72
4.4 The hydrogen fluoride (HF) case: open questions . . . 75

5 Sample environment and experimental set-up 78
5.1 Introduction . . . 78
5.2 Sample environment . . . 78
5.3 Experimental resolutions . . . 86
5.4 Empty cell measurements . . . 87

6 Study of the collective dynamics in HF and $(HF)_x$ $(H_2O)_{1-x}$ solutions 91
6.1 Introduction . . . 91
6.2 Study of the dynamic structure factor of HF by Brillouin light scattering . 92
6.2.1 Experimental data . . . 93
6.2.2 Data reduction: adiabatic sound velocity and kinematic longitudinal viscosity . . . 94
6.3 Study of the high frequency collective dynamics of HF by inelastic x-ray scattering . . . 98
6.3.1 Experimental data as a function of Q and T . . . 99
6.3.2 DHO analysis . . . 99
6.3.3 Viscoelastic analysis . . . 103
6.3.4 Conclusions . . . 113
6.4 Study of the high frequency collective dynamics of $(HF)_x(H_2O)_{1-x}$ by inelastic x-ray scattering . . . 114
6.4.1 Experimental data as a function of Q and concentration . . . 114
6.4.2 DHO analysis . . . 114
6.4.3 Viscoelastic analysis . . . 121

6.4.4 Conclusions 125

Conclusions **128**

Appendix1 **131**

Appendix2 **144**

Aknowledgments **152**

Introduction

The high frequency dynamics of many liquid systems is investigated experimentally by inelastic neutron scattering (INS) and inelastic X-rays scattering (IXS), and numerically by molecular dynamic simulations (MD). A big effort is devoted to understand how the dynamic properties of different liquids depend on the characteristic inter-particle interaction potential of the system under study. In this respect particular attention has been paid to noble gases and liquid metals. The inter-particle interactions for the former are usually modeled by Lennard-Jones potentials whereas the latter are represented in terms of pseudo-potentials. Another very important class of liquids to consider are the hydrogen bonded (HB) liquids. The interest is found in the strong influence that hydrogen bond has on the liquid microscopic properties. In fact they are characterized by a highly directional inter-particle interaction due to the hydrogen bond. In this respect one of the most investigated HB liquid system is water which has been extensively studied by both scattering experiments and molecular dynamic simulations. Besides water, many other liquid systems of organic and inorganic nature are characterized by hydrogen bonding, their structural and dynamic properties are strongly influenced by the strength and the number of the hydrogen bonds between nearest neighbour molecules. Aiming to establish a connection between the dynamical properties of these systems and the specific HB arrangement, in the present work we exploit the IXS technique to make a comparative study of water and other HB liquids. We focus our attention on the relaxation phenomena marking the dynamic of density fluctuations. In particular we deal with the structural and microscopic relaxation processes: the first is related to the structural rearrangements of the particles and takes place with a characteristic time scale τ_α dictated by the local inter-particle interaction and the thermodynamic state; the second is associated with the interactions between an atom and the cage of its nearest neighbours and is dictated by the topological disorder existing in both liquid and glassy phases.

Several open questions are related to the structural relaxation:

- The first concerns the *time scale* of the relaxation: it has been found that in water, in the $\approx 350 - 490\ K$ temperature range [1], the relaxation time associated to the structural process lies in the sub-picosecond region. This is the same order of magnitude of the lifetime of the H-bond. *Is the structural relaxation time in hydrogen bonded liquid systems related to the lifetime of the H-bond ?*

- The second question concerns the *strength* of the relaxation: it depends on the specific system and is related to the interaction potential between molecules. *How does the specific inter molecular interactions and local arrangements affect the strength of the relaxation in HB liquids ?*

- The third question concerns the *activation energy* of this process: *is the activation energy of the structural relaxation related to the activation energy necessary to make and break H-bonds?*

Another important point concerns the presence of the microscopic relaxation process. In simple monatomic liquids both kinetic and mode-coupling theories predict the existence of two distinct relaxation processes [2]. In these theories, as shown both by numerical simulations [3, 4] and by experiments [5], one of the two processes is the structural or $\alpha-$relaxation, and the other is the microscopic or $\mu-$ relaxation. In glass-forming systems, one also finds the same relaxation processes pattern. In this case, by driving the system to the glassy state, where the structural arrest freezes the α-process and τ_α becomes extremely large, is still possible to clearly observe the microscopic process [6]. The outlined scenario seems to point out that these two relaxation processes are universal features of the liquid state even if information on the important class of hydrogen bonded liquids is still missing. In this respect a question needs to be answered:

- *Are both the structural and microscopic relaxation process present also in hydrogen bonded liquid systems?*

Aiming to clarify all these aspects concerning the high frequency dynamics of hydrogen bonded liquids, we have chosen pure hydrogen fluoride (HF), the inorganic system with the strongest hydrogen bond and $(HF)_x(H_2O)_{1-x}$ solutions. The main difference between

HF and H_2O is the uni-dimensional vs. three-dimensional nature of the HB network. Consequently is of great interest to determine the evolution of the collective dynamics from the phenomenology of one liquid to that of the other.

The thesis is structured as follow:

In **Chapter 1** the inelastic x-ray scattering (IXS) with meV energy resolution and light scattering techniques are introduced. They allow to determine experimentally the dynamic structure factor $S(Q,\omega)$, which is the time and space Fourier transform of the correlation function for the particle density fluctuations of the investigated system. IXS is a powerful method to investigate the high frequency collective dynamics in the mesoscopic region, *i.e.* for distances comparable to those of first neighbours. Light scattering is a method used to probe the dynamics of density fluctuations under quasi-macroscopic conditions. It yields similar results to x-rays and neutrons scattering but in a substancially lower momentum transfer and frequency regions. In particular we derive the expressions for the inelastic x-ray and light scattering differential cross section, $\partial^2\sigma/\partial\Omega\partial\omega$ and its relation to the dynamic structure factor $S(Q,\omega)$. Finally a comparison between IXS and INS is done, underlining similarities, differences and complementarities of the two technique.

In **Chapter 2** we describe the very high resolution IXS spectrometer at the European Synchrotron Radiation Facility (ESRF) in Grenoble. This is the beam-line ID16 which provides a spectrometer with a meV energy. It is based on the principle of the triple axis spectrometer and allows to perform experiments with an energy resolution down to 1.5 meV with incident photons of 21748 eV energy. The method used to obtain highly monochromatic X-rays is discussed, it is based on the Bragg diffraction and requires: i) the use of high orders Bragg reflections from perfect crystals; ii) the use of nearly backscattering geometry for these reflections. The working principle of the spectrometer and the fundamental concepts behind the beamline construction, as the intrinsic resolving power for silicon crystals and the backscattering geometry are illustrated. The characteristics of the main optical elements of ID16 are described together with the general performances of this beamline.

Chapter 3 is devoted to the description of the collective dynamics in liquid systems Its aim is to remind the basic concepts and the basic equations which will be exploited to analyse and interpret the experimental data presented in this thesis. The basic analytical tools used to describe the dynamics of density fluctuations are introduced. A discussion on the main theoretical approaches to study the dynamics in different regions of the (Q,ω)

plane are presented. In particular we consider: i) the macroscopic hydrodynamic region where the system is viewed as a continuum isotropic medium and the excitation spectrum is well described within the Navier-Stokes hydrodynamic equations; ii) the mesoscopic region in which the momentum transfer becomes comparable to the inter-particle distance and the spectrum of density fluctuations is described within the framework of generalized hydrodynamics. Finally a qualitative and quantitative description of the relaxation processes in a liquid is given and the models that are used to fit our data are introduced.
Chapter 4 is dedicated to the description of the collective dynamics in hydrogen bonded liquid systems. In particular a general introduction to this class of systems together with their main properties is reported. We start giving a brief report on the most studied HB liquid system, water, summarizing the previous studies on its collective dynamics. We introduce the two HB liquids subject of the investigations of this thesis work, hydrogen fluoride (HF) and $(HF)_x(H_2O)_{1-x}$ solutions.
Chapter 5 is devoted to the description of all the experimental aspects related to the measurements of the dynamic structure factor of pure hydrogen fluoride (HF) and $(HF)_x(H_2O)_{1-x}$ solutions. The design and development of the sample cells as well as each part of the assembly and the sample preparation are described in details. The measurements of the instrumental energy resolutions together with the "empty cell" measurements, namely, the contribution to the total scattered intensity due to the sample cells, are presented.
In **Chapter 6** the experimental results obtained by studying the dynamic structure factor $S(Q,\omega)$ of the two HB liquid systems subject of this thesis work: HF and $(HF)_x(H_2O)_{1-x}$ solutions are reported. In order to characterize the transition from the hydrodynamic macroscopic regime probed by Brillouin light scattering, to the mesoscopic regime probed by inelastic X-rays scattering, the collective dynamics of HF is investigated with these two different techniques. Aiming to shed light on the behaviour of the collective dynamics of high associated liquids, we compare these results with the one existing on water. Then, since the main difference between HF and H_2O lies in the different HB arrangement, the collective dynamics of $(HF)_x(H_2O)_{1-x}$ solutions is investigated by IXS to describe the passage from the behaviour of one liquid to the other.

Chapitre 1

Dans ce chapitre, nous introduisons la diffusion inélastique des rayons X et la diffusion Brillouin de la lumière. Avec ces deux techniques on peut accéder expérimentalement au facteur de structure dynamique $S(Q,\omega)$ associé aux fluctuations de densité des particules du système exploré. Nous verrons comment la diffusion inélastique de rayons X, avec une très haute résolution en énergie, peut s'appliquer à l'étude de la région cinématique correspondant aux fluctuations de densité atomique. La diffusion Brillouin de la lumière est utilisée pour explorer la dynamique des fluctuations de densité en condition quasi-macroscopique. Elle donne des résultats très similaires au rayons X mais dans une région à plus bas moment échangé et à plus basses fréquences. Le chapitre est organisé comme suit:

dans le Par. 1.2 nous décrivons les équations de base qui lient la section efficace de diffusion de rayons X et de lumière au facteur de structure dynamique.

Dans le Par 1.3 les différentes régions du plan (Q,ω) accessible par les rayons X et les neutrons seront illustrées afin de mettre en évidence la complémentarité de ces deux techniques pour l'étude de la dynamique aux hautes fréquences dans les systèmes désordonnés. Enfin nous discuterons les principaux avantages et désavantages de cette nouvelle technique, et aussi les conditions particulières qui on permis son développement.

Chapter 1

Scattering methods to measure atomic density fluctuations

1.1 Introduction

In this Chapter the inelastic x-ray scattering (IXS) with meV energy resolution and light scattering are introduced. With these techniques it is possible to determine experimentally the dynamic structure factor $S(Q, \omega)$, which is the time and space Fourier transform of the correlation function for the particle density fluctuations in the investigated system.

IXS is a powerful method to investigate the high frequency collective dynamics in liquids and disordered systems. Traditionally the study of the atomic motion in condensed matter in this high frequency region has been the domain of inelastic neutron scattering (INS) in fact neutrons are particularly suited to these studies mainly for two reasons:

- neutrons with wavelengths comparable to the interparticle spacing have kinetic energy of $\cong 100\ meV$, and therefore, with moderate relative energy resolution, it is possible to study efficiently the collective atomic excitations.
- they scatter from the nuclei with an interaction strength sufficiently small to allow a large penetration in most materials;

The INS technique has been successfully applied to the study of the density fluctuations spectrum of crystalline solids and low density gases. In disordered systems, like liquids, glasses and dense gases, very few neutrons studies have been performed so far. In fact,

due to the kinematics of the scattering process, the neutron technique cannot be efficiently applied to study sound modes in materials with a large speed of sound, typically above 1500 m/s. These kinematics limitations do not apply to x-rays which are, therefore, particularly well suited to study the small momentum and large energy transfer regions.

Light scattering is a method used to probe the dynamics of density fluctuations under quasi-macroscopic conditions. It yields similar results to x-rays and neutrons scattering but in the low momentum transfer and low frequency region. The chapter is structured as follow:

in **Sec. 1.2** we derive the expressions for the inelastic x-ray and light scattering differential cross section, $\partial^2\sigma/\partial\Omega\partial\omega$. It is shown how they are related to the dynamic structure factor $S(Q,\omega)$.

In **Sec. 1.3** a comparison between IXS and INS is done, underlining similarities and main differences. i) The coherent and incoherent cross sections in the cases of INS and IXS are compared. ii) The kinematics of the scattering process, that determine different accessible regions of the (Q,ω) plane in the case of neutrons or x-rays, is illustrated. The complementarity between the two techniques is also highlighted. iii) The peculiarities of the IXS technique with meV energy resolution are summarized together with the particular conditions that have allowed the development of IXS.

1.2 X-rays and light scattering cross sections

The kinematics of an inelastic x-ray scattering process is illustrated in Figure 1.1. A photon with an initial energy $\hbar\omega_0$, a wave vector $\mathbf{k}_0$, and a polarization ϵ_0, impinging upon a target, S, is scattered in the solid angle $d\Omega$, centered on the scattering angle θ. The scattered photon will have a final energy $\hbar\omega_1$, a wave vector $\mathbf{k}_1$, and a polarization ϵ_1. From the energy-momentum conservation law, the energy, $\hbar\omega$, and momentum, $\mathbf{Q}$, transfered to the scattering system are $\hbar\omega = \hbar\omega_0 - \hbar\omega_1$ and $\mathbf{Q} = \mathbf{k}_0 - \mathbf{k}_1$.

When $\omega << \omega_0$ the wave vectors $\mathbf{k}_0$ and $\mathbf{k}_1$ have basically the same modulus and, as a consequence, the momentum transfer is simply connected to the scattering angle θ by the relation $Q = 2k_0 sin(\theta/2)$. The scattered intensity is determined by the scattering *double differential cross section* $\partial^2\sigma/\partial\Omega\partial\omega_1$, which determines the number of scattered photons into a solid angle $d\Omega$ around the direction defined by $\mathbf{k}_1$, with a frequency ω_1 in the range $d\Omega_1$.

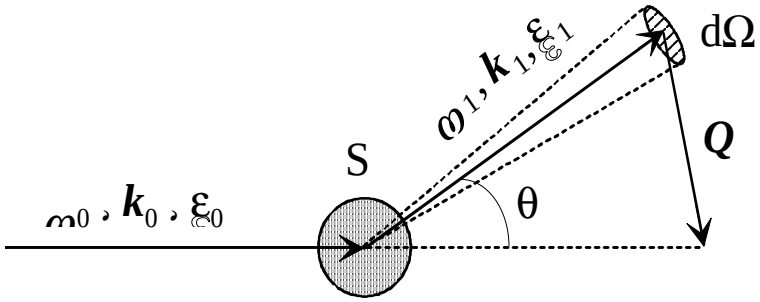

Figure 1.1. Principle of an inelastic x-ray and light scattering experiment.

Inelastic X-rays scattering cross section

The cross section, function of the energy and momentum transfer to the scattering system, can be calculated by considering the interaction Hamiltonian H_i which couples the electromagnetic field of the photon to the scattering electrons of the target. In the weak relativistic limit, H_i can be written as the sum of 4 terms [7].

$$H_i = \frac{e^2}{2m_e c^2}\sum_j \mathbf{A}(\mathbf{r_j},t)\cdot\mathbf{A}^*(\mathbf{r}_j,t) - \frac{e}{m_e c}\sum_i \mathbf{A}(\mathbf{r_j},t)\cdot\mathbf{p_j} - \frac{e}{m_e c}\sum_j \mathbf{s_j}\cdot(\bigtriangledown\times\mathbf{A}(\mathbf{r_j},t))$$

$$-\frac{e^2}{2m_e^2 c^4}\sum_j \mathbf{s_j}\cdot(\dot{\mathbf{A}}(\mathbf{r_j},t)\times\mathbf{A}(\mathbf{r_j},t)) \qquad (1.1)$$

Here the sum is over the electrons of the scattering system, e and m_e are respectively the charge and the mass of the electron, c is the speed of light, $\mathbf{p}$ is the momentum operator of the scattering electron, $\mathbf{s}$ is the electron spin operator, and $\mathbf{A}$ is the vector potential of the electromagnetic field. The first two terms of 1.1 do not depend on the electron spin and are respectively the Thomson term and the absorption term. They describe the coupling between the electron current and the electric photon field. The other two describe the coupling of the electron spin with the magnetic photon field, and the spin-orbit interaction in presence of the electromagnetic field. These last two terms are much weaker than the first two for photon energies lower than the rest energy of the electron ($m_e c^2$). Assuming the validity of the linear response theory, in which a weak coupling between the beam and the system is considered, the scattering double differential cross

section does not depend on the intensity of the incident flux, and the intrinsic properties of the sample are probed as if it was unperturbed [2].

- Using the lowest-order perturbation theory, in the hypothesis that the initial and final photon states are represented by plane waves,
- Calculating the transition probability per unit of time by the *Fermi golden rule*

the cross section can be expressed as [7]:

$$\frac{\partial^2\sigma}{\partial\Omega\partial\omega_1} = r_e^2\left(\frac{\omega_1}{\omega_0}\right)\sum_{I,F}\Big|\langle\Phi_F|\sum_j e^{iQ\cdot r_j}|\Phi_I\rangle(\epsilon_\mathbf{0}\cdot\epsilon_\mathbf{1}) - i\frac{\hbar\omega}{m_e c^2}\langle\Phi_F|\sum_j e^{iQr_j}\mathbf{s_j}|\Phi_I\rangle(\epsilon_\mathbf{1}\times\epsilon_\mathbf{0}) + \frac{1}{m_e}$$

$$\sum_N\Bigg\{\frac{\langle\Phi_F|\sum_j[\epsilon_\mathbf{1}\cdot\mathbf{p_j} - i(\mathbf{k_1}\times\epsilon_\mathbf{1})\cdot\mathbf{s_j}]e^{-i\mathbf{k_1}\cdot\mathbf{r_j}}|\Phi_N\rangle\langle\Phi_N|\sum_j[(\epsilon_\mathbf{0}\cdot\mathbf{p_j}) + i(\mathbf{k_0}\times\epsilon_\mathbf{0})\cdot\mathbf{s_j}]e^{i\mathbf{k_0}\cdot\mathbf{r_j}}|\Phi_I\rangle}{E_I - E_N + \hbar\omega_0 - i\Gamma_N/2}$$

$$+\frac{\langle\Phi_F|\sum_j[\epsilon_\mathbf{0}\cdot\mathbf{p_j} + i(\mathbf{k_0}\times\epsilon_\mathbf{0})\cdot\mathbf{s_j}]e^{-i\mathbf{k_0}\mathbf{r_j}}|\Phi_N\rangle\langle\Phi_N|\sum_j[\epsilon_\mathbf{1}\cdot\mathbf{p_j} - i(\mathbf{k_1}\times\epsilon_\mathbf{1})\cdot\mathbf{s_j}]e^{-i\mathbf{k_1}\cdot\mathbf{r_j}}|\Phi_I\rangle}{E_I - E_N - \hbar\omega_1}\Bigg\}\Bigg|^2$$

$$\times\delta(E_F - E_I - \hbar\omega) \tag{1.2}$$

where $r_e = e^2/m_e c^2 = 2.818\cdot 10^{-15}m$ is the classical electron radius, $|\Phi_N>$ is the wave-function which describes a general (intermediate) state for the scattering electron system with energy E_N , and Γ_N takes into account the level width, it is proportional to the inverse of the lifetime of the state $|\Phi_N>$, $\epsilon_\mathbf{0}$ and $\epsilon_\mathbf{1}$ are the unit polarization vectors, E_I is the energy of the initial state. Using the closure relation $\sum_N|\Phi_N><\Phi_N| = I$ and considering that if the incident energy $\hbar\omega_0$ is much larger than E_I it is possible to neglect $E_N - E_I$ in the two denominators and the expression 1.2 is reduced to [7]:

$$\frac{\partial^2\sigma}{\partial\Omega\partial\omega_1} = r_e^2\left(\frac{\omega_1}{\omega_0}\right)\sum_{I,F}\left|\langle\Phi_F|\sum_j e^{iQr_j}|\Phi_I\rangle(\epsilon_\mathbf{0}\cdot\epsilon_\mathbf{1}) - i\frac{\hbar\omega}{m_e c^2}\langle\Phi_F|\sum_j e^{iQr_j}\left(i\frac{\mathbf{Q}\times\mathbf{P_j}}{\mathbf{k_0}^2}\cdot\mathbf{C} + \mathbf{s_j}\cdot\mathbf{D}\right)|\Phi_I\rangle\right|^2$$

$$\times\delta(E_F - E_I - \hbar\omega) \tag{1.3}$$

where

$C = \epsilon_\mathbf{0} \times \epsilon_\mathbf{1}$
$D = (\epsilon_\mathbf{0} \times \epsilon_\mathbf{1}) + (\hat{\mathbf{k}_1} \times \epsilon_\mathbf{1})(\hat{\mathbf{k}_0} \times \epsilon_\mathbf{0}) - (\hat{\mathbf{k}_0} \times \epsilon_\mathbf{1})(\hat{\mathbf{k}_1} \times \epsilon_\mathbf{1}) \times (\hat{\mathbf{k}_0} \times \epsilon_\mathbf{0})$
$\mathbf{Q} = \mathbf{k}_1 - \mathbf{k}_0$
Here $\hat{k_0}$ and $\hat{k_1}$ represent the unit vectors of the incident and scattered photon respectively. The first term of 1.3 is due to pure charge Thomson scattering, and the latter is due to the the magnetic scattering. This latter one is reduced by a factor $(\hbar\omega/m_e c^2)^2$ in amplitude with respect to the Thomson term. Being $m_e c^2 \approx 0.5 MeV$, at photon energies of the order of 10 keV, $(\hbar\omega/mc^2)^2 \approx 10^{-4}$ and the magnetic scattering is strongly suppressed. For x-rays in the energy range of $10-20$ keV, neglecting the magnetic term and away from absorption edge, the scattering cross section reduces to the following simple expression:

$$\frac{\partial^2\sigma}{\partial\Omega\partial\omega_1} = r_e^2\left(\frac{\omega_1}{\omega_0}\right)(\epsilon_\mathbf{0}\cdot\epsilon_\mathbf{1})^2 \sum_{I,F} p_I \left|\langle\Phi_F|\sum_j e^{i\mathbf{Q}\cdot\mathbf{r_j}}|\Phi_I\rangle\right|^2 \times \delta(E_F - E_I - \hbar\omega) \tag{1.4}$$

where p_I is the statistical weight of the initial state $|\Phi_I>$.Using the integral representation of the δ function, the Van Hove transformation [8, 9]and the relation [8]:

$$\left(\frac{d\sigma}{d\Omega}\right)_{th} = r_e^2\left(\frac{\omega_1}{\omega_0}\right)(\epsilon_\mathbf{0}\cdot\epsilon_\mathbf{1})^2 \tag{1.5}$$

the double differential cross section can be rewritten as:

$$\frac{\partial^2\sigma}{\partial\Omega\partial\omega_1} = \left(\frac{d\sigma}{d\Omega}\right)_{th}\frac{1}{2\pi}\int\sum_{l,l'} < e^{-iQ\cdot r_l(t)}e^{iQ\cdot r_l(0)} > e^{-i\omega t}dt \tag{1.6}$$

The integral representation is used to highlight that the cross section can be expressed as the time evolution of ground state properties and in fact, it corresponds to the Fourier transform in space and time of the electron-electron pair correlation function. This quantity is by definition the dynamic structure factor of the electron density, $S(Q,\omega)$:

$$S(Q,\omega) = \int\sum_{l,l'} < e^{-iQ\cdot r_l(t)}e^{iQ\cdot r_l(0)} > e^{-i\omega t} \tag{1.7}$$

The quantity $(\frac{d\sigma}{d\Omega})_{th}$ represents the coupling of the beam to the scattering system and does not depend on the detailed properties of the scattering system. It is possible to reduce further the expression 1.4, and to derive a relation where, instead of the electron-electron pair correlation function, one has directly the dynamic structure factor associated to the atomic motion. This is possible within the validity of the following two assumptions:

- The validity of the adiabatic or Born-Oppenheimer approximation. It assumes that electronic velocities are much greater than ionic velocities; one therefore assumes that because ions move so slowly compared to electrons, at any moment electrons are in their ground state for that particular instantaneous ionic configuration. This allows to separate the electronic and the ionic motion. This means that the wavefunction Φ that describes the *ensemble* ions plus electrons of our target can be factorized in the product of a wavefunction ϕ describing the ions states depending on the nuclear coordinates and a wavefunction ψ describing the electrons states which depend only parametrically from the nuclear coordinates. For a monoatomic system we then assume that the initial and final states can be written as:

$$\begin{aligned}\Phi_I &= \phi_{I_N}(\mathbf{R_1},\ldots,\mathbf{R_N})\cdot\psi_{I_e}(\mathbf{r_1^1},\ldots,\mathbf{r_z^1}\ldots\mathbf{r_1^N},\ldots,\mathbf{r_z^N})\\ \Phi_F &= \phi_{F_N}(\mathbf{R_1},\ldots,\mathbf{R_N})\cdot\psi_{F_e}(\mathbf{r_1^1},\ldots,\mathbf{r_z^1}\ldots\mathbf{r_1^N},\ldots,\mathbf{r_z^N})\end{aligned} \tag{1.8}$$

  where $\mathbf{R}$ and $\mathbf{r}$ are respectively the ions and electrons position vectors, N and Z the ions and the electrons numbers, $\phi_{I_N}(\mathbf{R_1},\ldots,\mathbf{R_N})$, $\phi_{F_N}(\mathbf{R_1},\ldots,\mathbf{R_N})$ the ions wavefunctions, and finally $\psi_{I_N}(\mathbf{r_1^1},\ldots,\mathbf{r_z^1}\ldots\mathbf{r_1^N},\ldots,\mathbf{r_z^N})$, $\psi_{F_N}(\mathbf{r_1^1},\ldots,\mathbf{r_z^1}\ldots\mathbf{r_1^N},\ldots,\mathbf{r_z^N})$ are the wavefunctions of the electrons on the nth atom. This approximation neglects any interaction between electrons of different atoms, and between electrons of one atom with the nucleus of another atom. This approximation is particularly good as far as the energy transfers are small with respect to the electron excitation energies, and therefore it assumes implicitly that the valence electrons with small binding energies are few compared to the core electrons, assumption valid in most cases.

- The scattering process does not lead to electronic excitations; this means that the difference between initial and final state concerns only excitations related to atomic density fluctuations.

The double differential scattering cross section, under these hypotheses, can be written as:

$$\frac{\partial^2\sigma}{\partial\Omega\partial\omega_1} = r_e^2\left(\frac{\omega_1}{\omega_0}\right)(\epsilon_0\cdot\epsilon_1)^2\sum_{F_N I_N} p_{I_N}\left|<\phi_{F_N}|\sum_l f_l(Q)e^{-iQ\cdot R_l}|\phi_{I_N}>\right|^2\delta(E_F-E_i-\omega)$$

$$= r_e^2\left(\frac{\omega_1}{\omega_0}\right)(\epsilon_0\cdot\epsilon_1)^2|f(Q)|^2\frac{1}{2\pi}\frac{1}{N}\int dt e^{-i\omega t}\sum_{l,l'}<e^{-iQR_l(t)}e^{-iQR_{l'}(0)}>$$

$$\boxed{\frac{\partial^2\sigma}{\partial\Omega\partial\omega_1} = r_e^2\left(\frac{\omega_1}{\omega_0}\right)(\epsilon_0\cdot\epsilon_1)^2|f(Q)|^2 S(Q,\omega)} \tag{1.9}$$

where $f_l(Q)$ corresponds to the integral on the electron coordinates of the l^{th} atom. This quantity is the Fourier transform of the electronic charge spatial distribution on the considered atom. It is in fact given by:

$$f_l(Q) = \int \psi_l(\mathbf{r_1}\ldots\mathbf{r_z})\psi_l^*(\mathbf{r_1}\ldots\mathbf{r_z})\sum_{i=1}^{z} e^{iQ\cdot r_i} d\mathbf{r_1}\ldots d\mathbf{r_z} \tag{1.10}$$

and is called the atomic scattering amplitude or *atomic form factor* of the l^{th} atom. The quantity $|\phi_{I_N}>$ denotes the ground state of the ions system, and the $S(Q,\omega)$ in 1.9 is the dynamic structure factor of the ions, i.e. it refers to the atomic density fluctuations only. In the limit $Q\to 0$, $f_l(Q)$ is the number of electrons, Z, of the l^{th} atom, and when Q increases $f_l(Q)$ decreases almost exponentially, thus strongly reducing the inelastic scattering intensity: its decay is determined at large Q predominantly by the Fourier transform of the inner shell atomic wave function which have an exponential envelope. If Q is comparable to the inverse of the interparticle separation, and ω is in the range of phonon excitations energies, it is possible, as shown by Eq. 1.9, to get information concerning the scattering by collective atomic excitations. The Eq. 1.9, derived for a monoatomic system, can be generalized to molecular or crystalline systems. Beside the hypothesis that one can neglect the electronic excitations, if one can neglect also the excitations of other characteristic internal degrees of freedom in the molecule or in the unit cell, (molecular vibrations, for example) because they are at energies much larger than those associated to the considered atomic collective density fluctuations, it is possible to substitute the

atomic scattering amplitude with the molecular or unit cell form factor. In the case of polyatomic non crystalline samples the procedure to determine the scattering cross section is obviously more complicated. The formalism introduced can be easily generalized in the hypothesis of a random distribution of scattering units. In this case one can show that the cross section is splitted into two components: one *coherent* and the other one *incoherent*. They are weighted respectively by the average and by the variance of the fluctuations of the average form factor. In the approximation of a random atomic distribution, the inelastic x-ray cross section can then be re-written as:

$$\frac{\partial^2\sigma}{\partial\Omega\partial\omega_1} = r_e^2\left(\frac{\omega_1}{\omega_0}\right)(\epsilon_0\cdot\epsilon_1)^2[\sigma_c S(Q,\omega)+\sigma_i S_S(Q,\omega)] \tag{1.11}$$

where $\sigma_c =< f(Q) >^2$, $\sigma_i =< f(Q)^2 > - < f(Q) >^2$. Here the calculation of the mean values of $< f(Q) >$ and $< f(Q) >^2$ are made over the whole system. $S_S(Q,\omega)$ is the spectrum of the single particle correlation dynamics and concerns the incoherent part of the scattering cross section. It is defined by:

$$S_S(Q\omega) = \frac{1}{2\pi}\int dt e^{-i\omega t}\sum_l < e^{-iQr_l(t)}e^{-iQr_l(0)} > \tag{1.12}$$

The equation 1.11 is the basic expression to be used in the inelastic x-ray scattering from atomic density fluctuations. As we will see in the next paragraph, this expression is formally identical to the inelastic neutron scattering cross-section. The parameters σ_c and σ_i , however, have slightly different origin, and therefore different values and Q-dependence. From these differences arises the complementarity between these two techniques.

Light scattering cross section

While x-rays interact with electrons, light is sensitive to those collective excitations which are correlated with a change of polarizability. Also in this case the double differential cross section is achieved by applying the time dependent perturbation theory to the interaction hamiltonian H_i of equation 1.1. In this case the time dependent perturbation theory together with the application of the dipole approximation (valid when the wavelength of the incident radiation is much bigger than the interatomic distance $\lambda \gg l$) yields the following expression [2]:

$$\frac{\partial^2\sigma}{\partial\omega\partial\omega} = \frac{\omega_0\omega_1^3}{2N\pi c^4}\sum_{\alpha\beta\gamma\delta} e_i^\alpha e_f^\beta (e_0^\gamma)^*(e_1^\delta)^* \int_{-\infty}^{+\infty} < P_{\alpha\beta}(\mathbf{Q},t)P^*_{\gamma\delta}(\mathbf{Q},0) > e^{i\omega t}dt \tag{1.13}$$

where c is the speed of light, $\mathbf{Q} = \mathbf{k}_1 - \mathbf{k}_0$, its modulus is

$$Q = \frac{4\pi n}{\lambda} sin\frac{\theta}{2}$$

n is the refractive index and λ the wavelength of the incident radiation, $P_{\alpha\beta}(\mathbf{Q},t)$ is the space Fourier transform of the total polarizability tensor $P_{\alpha\beta}(\mathbf{r},t)$:

$$P_{\alpha\beta}(\mathbf{Q},t) = \int P_{\alpha\beta}(\mathbf{r},t)e^{-i\mathbf{Q}\cdot\mathbf{r}}d\mathbf{r} = \int\left(\sum_{l=1}^{N}\alpha^l_{\alpha\beta}(R_l(t))\delta(\mathbf{r}-\mathbf{R}_l(t))\right)e^{-i\mathbf{Q}\cdot\mathbf{r}}d\mathbf{r}$$

$$= \sum_{l=1}^{N}\alpha^l_{\alpha\beta}(\mathbf{R}_l(t))e^{-i\mathbf{Q}\cdot\mathbf{R}_l(t)}$$

here $\alpha^l_{\alpha\beta}(\mathbf{R}_l(t))_{l=1...N}$ is the effective polarizability tensor of the lth molecule. It depends on the position $R_l(t)$ of the molecules in the target and can be written as:

$$\alpha^l_{\alpha\beta} = \alpha\delta_{\alpha\beta} + \beta^l_{\alpha\beta} + (\Delta\alpha)^l_{\alpha\beta} \tag{1.14}$$

where α is called the isotropic part of the polarizability tensor since it is independent of molecular orientation, $\beta^l_{\alpha\beta}$ is the anisotropic part, traceless (zero trace) which changes as the molecule rotates, $(\Delta\alpha)^l_{\alpha\beta}$ comes from the local electromagnetic fields produced by the dipoles of the other molecules of the system and induced by the field of the probe. The scattering cross section coming from the first term of the 1.14 is the isotropic part:

$$\frac{\partial^2\sigma}{\partial\Omega\partial\omega} = \frac{\omega_0\omega_1^3}{2N\pi c^4}\alpha^2(\epsilon_0\cdot\epsilon_1)^2\int < \rho(\mathbf{Q},t),\rho^*(\mathbf{Q},0) > e^{-i\omega t}dt \tag{1.15}$$

It is proportional to the dynamic structure factor through

$$\boxed{\frac{\partial^2\sigma}{\partial\Omega\partial\omega} = \frac{\omega_0\omega_1^3}{2N\pi c^4}\alpha^2(\epsilon_0\cdot\epsilon_1)^2 S(Q,\omega)} \tag{1.16}$$

1.3 X-rays and neutrons: a comparison

Both inelastic x-ray and neutron scattering can provide important information on the study of the high frequency collective dynamics in condensed matter and, in both cases, one can measure directly the $S(Q,\omega)$ associated to atomic density fluctuations. In this section we discuss the main differences and analogies between the two techniques.

1.3.1 Inelastic X-rays (IXS) and neutrons (INS) cross sections

The neutrons interact directly with the nuclei, and not with the electrons around them and, similarly to the x-ray case, the interaction Hamiltonian has different terms that describe the coupling between the neutron and the nuclear and electronic operators. In the non relativistic limit, the principal interaction is with the nuclear density and it can be expressed with the Fermi pseudopotential:

$$H_i = \frac{2\pi\hbar^2}{m_N}\sum_j b_j \delta(R_j - r) \tag{1.17}$$

where m_N is the neutron mass, b_j is the scattering length, characteristic of the interaction between the neutron and the j^{th} nucleus at R_j, and the sum runs over all nuclei of the scattering system. Considering this interaction Hamiltonian, and following the same procedure as in the case of x-rays, it is possible to obtain the following expression for the scattering cross section:

- neutrons

$$\frac{\partial^2\sigma}{\partial\Omega\partial\omega_1} = \left(\frac{k_1}{k_0}\right)\sum_{F_N I_N} p_{I_N}\left|<\phi_{F_N}|\sum_l b_l e^{-iQ\cdot R_l}|\phi_{I_N}>\right|^2 \delta(E_F - E_i - \hbar\omega) \tag{1.18}$$

- x-rays

$$\frac{\partial^2\sigma}{\partial\Omega\partial\omega_1} = r_e^2\left(\frac{\omega_1}{\omega_0}\right)\sum_{F_N I_N} p_{I_N}\left|<\phi_{F_N}|\sum_l f_l(Q) e^{-iQ\cdot R_l}|\phi_{I_N}>\right|^2 \delta(E_F - E_i - \hbar\omega) \tag{1.19}$$

The neutron scattering length b_l of the 1.18 formally plays the same role of the atomic form factor $f_l(Q)$ in 1.19 but it is not Q-dependent in the Q-range of interest to atomic density fluctuations. This is because the dimensions of the nuclei are much smaller than the

inverse values of the momentum transfer Q typically considered in the study of the atomic dynamics, and therefore the scattering length is not expected to show any Q-dependence up to Q values of the order of the inverse of the nuclear size. As a consequence, the double differential scattering cross section in a neutron scattering processes does not decay for high Q values as it does for x-rays. In general, it is possible to have different scattering length b_l not only for each atom type but also for each isotope. Furthermore, for nuclei with a magnetic moment, the scattering length depends on the relative orientation between the spin of the incoming neutron and that of the considered nucleus. This characteristic makes very difficult the factorization of the scattering lengths. With the assumption of a random distribution of the nuclear spin orientation [2], however, in analogy with the x-ray case, the neutron double differential scattering cross section can be expressed as:

$$\frac{\partial^2\sigma}{\partial\Omega\partial E_1} = \left(\frac{k_1}{k_0}\right)[\sigma_c S(Q,\omega) + \sigma_i S_S(Q,\omega)] \qquad \textbf{neutrons} \qquad (1.20)$$

$$\frac{\partial^2\sigma}{\partial\Omega\partial E_1} = r_e^2\left(\frac{\omega_1}{\omega_0}\right)(\epsilon_0\cdot\epsilon_1)^2[\sigma_c S(Q,\omega) + \sigma_i S_S(Q,\omega)] \qquad \textbf{x-rays} \qquad (1.21)$$

where

$$\begin{cases} \sigma_c = < b >^2 \\ \sigma_i = < b^2 > - < b >^2 \end{cases} \qquad \textbf{neutrons} \qquad (1.22)$$

$$\begin{cases} \sigma_c = < f(Q) >^2 \\ \sigma_i = < f(Q)^2 > - < f(Q) >^2 \end{cases} \qquad \textbf{x-rays} \qquad (1.23)$$

The Eq. 1.20, 1.21 show the formal similarity between neutrons and x-rays scattering cross sections.

It is important to underline that for neutrons the incoherent term in the total cross section depends on the specific investigated system, and it is present even for mono isotopic samples, whereas in the case of x-rays it is completely absent for monoatomic, molecular and crystalline systems. In Fig. 1.2, it is shown the different behaviour of the coherent cross section versus the atomic number Z for x-rays and neutrons. In the case of x-rays, the $Q = 0$ limit is considered where $\sigma_c = r_0^2 Z^2$. This shows that the coupling of the

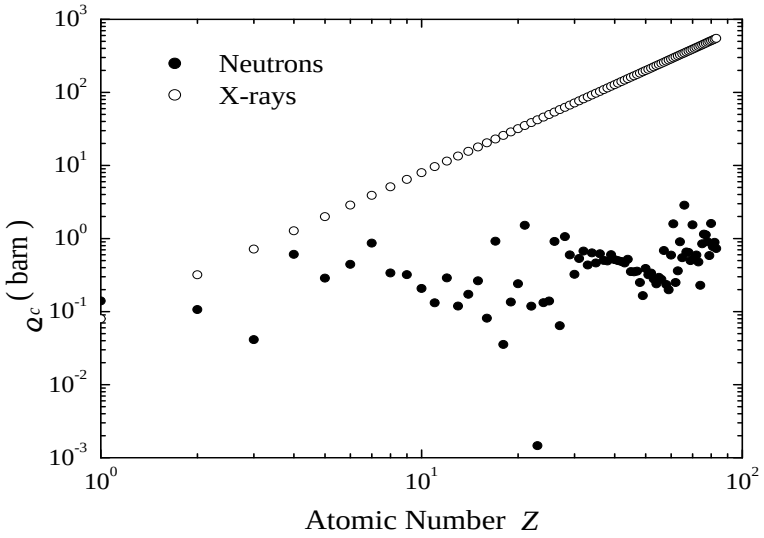

Figure 1.2. Coherent scattering cross section for neutrons and x-rays versus the atomic number. The coherent cross section for x-rays, i.e. $\sigma_c = r_0^2 Z^2$ is calculated assuming f(Q) = Z.

two probes is very similar in the low Z-region, and increases for x-rays as Z^2 at high Z values. The advantage, shown in Fig. 1.2, on studying systems with high Z for x-ray can be misleading in practice. In fact, the optimal scattering volume in the x-ray case, especially in high Z materials, is strongly limited by the photoelectric absorption process. To better appreciate this point, one must consider that the signal effectively measured in a scattering process must take into account the scattering volume and N. The scattered photon flux is given by

$$N = N_0 \frac{\partial^2 \sigma}{\partial \Omega \partial \omega} \Delta\Omega \Delta\omega \rho L e^{-\mu L} \tag{1.24}$$

where N_0 is the incident photon flux, $\Delta\Omega$ the solid angle and in the energy interval $\Delta\omega$, ρ is the density of the sample, L is the sample length, and μ is the linear attenuation coefficient. Eq. 1.24 is valid both for x-rays and neutrons and at the largest value for N is obtained when the sample length $L = 1/\mu$, i.e. the linear attenuation coefficient determines the effective scattering volume. For x-rays energies on the order of $10 \div 30$ keV and atoms with $Z > 3$, μ is basically determined by the photoelectric absorption process. In fact, while the atomic form factor increases as Z^2, the photoelectric linear attenuation coefficient increases roughly as Z^4. As a consequence, the effective scattering volume is

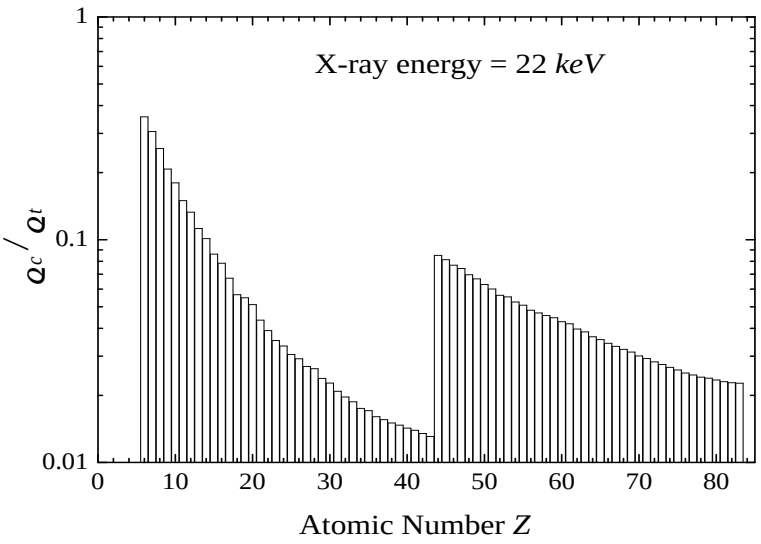

Figure 1.3. Ratio between coherent scattering and the total scattering cross section st for x-rays of incident energy 22 keV versus the atomic number.

rapidly reduced in materials with high Z atoms, making very difficult their study with x-rays. The ratio between the coherent (σ_c) and the total (σ_t) scattering cross section as a function of Z is reported in Figure 1.3 for an incident photon energy of 22 keV. Here $\sigma_c = e^2Z^2/(m_0c^2)$ and $\sigma_t = \mu/\rho$.

As we have seen, in the x-rays case, the photoelectric absorption determines the scattering volume, and this has the consequence that the multiple scattering processes associated to the Thomson scattering term are strongly suppressed and always almost negligible. This is not true for neutrons where the principal source of attenuation is the scattering process itself, and multiple scattering gives a large contribution to the scattered signal whenever the sample length is of the order of $1/\mu$.

1.3.2 Kinematics in the (Q, ω) plane for X-rays and neutrons

An important difference between neutrons and x-rays is connected to the kinematics of the scattering process that determines the different accessible regions of the plane (Q, ω) to the two techniques. In the **neutrons** case, the energy and momentum conservation laws impose the following relations:

$$\begin{cases} \mathbf{Q} = \mathbf{k}_0 - \mathbf{k}_1 \\ E = E_0 - E_1 \\ Q^2 = k_0^2 + k_1^2 - 2k_0k_1cos\theta \end{cases} \tag{1.25}$$

where θ is the scattering angle. For a neutron, the relation which connects energy and momentum is:

$$E(k) = \hbar^2k^2/(2m_N) \tag{1.26}$$

where m_N is the neutron mass. Using the equations 1.25, one obtains:

$$\left(\frac{Q}{k_0}\right)^2 = 2 - \frac{E}{E_0} - 2cos\theta\sqrt{1 - \frac{E}{E_0}} \tag{1.27}$$

As can be observed in Fig. 1.4, for a fixed incident neutron energy there are kinematics regions in the plane (Q, ω) not accessible by any scattering angle q. In these regions, the energy transfer is comparable or larger than the energy of the incident neutron and, here, one would have acoustic excitations propagating with a speed of sound larger than the velocity of the incident neutron. The thermal neutrons have an average energy of $\approx 25meV$ and corresponding total momentum of $\approx 35nm^{-1}$: This correspond to a speed of $\approx 2200m/s$. This condition, together with the energy and momentum resolution of the neutron spectrometers, make very difficult, even using faster neutrons, to cover efficiently the kinematics region associated to acoustic excitations with sound velocities larger than $\approx 1500m/s$. In crystalline systems, this limitation is overcame by the periodicity of the lattice, which allows to use the neutrons to study these dynamical properties in high order Brillouin zones. In disordered materials, where there is no translation invariance, i.e. no Brillouin zones, the propagation of collective excitations can be studied only at momentum transfer smaller than the inverse of the interatomic distances, i.e. in the analogous of the first zone where, indeed, the kinematic limits are the most severe. This explains the very few neutron studies in these systems. In the case of **x-rays**, the relation between energy and momentum is:

$$E(k) = \hbar ck \tag{1.28}$$

and the analogous of 1.27 is given by:

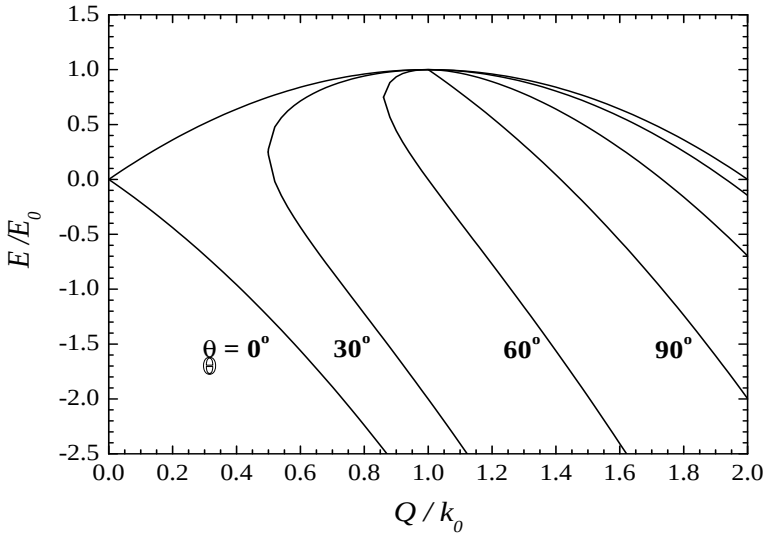

Figure 1.4. Kinematics regions accessible by neutron scattering experiments as function of the scattering angle q, for energy gain ($E < 0$) and energy loss ($E > 0$) of the scattered neutron.

$$\left(\frac{Q}{k_0}\right)^2 = 1 + (1 - \frac{E}{E_0})^2 - 2cos\theta(1 - \frac{E}{E_0}) \tag{1.29}$$

In the typical limit of small energies transfers, i.e. when $E \ll E0$, this expression reduces to

$$\frac{Q}{k_0} = 2sin\frac{\theta}{2} \tag{1.30}$$

We observe that the momentum transfer is completely determined by the scattering angle, and this show that there are basically no limitations in energy transfer for any accessible momentum transfer in the energy region typically spanned by phonon like excitations. The different accessibility to zones of the plane (Q, ω) determines the most interesting complementarity between the two techniques: unlimited energy transfer at small momentum transfer for x-rays, very large momentum transfer capabilities at very small energy transfer for neutrons.

1.3.3 Summary on the peculiarity of the IXS method

The x-rays couple to the electrons with a cross-section of the order of the square of the classical electron radius, and therefore with a strength comparable to that of the neutrons with nuclei. Within the adiabatic approximation, as far as the electronic state of the system is not modified by the scattering process, the ion dynamic structure factor, and therefore the collective ion excitations, becomes detectable by inelastic x-ray scattering through the electron density variations associated to the atomic density fluctuations. As a consequence, inelastic x-ray scattering, in principle, is a powerful spectroscopic technique for the study of the high frequency atomic dynamics of condensed matter and it is complementary to the inelastic neutron scattering technique in those specific cases where the neutrons are difficult to apply. The principal differences of the x-rays respect to the neutrons are:

- The IXS technique allows unlimited energy transfers in the accessible Q transfer range, namely in the $\approx 0.5 \div 150 nm^{-1}$ region. At larger Q-transfers, the signal is strongly reduced by the decay of the atomic form factor. This situation makes the IXS technique particularly suited in the study of collective excitations in liquids and disordered materials. In these systems, in fact, the lack of translation invariance requires that the collective excitations must be studied in a momentum transfer region comparable or smaller than that corresponding to Q_m, the inverse of the intermolecular distances. This is the Q region of major interest, i.e. the one below the first maximum of the static structure factor S(Q). This region is very difficult to reach in most materials with neutrons and this explains why, so far, the studies on the high frequency dynamics of disordered systems have been very few.

- The inelastic x-ray scattering cross-section is almost completely coherent and isotope independent, contrary to the neutron case, where often the incoherent contribution may dominate, or it is difficult to be separated from the coherent one.

- With x-rays, it is possible to have a very good Q-resolution and a very small spot size on the sample. This may offer the possibility to study materials available only in small quantities, and samples under extreme thermodynamics conditions (which is the case of this thesis).

- Finally, the absence of multiple scattering processes allows the direct measurement

of the dynamic structure factor without need of sophisticated procedures for the data reduction and analysis.

The development of the inelastic x-rays scattering technique to study collective excitations has been, so far, very difficult for the following reasons:

- An x-ray with a wavelength $\lambda = 0.1nm$ has an energy $E_0 \approx 12keV$, and therefore the study of excitations in condensed matter with energies of the order of few meV requires a very good relative energy resolution, i.e. $\Delta E/E \approx 10^{-7} \div 10^{-8}$. This poses severe constraints on the monochromator and analyzer optics, as well as on the divergence and flux of the incident and scattered photons beams.

- The fast decay of the form factors with increasing Q is responsible for important signal losses already at relatively small Q, and, therefore this limits the efficient use of the IXS technique to Q-values well below $150nm^{-1}$.

- At the considered x-ray energies, the photoelectric cross section is in general larger than the Thomson one. Considering that the increase of the photoelectric cross section with the atomic number Z goes roughly as Z^4 , the applications of the inelastic x-ray scattering technique are most effective in the study of low Z materials.

Chapitre 2

Ce chapitre est consacré à la description du spectromètre de diffusion inélastique de rayons X à très haut pouvoir de résolution, installé à l'ESRF de Grenoble dans la ligne de lumière ID16. Nous montrerons les principes généraux qui ont inspiré la construction de cette ligne de lumière. Ses éléments principaux et ses caractéristiques seront aussi illustrés dans le détail. Il est basé sur le principe du spectromètre à trois axes et perme de réaliser des expériences de diffusion inélastique des rayons X avec une résolution en énergie de 1.5 meV en utilisant une énergie incidente de 21747 eV. Dans ce chapitre on discutera la méthode utilisée pour obtenir des rayons X très monochromatiques. Elle est basée sur la diffraction de Bragg et demande

- *l'utilisation des réflexions de Bragg d'ordre élevé de cristaux parfaits,*
- *l'utilisation de la géométrie en 'backscattering' pour ces réflexions.*

Le chapitre est organisé comme suit:
dans le Par 2.2 nous illustrons le principe de fonctionnement du spectromètre et les concepts fondamentaux sur lesquels se base la ligne de lumière.
Le Par 2.3 est dédié à la description des caractéristiques des éléments principaux de ID16 et à ses performances principales.

Chapter 2

The inelastic X-rays scattering method

2.1 Introduction

Thanks to the development of the third generation synchrotron radiation source with very high brilliance, collimation and polarization, it has been possible to construct very high resolution IXS spectrometers. A big contribution in this direction has been made by the European Synchrotron Radiation Facility (ESRF) in Grenoble with a meV energy resolution IXS spectrometer. It has been working by now for eight years. It is based on the principle of the triple axis spectrometer and allows to perform experiments with an energy resolution up to 1.5 meV with incident photons of 21748 eV energy. An energy resolution of the order of meV is achieved by the IXS method for very small values of the ratio $\Delta E/E$. This requires very high photons fluxes. In this chapter we will discuss the method used to obtain highly monochromatic X-rays exploited at the beam-line ID16 at the ESRF. It is based on the Bragg diffraction and requires i) the use of high orders Bragg reflections from perfect crystals; ii) the use of nearly backscattering geometry for these reflections. It is possible to perform energy scans either by changing the monochromator or analysers crystal Bragg angles or by varying the relative lattice parameter of the two crystals through the change of their relative temperature. In order to avoid to drastically affect the resolution with geometrical contributions due to the change of the Bragg angle, at ID16 the problem has been overcome by exploiting the second strategy and in particular by keeping fix the temperature of the analyser crystal and by varying the one of the monochromator. Aiming to obtain resolving power of the order of $(\Delta E/E) \approx 10^{-7} \div 10^{-8}$, the temperature stability of the two crystals has to be maintained within the mK range,

while the typical temperature step in a scan has to be of the order of $5 \div 10\ mK$. This chapter is structured as follow:
Sec. 2.2 is dedicated to illustrate the working principle of the spectrometer and the fundamental concepts behind the beamline construction, as the intrinsic resolving power for silicon crystals and the backscattering geometry.
Sec. 2.3 is devoted to the description the characteristics of the main optical elements of ID16. In the last part, the general performances of this beamline will be discussed. In particular the energy and momentum resolution will be reviewed.

2.2 Basic ideas

This section is devoted to present the basic ideas to develop a spectrometer for inelastic X-rays scattering with meV energy resolution. It is based on the working principle of a triple axis spectrometer which exploits high order Bragg reflection from perfect crystals and the backscattering geometry. We describe it in the following.

2.2.1 The triple axis spectrometer

The general principle of a triple axis spectrometer is schematized in Figure 2.1
The first axis corresponds to the backscattering crystal monochromator, here the energy E_i of the incident beam is selected by an elastic Bragg scattering process. The second axis, corresponds to the sample which scatters inelastically at an angle θ. This angle determines the geometry (Figure 1.1) and the moment transfer Q. The scattered energy E_f is finally analyzed by the backscattering crystal analyser through an elastic Bragg scattering process, as in the case of the first axis. This analayzer defines the third axis. According to the Bragg's law, the energy difference between incident and analyzed beam can be achieved either by varying the Bragg angles θ_B either by varying the lattice parameter d_h of one of the two crystals by changing its temperature. As we will see, the latter method is well suited for high resolution inelastic x-rays scattering to perform energy scan at fixed momentum transfer; this allows in fact to keep always constant the geometrical contributions of the total resolving power of the instrument. To obtain high energy resolution, two conditions are necessary:

- use of high order reflections from perfect crystals

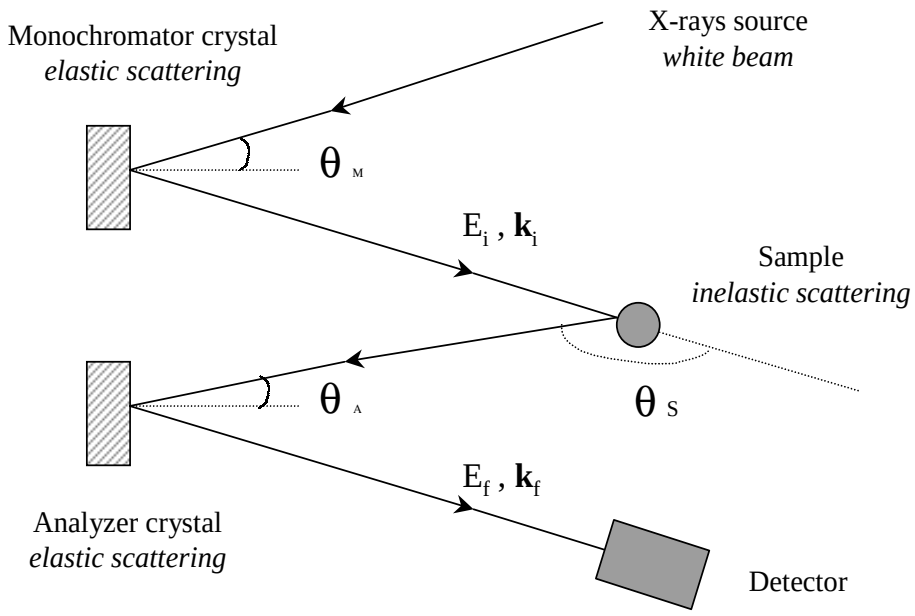

Figure 2.1. General principle of a triple axis spectrometer.

- use of backscattering geometry

We derive the energy resolution starting from the Bragg's law:

$$2d_h sen\theta_B = h\lambda \tag{2.1}$$

where d_h is the spacing of the crystal lattice planes of the reflection with Miller index h; θ_B is the Bragg angle between the incident x-ray and the diffraction planes; λ is the wavelength of the diffracted x-ray; exploiting the following relations:

$$\begin{cases} \lambda = \frac{2\pi}{k} \\ \tau_h = \frac{2\pi}{d_h} \\ sin\theta_B = cos(\frac{\pi}{2} - \theta_B) \\ \epsilon = \frac{\pi}{2} - \theta_B \end{cases}$$

equation 2.1 can be rewritten as:

$$2kcos\epsilon = \tau_h \tag{2.2}$$

where $\tau_h = 2\pi/d_h$ is the reciprocal lattice vector; $k = 2\pi/\lambda$ is the photon wave-vector and the angle ϵ expresses the deviation from perfect backscattering $\theta_B = \pi/2$. The wave-vector

given by Eq. 2.2 depends from the two parameters ϵ and τ_h

$$k = k(\epsilon, \tau_h)$$

variations in ϵ and τ_h produce variations in k, this allows to write $\delta k/k$ as the sum of two contributions:

$$\frac{\delta k}{k} = \sqrt{\left(\frac{\delta k}{k}\right)_h^2 + \left(\frac{\delta k}{k}\right)_\epsilon^2} \tag{2.3}$$

The energy resolution can be achieved by exploiting the relation between the energy and the wave-vector of an x-ray beam $E = \hbar ck$, which leads to:

$$\frac{\delta E}{E} = \frac{\delta k}{k}$$

Exploiting this expression, the energy resolution can be written as:

$$\frac{\delta E}{E} = \sqrt{\left(\frac{\delta E}{E}\right)_h^2 + \left(\frac{\delta E}{E}\right)_\epsilon^2} \tag{2.4}$$

In the next two subsections we describe in detail the origin of these two terms.

2.2.2 High order reflections from perfect crystals

The term $(\frac{\delta E}{E})_h$ represents the contribution due to the intrinsic properties of the crystal. The best relative energy resolution $(\frac{\delta E}{E})_h$ at a given diffraction order h, can be derived in the framework of the Dynamical Theory of x-ray diffraction [10]. An efficient experimental method to obtain a very high resolving power for X-rays is based on Bragg diffraction from perfect crystal. A Bragg reflection is characterized by an angular width, customarily called *Darwin width* ω_D. In the conventional dynamical theory [10] ω_D can be written as:

$$\omega_D = \frac{4r_0 d_h^2}{\pi V \sqrt{b}} C |F_h| e^{-W} tg\theta_B \tag{2.5}$$

where r_0 is the classical electron radius, V the unit-cell volume, C the polarization factor, b the asymmetry factor[1], F_h the crystal structure factor and e^{-W} the temperature factor,

[1]The asymmetry factor is defined as: $b = sin(\theta_B - \alpha)/sin(\theta_B + \alpha)$, where α is the asymmetry angle between the crystal surface and the family of the h diffracting planes. It is worthwhile to observe that,in backscattering geometry, the intrinsic energy resolution of a perfect crystal cannot be changed by varying the asymmetry angle α, because $b \to 1$ when $\theta_B \to pi/2$

generally referred to as the Debye-Waller factor. By using the conventional dynamical theory [10] it is also possible to calculate the *extinction length* t_{ext} defined as the distance of penetration of the beam into a perfect crystal in the direction perpendicular to the diffraction planes after which the intensity of the incident beam has decreased by 1/e:

$$t_{ext} = \frac{V}{2d_h r_0 C|F_h|} \tag{2.6}$$

At a given diffraction order h, the best relative energy resolution is an intrinsic property of the crystal. This quantity is inversely proportional to the number of lattice planes effectively involved in the reflection process. From the dynamical theory of x-ray diffraction [10] this quantity is derived as

$$\left(\frac{\delta E}{E}\right)_h = \frac{4r_0 d_h^2}{\pi V\sqrt{b}} C|F_h|e^{-W} \tag{2.7}$$

It can be related either to the Darwin width or to the extinction length through the relations:

$$\left(\frac{\delta E}{E}\right)_h = \omega_D cotg\theta_B \tag{2.8}$$

$$\left(\frac{\delta E}{E}\right)_h = \frac{1}{\sqrt{b}\pi}\frac{2d_h}{t_{ext}} \tag{2.9}$$

The intrinsic energy resolution of a Bragg reflection varies with the square of the d-spacing d_h and is proportional to the structure factor F_h. Most important, it is independent of the Bragg angle θ_B. This is a very important point, which underlines the fact that the resolving power is determined by the number of planes participating in the diffraction process. This number of planes is determined by the transmission and reflection probabilities of a single plane, a quantity that again, cannot depend on the scattering geometry but only on the intrinsic properties of the reflection, i.e. the unit cell form factor F_h (calculated at the Q-value corresponding to the considered reflection $Q_h = 2\pi/d_h$), and the d-spacing d_h. This accounts for the decrease of $(\Delta E/E)_h$ with increasing the order of the reflection. In fact, both F_h and d_h decrease as the order is increased. The structure factor F_h is strictly connected to the atomic form factor $f(Q)$ through the relation $F_h = \sum_{i=1}^{N} f_i(Q)e^{iQ_h \cdot r_i}$ The behaviour of the atomic form factor of silicon crystals, as a function of Q_h, is shown in Figure 2.2 it decreases with Q, or equivalently with increasing the reflection order. As a consequence increasing the reflection order one decreases the number of reflected

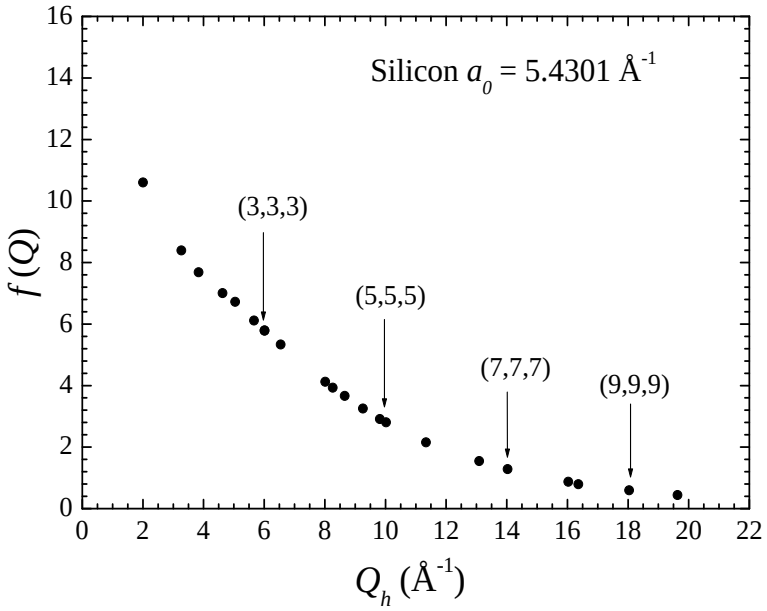

Figure 2.2. Atomic form factor of Silicon derived from the experimental determination, at room temperature, of the structure factor [11, 12]

photons by each plane. This allows the photons a deeper penetration inside the crystal. This picture is true as soon as the crystal is perfect and the penetration length due to the photoelectric absorption t_{abs} is larger then the extinction length t_{ext}.

In Figure 2.3 the evolution of the absorption length t_{abs} and the one of the extinction length for a silicon crystal are shown as a function of $Q_h = 2\pi/d_h$. It can be noted that, for low order Bragg reflections, the extinction length is always much shorter than the absorption length. In a perfect silicon crystal, indeed, for Bragg reflection of low order one is always in conditions where the Bragg reflection is described successfully by the dynamical theory of a perfect non absorbing crystal. The situation is not as satisfactory approaching $Q_h = 30\ \mathring{A}^{-1}$, here in fact the two lengths become equal. At even larger Q_h values, the ideal resolving power cannot be any longer achieved because the needed theoretical penetration depth into the crystal is limited by the photo-absorption length. The ideal penetration depth can also be reduced by crystal defects or imperfections which limit the maximum size of the grain that one considers to be the perfect crystal. In our specific context, therefore, the definition of perfect crystal is related to the considered reflection order, and the required crystal perfection implies that the relative variation of

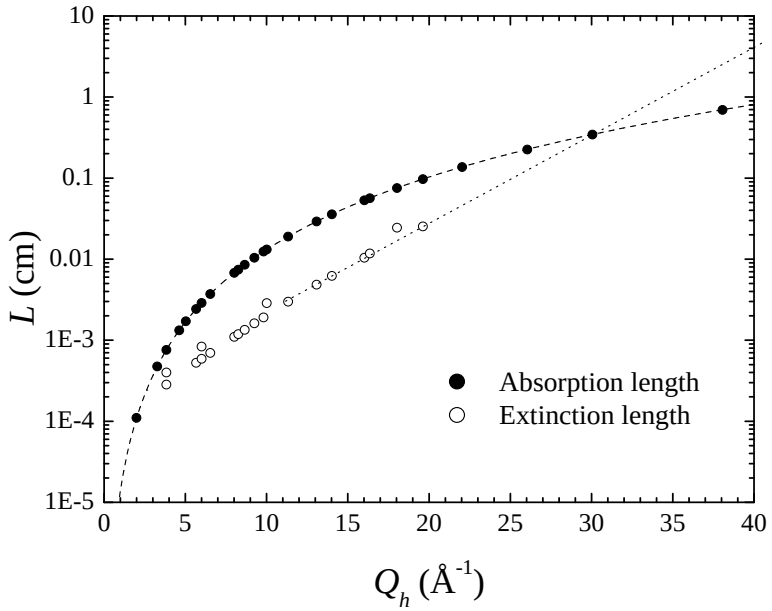

Figure 2.3. Absorption length t_{abs} (full circles) and extinction length t_{ext} (open circles) for a perfect silicon crystal as a function of Q_h.

the lattice constant in the diffraction volume, $\Delta d/d$, is smaller than the intrinsic relative energy resolution of the considered reflection. In our case we aim to $\Delta E/E \approx 10^{-8}$. At high reflection orders, actually, this "perfection" definition is obtained only with silicon.

2.2.3 Backscattering geometry

The term $(\delta E/E)_\epsilon$ of equation 2.11 represents the geometrical contribution to the energy resolution, it is due to the angular divergence of the beam. To minimize this contribution, the backscattering geometry is introduced. The backscattering geometry is necessary to our purposes essentially for two interconnected reasons:

i) it allows to use efficiently the photon flux at the high order reflections

ii) it allows to minimize the geometrical contributions to the total resolving power

In order to demonstrate these two statements, we will remind few basic concepts of the dynamical theory of the x-rays diffraction. A given reflection order has a characteristic angular acceptance, called Darwin width ω_D. This quantity is a direct consequence of the finite energy resolution of the considered reflection, and corresponds to the angular range

in which a photon of wavelength λ is efficiently Bragg-reflected by the crystal (reflectivity R = 1 in absence of photoelectric absorption). For symmetric crystals the relation between ω_D and the intrinsic resolving power is given by Eq. 2.5. The geometrical contribution to the total resolving power, considering an incident white beam with divergence $\delta\epsilon$, is obtained from the differentiation of the Bragg's law 2.1.

$$\left(\frac{\Delta E}{E}\right)_{\epsilon} = \Delta\epsilon cotg\theta_B \tag{2.10}$$

This geometrical contribution and the intrinsic contribution give a total energy resolution:

$$\left(\frac{\Delta E}{E}\right) = \sqrt{\left(\frac{\Delta E}{E}\right)_h^2 + \left(\frac{\Delta E}{E}\right)_{\epsilon}^2} = \sqrt{\omega_D^2 + \Delta\epsilon^2} cotg\theta_B \tag{2.11}$$

It is clear from Eq. 2.11 that, in order to have a total resolving power $(\Delta E/E) \approx (\Delta E/E)_h$ the Darwin width (intrinsic width of a Bragg reflection) has to be much larger than the angular divergence of the incident beam. However, in general, the Darwin width of an high order reflection is very small. For reflections with an intrinsic resolving power $\Delta E/E \approx 10^{-8}$ and for angle such that $tan\theta_B \approx 1$, the angular acceptance ω_D is of the order of few tenths of nrad, a value much smaller than the typical collimation values of x-ray beams. In this situation the number of reflected photons from a perfect crystal in the desired energy bandwidth is drastically reduced. The quantity ω_D is dependent of the scattering geometry via the term $tan\theta_B$ and we note that it increases by increasing the Bragg angle. In particular we note that it becomes very large close to 90^0. The extreme backscattering geometry has been proposed since 1965, where this solution was though to provide a good method for very high precision diffraction work [13, 14]. With respect to its use for inelastic x-rays scattering, one notes that using 2.5 as an indication of the actual value of ω_D , with an angle $\theta_B \approx 89.95^0$ one has $tan\theta \approx 1000$. Consequently, for reflections with an intrinsic resolving power $\Delta E/E \approx 10^{-8}$ we have $\omega_D = 10^{-5} rad$, and therefore one can work with an incident beam of 10 μrad divergence. This divergence is comparable to that obtained recently from an undulator on a third generation light source, and therefore, using this backscattering geometry one uses all the available photons in the considered energy bandwidth, without a sensible deterioration of the intrinsic energy resolution of the reflection. In Table **??** we report, as an example, the Darwin widths calculated using the relation 2.5 for the most used Si(h,h,h) reflections on the beamline ID16 (ESRF) with an operative Bragg angle $\theta_B = 89.98^0$. This Bragg angle corresponds to a deviation ϵ

Reflection	$\Delta E/E$	ω_D $[\mu rad]$
(5,5,5)	$1.5.10^{-6}$	4297
(7,7,7)	$3.6.10^{-7}$	1031
(8,8,8)	$2.4.10^{-7}$	688
(9,9,9)	$1.0.10^{-7}$	286
(11,11,11)	$3.6.10^{-8}$	103
(12,12,12)	$2.8.10^{-8}$	80
(13,13,13)	$2.0.10^{-8}$	57

Table 2.1. Darwin widths of the most used Si(h,h,h) reflections at the beamline ID16 (ESRF) calculated with the relation 2.5 for an operating Bragg angle $\theta_B = 89.98^0$ and exploiting $\Delta E/E$ values from reference [15]

from perfect backscattering of 350 μrad, while the vertical angular divergence from an undulator at the ESRF is in average $\delta\epsilon \approx 13$ μrad Full Width Half Maximum (FWHM), i.e. we are in the condition that ϵ is still much larger than $\delta\epsilon$. It is easy to observe that the calculated angular acceptance ω_D is always much larger than the angular divergence of the X-ray beam, and, as a consequence, the geometrical contributions to the relative energy resolution are always very small. However, as already pointed out, Eq. 2.5 looses its validity when $\theta_B \to \pi/2$ and, therefore, the ω_D values of Table 2.1 are only an indication of the exact values that, nevertheless helps us to have an idea of the order of magnitude of ω_D.

In the Bragg angle region near $\theta_B = \pi/2$ the dynamical theory of x-rays diffraction needs some corrections and such reformulation is analyzed in ref. [16, 17, 18]. They show that, as long as $\omega_D \approx \epsilon$, ω_D is even larger than the prediction based on 2.5. Working with nearly backscattered reflections the contribution to the relative energy resolution, due to the finite divergence of the beam, can be evaluated from 2.2 using the Taylor expansion in the variable ϵ

$$\left(\frac{\Delta E}{E}\right)_\epsilon = \left(\frac{\Delta k}{k}\right)_\epsilon = tan\epsilon\delta\epsilon + (2tan^2\epsilon + 1)\frac{1}{2}\delta\epsilon^2 \tag{2.12}$$

where $\delta\epsilon$ corresponds to the angular divergence of the x-rays beam. For $\epsilon \ll 1$ and neglecting high order terms the 2.12 becomes:

$$\left(\frac{\Delta E}{E}\right)_{\epsilon} = \epsilon\delta\epsilon + \frac{1}{2}\delta\epsilon^2 \tag{2.13}$$

which shows that to minimize this additive contribution one has to reduce both the angular divergence and the deviation from backscattering. From 2.13 we can envisage two different situations: a value of ϵ smaller than $\delta\epsilon$ leads to a parabolic variation of the energy resolution, while larger angular deviation, while larger angular deviations lead to a linear change. This is true as long as the incident beam divergence is small compared to the angular acceptance of the crystal. In the case of ID16 at ESRF the condition $\epsilon \geq \delta\epsilon$ is always satisfied and the geometrical contribution to the relative energy resolution can be evaluated as $(\delta E/E)_{\epsilon} \approx 7 \cdot 10^{-9}$ with deviation from backscattering $\epsilon = 350\ \mu rad$ and divergence $\delta\epsilon = 10\ \mu rad$. This value $(\delta E/E)_{\epsilon}$ is always smaller than the energy resolutions $(\delta E/E)_h$ for a silicon crystal. In conclusion, the extreme backscattering geometry is important in order to exploit efficiently the incident photon flux, and to minimize the geometrical contribution to the total resolving power coming from the scattering process.

2.3 Characteristics of the beamline ID16 at the ESRF

This section is devoted to illustrate the characteristics of the beamline. In particular we will review the working principle, the layout, and the general performances of this very high energy resolution spectrometer. As described in previous section an energy scan is possible either by varying the Bragg angles either by varying the lattice parameter d_h of one of the two crystals by changing its temperature. In the case of backscattering geometry it is not possible to change the relative energy between monochromator and analyser by changing the Bragg angles because, the energy variation is small and the loss in energy resolution, due to the geometrical contributions, becomes very large for small angle variations ($\approx tan\theta_B$). In order to overcome this difficulty the energy scans can be performed by varying the other parameter entering in the Bragg law: this is the lattice parameter d_h. A variation of d_h is obtained by changing the temperature of the crystal. In fact, a change ΔT induces a relative variation in the lattice constant given by:

$$\frac{\Delta d}{d} = \alpha(T)\Delta T \tag{2.14}$$

where $\alpha(T)$ is the coefficient of thermal expansion ($\alpha = 2.56 \cdot 10^{-6} K^{-1}$ in silicon at 294

K [19]). According to the Bragg's law $\lambda = 2dsin\theta_B$ at fixed θ_B:

$$\frac{\Delta\lambda}{\lambda} = \frac{\Delta E}{E} = -\frac{\Delta d}{d} = -\alpha(T)\Delta T \tag{2.15}$$

This shows that a scan $\Delta d/d$ is analogous to a scan $\Delta E/E$. Therefore, the energy scans between monochromator and analyser are obtained by changing the temperature of one of the two crystals, in our case the monochromator, keeping the other crystal (the analyser) at constant temperature. Under these experimental conditions the geometrical contributions to the energy resolution are constant because the scattering geometry of the first and third axis is the same for any energy transfers. To obtain a sufficiently small energy step size for reflections with a resolving power $\Delta E/E \approx 10^{-7} \div 10^{-8}$, the temperature of the monochromator and analyser crystals has to be controlled with mK precision, considering that $\alpha \approx 10^{-6}$. A schematic side view of the main optical elements of the beamline and of the horizontal spectrometer is shown in Figure 2.4.
Starting form the source and following the x-rays path down to the detector, the main characteristics of each element will be discussed in some detail. The vertical scale is expanded with respect to the horizontal one to better show the different components.

Undulator source: The x-rays source is composed of three linear undulators with a magnetic period of 35 mm and length 1.6 m, which are located on a high-β straight-section of the storage ring. An undulator is a periodic array of magnets disposed in a way to impose many oscillations to the motion of the electrons beam [20]. Crossing this magnetic structure, the electron beam emits radiation at each individual wiggle. which interferes coherently with the ones emitted by the others producing sharp peaks in the energy spectrum, called harmonics. The photon energy of these harmonics can be changed by varying the distance between the upper and the lower magnets of the undulator. Such a distance, determining the magnetic gap, can vary from 16 to 35 mm. The undulators are normally used from the 3rd to the 7th harmonic in order to cover an the energy range from 7 to 30 keV. The angular divergence of the central cone of the X-ray beam coming from the undulators is roughly 15 vertical x 40 horizontal μrad^2 (FWHM), with a bandwidth $\delta E/E = 10^{-2}$ and an integrated power of roughly 200 W.

Double-Crystal Premonochromator: The white x-rays beam coming from the undula-

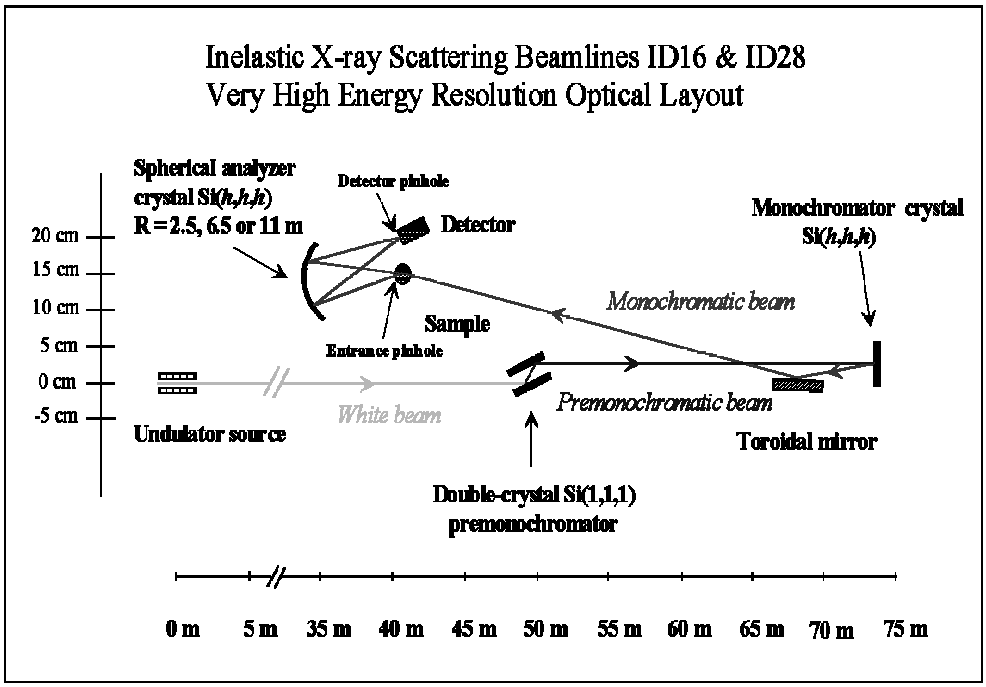

Figure 2.4. Schematic layout of the horizontal spectrometer of the inelastic x-rays scattering beamline at ESRF. The vertical displacements, determined by the double-crystal pre-monochromator, by the backscattering angle of the monochromator, by the toroidal mirror and by the analyser crystal, are not shown on the same scale as those along the beam path. In order to give an idea, at the sample position, the height difference between the white and monochromatic x-rays beam is roughly 15 cm.

tors is premonochromatized by a Si(1,1,1) double crystal monochromator to a bandwidth of $\delta E/E = 2 \cdot 10^{-2}$. The premonochromator is cryogenically cooled with a closed-loop circuit of nitrogen in order to absorb the unwanted power and to reduce thermal deformations. The premonochromator crystal works in nearly fixed-exit conditions in the Bragg-angles range of $4^0 \div 5^0$ and diffracts the beam vertically 22 mm above the white beam. In the used energy range $(7 - 28KeV)$ the angular acceptance of the Si(1,1,1) crystal is either larger or pretty well matched to the vertical divergence of the undulator source.

High Energy Resolution crystal Monochromator: The photons coming from the premonochromator impinge on the very high resolution monochromator constituted by a

flat Si(1,1,1) crystal symmetrically cut and temperature controlled with a precision in the mK range. The specific Si(h,h,h) reflection is chosen by simply tuning the premonochromator Bragg angle at the correct energy and adjusting the undulator gap accordingly. The Bragg angle of the Si(1,1,1) matching the energy of a Si(h,h,h) reflection with $\theta_B = 90^0$ is given by the relation:

$$2d_1 sin\theta_B = 2d_h = \frac{2d_1}{h} \rightarrow sin\theta_B = \frac{1}{h} \tag{2.16}$$

where h is the desired reflection order. The monochromator crystal has an operative Bragg angle of 89.98^0 in the vertical plane and the diffracted x-ray beam is monochromatized to a bandwidth $\Delta E/E \approx 10^{-6} \div 10^{-8}$. This extreme backscattering angle, as already explained in previous section, is chosen to insure that the divergence of the incoming beam is always much smaller than the Darwin width of the considered reflection, while the deviation from perfect backscattering is still large compared to the beam divergence. The design and the performances of this very high energy resolution monochromator are described in details in reference [15].

Toroidal mirror: The very high energy resolution x-ray beam is focused on the sample by a grazing incidence (3 mrad) toroidal mirror to a spot size of 150 vertical x 350 horizontal μm^2 (FWHM). The mirror has a platinum coating deposited on the optically polished surface obtained from a Zerodur glass substrate. The mirror has an entrance arm of 78 m and an exit arm of 24 m. This gives approximately 3:1 demagnification of the source in the image plane at the sample position. We want to underline that the traveled distance by the X-ray beam from the undulator source to the sample is 102 m.

High Energy Resolution Spherical Crystal analyser: The photons scattered by the sample are collected by a spherical silicon crystal analyser positioned at the tip of an arm able to rotate around the scattering sample in order to select the desired Q-value. This analyser crystal is operating at the same Si(h,h,h) as the monochromator crystal and at a Bragg angle very close to backscattering ($\theta_B = 89.98^0$). This spherical analyser crystal is also temperature controlled with a precision in the mK range, and is desired to have the same energy resolution as the monochromator crystal but whit a much larger angular acceptance. This angular acceptance is chosen by moving a set of apertures in

front of the analyser crystal, and it is typically determined by the desired Q-resolution. An angular acceptance up to $4x10\ mrad^2$ is an adequate compromise of Q-resolution ($\Delta Q \approx 0.5nm - 1$) and signal maximization. Such a large angular acceptance, larger than the deviation $\epsilon = 350\mu rad$ from perfect backscattering, can be only obtained by using a focusing optics and by keeping, at the same time, the characteristic of a perfect crystal analyser. This excludes the possibility to elastically bend a crystal because such a procedure introduces important deformations which degrade the energy resolution [15, 21]. A possible solution to the problem is to position small flat crystals, squares of side length c, on a focusing substrate of radius R, where $c \ll R$. Providing that this focusing substrate is a sphere in 1:1 Rowland geometry, the Bragg angle variation on these small crystals will be c/R. If the size c is chosen in a way that the ratio c/R is comparable or smaller than the Darwin width, the spherical analyser will reflect the X-rays with almost the intrinsic energy resolution of the considered reflection. Following this idea, within the Inelastic X-ray Scattering Group at the ESRF a new method has been developed that allows to glue 12000 independent silicon crystals on a spherical substrate with radius R. The spherical substrates are obtained from silicon disks with a diameter of 100 mm. The size c of these small crystals is $\sim$ 0.7 x 0.7 mm^2, and their thickness is 3 mm [22, 23]. At the moment at the beamline ID16 there are five analysers simultaneously working during an IXS experiment. They are fixed at the end of an arm able to rotate in the horizontal plane and are located one next to the other with an angular offset of 1.56^0. This allows to measure five IXS energy spectra at five different Q-values simultaneously. The arm, 6.5 m long, is able to cover an angular range between 0^0 and 13^0. Such a considerable length, offers to reduce the geometrical contribution to the energy resolution. The spherical analysers with a radius R = 6150 mm are equipped with analyser slits. The most used reflections at the beamline are the Si(h,h,h) with h = 5, 7, 8, 9, 11, 12, 13. More informations on their construction can be found in reference [21]

Detector: The detector is a silicon diode of equivalent thickness 2.5 mm and with a background signal of the order of 1 $count/min$. The detector is sitting on the same arm of the analyser crystal. On this arm are also mounted an entrance pinhole placed just after the sample and a detector pinhole placed before the detector (see Figure 2.4). Due to the extreme backscattering geometry the detector is basically on top of the entrance pinhole at a distance ranging between $3 \div 4$ mm.

Beamline performances

Momentum resolution: The momentum resolution is basically determined by the opening of the analyser's slits at the selected Si(h,h,h) reflection. As an example using the horizontal spectrometer and the Si(9,9,9) reflection the momentum resolution can vary between $0 \div 1.2\ nm^{-1}$, while using the Si(11,11,11) reflection the momentum resolution can vary between $0 \div 1.6\ nm^{-1}$. The maximum momentum transfer allowed by using the horizontal spectrometer is 26.5 nm^{-1} at the Si(9,9,9) reflection and 32 nm^{-1} at the Si(11,11,11) reflection. The minimum momentum transfer is roughly 0.5 nm^{-1}. This value is related to the minimum scattering angle that allows to avoid that the direct beam transmitted by the sample enters in the spectrometer vacuum chamber by the spectrometer entrance pin-hole.

Energy resolution: The energy resolution is measured by looking at the elastic scattering from a 5 mm thick polymethylmethacrylate (PMMA) sample at $Q = 10\ nm^{-1}$. At this Q value the spectrum of PMMA is dominated by the extremely narrow quasi-elastic component, namely the incident beam can be assumed as a delta function of the energy. The inelastic scattering contribution has been further reduced by keeping the PMMA at 10 K. At this temperature the inelastic signal is drastically reduced in the whole Q range, allowing to measure the energy resolution even at Q values lower than $Q = 10\ nm^{-1}$ and excluding the presence of any unwanted Q-dependence. The measured experimental resolutions are presented in Chapter 5. Using the horizontal harm analyser with $R = 6450\ mm$ we measure an energy resolution of $1.5 \pm 0.2\ meV$ at the Si(11,11,11) reflection and $3.0 \pm 0.2\ meV$ at the Si(9,9,9) reflection with an angular acceptance of 100 $mrad^2$. More information on the ID16 beamline construction and on its performances can be found in [24, 25, 15, 21].

Chapitre 3

L'objet de ce chapitre est de donner une vue d'ensemble des principales approches théoriques de l' étude de la dynamique collective des systè mes désordonnés dans les différentes régions du plan (Q,ω). Dans ce contexte, on peut distinguer trois situations limites différentes :

- *la région hydrodynamique macroscopique, où le systè me est considéré comme un milieu isotrope continu,*
- *la région mésoscopique, correspondant à la gamme de transfert d'impulsion de l'ordre de l'inverse des distances interatomiques,*
- *la région de particule isolée, où le mouvement de la particule est considéré comme libre entre deux collisions successives.*

Une attention particuliè re sera portée à la région mésoscopique où la diffusion inélastique de rayons X est particuliè rement convenable pour explorer la dynamique microscopique. Le but de ce chapitre est donc de rappeler les concepts et les équations de base que nous utiliserons pour analyser et interpréter les données expérimentales présentées dans la thè se. Il est organisé comme suit :
dans le Par 3.2 nous introduisons les instruments analytiques pour décrire la dynamique des fluctuations de densité ainsi que les principales approches théoriques pour étudier la dynamique dans différentes régions du plan :
dans le Par. 3.3 nous considérons l'hydrodynamique macroscopique où le spectre de fluctuation de densité est bien décrit à partir des équations hydrodynamiques de Navier-Stokes ;

dans le Par 3.4 nous considérons la région mésoscopique où le spectre de fluctuation de densité est décrit dans le cadre de l'Hydrodynamique Généralisée. Cette théorie est obtenue en exploitant l'approche de la Fonction Mémoire expliquée dans le Par. 3.5. Grâce à cette approche, on arrive à décrire de faon analytique les processus de relaxation dans un liquide et à dériver les principaux modè les utilisés pour analyser nos données.

Chapter 3

Collective dynamics of liquid systems

3.1 Introduction

An essential distinction among liquids, gases and crystals is drawn with respect to the nature of the microscopic motion of the atoms in the system. In a crystal the atoms are fixed in a well defined structure except for the vibrational motion around their equilibrium positions; in a gas the atoms are free to make long translational movements. A liquid constitutes an intermediate situation: the translational movements are an essential characteristic of the atomic motion and, at the same time, since the atoms are surrounded by nearby atoms, their motion is also partially oscillatory. The translational motion is, by the way, the principal feature of the liquid and is such that each atom moves through the material changing continually neighbours. A quantitative measure of the correlation between atoms in different points in space and time, is provided by the *density-density correlation function* which furnishes the probability to find a particle in a certain point R and time t given that there was another particle in the origin at t=0. Information on this function and on the microscopic dynamic behaviour of a liquid can be gained from inelastic scattering experiments. A scattering process is marked by the presence of waves scattered with frequencies and in directions different from the ones of the incident beam. Depending on the wavelength and frequency at which the structure is explored, the system shows peculiar dynamic behaviours:

- the *hydrodynamic regime* is investigated when $\lambda \gg l$ where λ is the wavelength of the incident beam and l is the interatomic distance.

- the *molecular dynamic region* or *mesoscopic regime* is investigated when $\lambda \approx l$.
- the *single-particle region* is investigated when $\lambda \ll l$

The study of the intermediate region, namely the mesoscopic regime, in which the momentum transfer becomes comparable to the inverse of the interparticle distances, is more difficult to interpret because the system cannot be treated neither as a continuum nor as composed of independent particles. This implies the development of a theory which is an extension of the hydrodynamic one and which is called *Generalized hydrodynamics*. Experimentally, inelastic x-rays (IXS) and neutrons scattering (INS) are particularly well suited to asses the microscopic dynamics at the atomic scale and then to investigate the mesoscopic region.
The aim of the following chapter is to remind the basic concepts and the basic equations which we will exploit to analyze and interpret the experimental data presented in this thesis. It is organized as follow:
in **Sec. 3.2** the basic analytical tools used to describe the dynamics of density fluctuations are introduced. Then we present a discussion on the main theoretical approaches to study the dynamics in different regions of the (Q, ω) plane, in particular:
in **Sec. 3.3** we consider the macroscopic hydrodynamic region where the system is viewed as a continuum isotropic medium and the excitation spectrum is well described within the Navier-Stokes hydrodynamic equations;
in **Sec. 3.4** we describe the mesoscopic region in which the momentum transfer becomes comparable to the interparticle distance. The spectrum of density fluctuations is described within the framework of generalized hydrodynamics whose formal results are obtained in terms of a memory function approach.
Sec. 3.5 is devoted to the presentation of this "memory function" based formalism. We provide both a qualitative and quantitative description of the relaxation processes in a liquid in terms of the memory functions, this allows us to derive those model functions that we will use to fit the IXS data.

3.2 Basic definitions

A great deal of information about static and dynamic properties of fluid systems are contained in the correlation function of the microscopic *number density* $\rho(\mathbf{r}, t)$ at the

point $\mathbf{r}$ defined as:

$$\rho(\mathbf{r},t) = \sum_i \delta(r - r(t))$$

it counts the number of particles in the neighbourhood of the point $\mathbf{r}$ at time t. Its auto-correlation function, the van Hove correlation function $G(\mathbf{r},t)$ is:

$$G(\mathbf{r},t) =< \rho^*(\mathbf{r},0)\rho(\mathbf{r},t) >$$

This represents the probability of finding a particle at position r at time t given that there was a particle at the origin at time t = 0.
The Fourier transform of $\rho(\mathbf{r},t)$ is:

$$\rho(\mathbf{Q},t) = \sum_i e^{i\mathbf{Q}\cdot\mathbf{r_i(t)}}. \tag{3.1}$$

Using this expression, the *intermediate scattering function* F(Q,t), which is a measure of the correlation between the Fourier components of the number density at two different times, is given by:

$$F(Q,t) =< \rho(\mathbf{Q},0), \rho(\mathbf{Q},t) > \tag{3.2}$$

The time Fourier transform of the intermediate scattering function F(Q,t), is the spectral function

$$\boxed{S(Q,\omega) = \tfrac{1}{2\pi}\int_{-\infty}^{\infty} F(Q,t)e^{-i\omega t}dt,} \tag{3.3}$$

generally referred to as *dynamic structure factor*. This is the function of main interest because it can be measured directly by scattering experiments. The time expansion of the intermediate scattering function F(Q,t) allows to obtain a description of the density correlation function. In particular the knowledge of the derivatives of static correlation functions is useful to get information on the dynamic correlation function F(Q,t) at short-times.

$$F(Q,t) = F(Q,0) + \frac{\partial F(Q,t)}{\partial t}|_{t=0}t + \frac{1}{2}\frac{\partial^2 F(Q,t)}{\partial t^2}|_{t=0}t^2 + \cdots$$

Since

$$F(Q,t) = \int_{-\infty}^{\infty} S(Q,\omega) e^{i\omega t} d\omega,$$

one has:

$$F(Q,0) = \int_{-\infty}^{\infty} S(Q,\omega) d\omega = S(Q)$$

$$\frac{\partial F(Q,t)}{\partial t}|_{t=0} = i \int_{-\infty}^{\infty} \omega S(Q,\omega) d\omega = 0$$

$$\frac{\partial^2 F(Q,t)}{\partial t^2}|_{t=0} = -\int_{-\infty}^{\infty} \omega^2 S(Q,\omega) d\omega = \frac{K_B T}{m} Q^2$$

where $\frac{K_B T}{M} = c_0^2$ is the thermal speed. The integrals in the previous expressions represent the *frequency moments* $\Omega^{2n}(Q)$ of $S(Q,\omega)$ defined as:

$$\boxed{\Omega_S^{2n}(Q) = (-1)^n \frac{\partial^{2n} F(Q,t)}{\partial t^{2n}}|_{t=0} = \int_{-\infty}^{\infty} \omega^{2n} S(Q,\omega) d\omega} \tag{3.4}$$

In the classical limit ($T \to \infty$) all odd moments are zero because of the even character in frequency of $S(Q,\omega)$ ($S(Q,\omega) = S(Q,-\omega)$). Thus

$$\begin{cases} \Omega_S^0(Q) = S(Q) \\ \Omega_S^1(Q) = 0 \\ \Omega_S^2(Q) = \frac{K_B T}{m} Q^2 \\ \vdots \end{cases} \tag{3.5}$$

These frequency moments or *sum rules* enable to write F(Q,t) as:

$$F(Q,t) = S(Q) - \frac{1}{2}\Omega_S^2(Q) t^2 + \frac{1}{4!}\Omega_S^4(Q) t^4 + \cdots$$

and to define the *normalized frequency moments* $\omega^{2n}(Q)$:

$$\boxed{\omega_S^{2n}(Q) = \frac{\Omega_S^{2n}(Q)}{S(Q)}} \tag{3.6}$$

The subscript $_S$ indicates that $\omega_S^{2n}(Q)$ are the normalized frequency moments of $S(Q,\omega)$. In next chapters the second frequency moment is indicated as follow:

$$\omega_S^2(Q) = \omega_0^2(Q) = \frac{K_B T}{mS(Q)} Q^2$$

where K_B is the Boltzman constant and m is the mass of the molecule. Using this approach, the expression of $F(Q,t)$ transforms into:

$$F(Q,t) = S(Q)[1 - \frac{1}{2}\omega^2(Q)t^2 + \frac{1}{4!}\omega^4(Q)t^4 + \cdots]$$

an important property can be extract from this expansion, which enables to formally write F(Q,t) in an exponential form as:

$$F(Q,t) \approx S(Q)e^{-\frac{\omega_0^2(Q)}{2}t^2}.$$

Consequently, its Fourier transform in frequency $S(Q,\omega)$ can be expressed as:

$$\frac{S(Q,\omega)}{S(Q)} = \frac{1}{\sqrt{2\pi\omega_0^2(Q)}} e^{-\frac{\omega^2}{2\omega_0^2(Q)}}$$

which allows to extract an approximative measure of the spectral width of $S(Q,\omega)$ from:

$$FWHM \propto (\omega_0^2(Q))^{1/2} = Q\sqrt{\frac{K_B T}{mS(Q)}}.$$

(Full Width at Half Maximum=FWHM) This behaviour is particularly interesting in the surrounding of the maxima of S(Q), because it explains the observed width reductions of $S(Q,\omega)$ when one approaches $Q \approx Q_m$, the maxima of the static structure factor (*de Gennes narrowing*)

Another important dynamical variable is the *current density*:

$$\mathbf{j}(\mathbf{Q},t) = \sum_i \mathbf{v}_i(t) e^{i\mathbf{Q}\cdot\mathbf{r_i(t)}}$$

where $\mathbf{v}_i(t)$ is the velocity of the the particle i. This variable is related to the general motion of the particles and the associated correlation function describing the flow of the particles in the direction of the wave-vector Q, is the *longitudinal current correlation function* defined as:

$$J_L(\mathbf{Q},t) = < \mathbf{j}_L(\mathbf{Q},0)^*, \mathbf{j}_L(\mathbf{Q},t) > .$$

This quantity is connected to the dynamic structure factor through the relation:

$$\boxed{S(Q,\omega) = \frac{\omega^2}{Q^2} J_L(\mathbf{Q},t)} \tag{3.7}$$

This is an obvious consequence of the continuity equation. The study of the maxima of this function enables to get information about the position of the inelastic peaks of $S(Q,\omega)$. The dynamic structure factor $S(Q,\omega)$ considered until now arises from Fourier transforms of the correlation function of a dynamical variable, the density, which has been considered as classical. For this reason we define the subscript cl, $S_{cl}(Q,\omega)$, to refer to the classical limit ($\hbar/T \to 0$). In this case $S_{cl}(Q,\omega)$ satisfies the relation [26]

$$S_{cl}(Q,\omega) = S_{cl}(-Q,-\omega)$$

The generalization to the quantum mechanical (q subscript) case, which is relevant whenever one considers excitations comparable or larger than the sample temperature, [2] requires that the $S_q(Q,\omega)$ fulfills the basic condition

$$S_q(Q,\omega) = e^{-\hbar\omega\beta} S_q(Q,-\omega).$$

This relation is referred to as the *detailed balance* condition, and is responsible for the asymmetry in ω of $S_q(Q,\omega)$ whenever $\hbar\omega > K_B T$. Since $S_q(Q,\omega)$ is the spectral distribution of the scattered radiation, positive frequencies describe a process in which the incident beam transfered energy to the fluid while negative frequencies describe a process in which the beam picked up energy from the system. The fulfillment of this relation is a check to test the validity of experimental data, the asymmetry of the scattered intensity is pronounced at low temperature and is negligible for hydrodynamic modes (Brillouin scattering) for which the frequencies are so small that the factor $e^{-\hbar\omega\beta}$ is about unity. The quantum and classical dynamic structure factors are related through the relation

$$S_q(Q,\omega) = \frac{\hbar\omega\beta}{1-e^{-\hbar\omega\beta}} S_{cl}(Q,\omega)$$

This is the expression we will use in the following chapters to fit experimental data.

3.3 Hydrodynamics

In a liquid the *hydrodynamic region* is investigated when the wavelength of the incident radiation is much larger than the intermolecular distance ($\lambda \ll l$) and on time scales that are very longer than the interatomic motion, and therefore $Q \to 0, \omega \to 0$. The details of the microscopic structure can be ignored and the liquid is regarded as a continuum. On this long-wavelength scale, the fluctuations involve the collective motion of large number of molecules and can be described by the laws of macroscopic physics. In this regime the variation of density fluctuations occurs very slowly in space and in time and the liquid is considered to be in local thermodynamic equilibrium. This is the central idea of hydrodynamics and allows writing macroscopic equations for local variables. In the region of visible light ($\lambda \sim 5000$) one fulfills the requirements for hydrodynamics to be valid , and therefore, a very useful technique to probe the longitudinal acoustic dynamics in this hydrodynamic region is Brillouin light scattering. In the hydrodynamic approximation, the line-shape of $S(Q,\omega)$ shows a characteristic triplet- the Brillouin triplet. To derive its origin we remind the classical treatment to understand the spectrum of scattered light.

The aim is to determine a theoretical expression for $S(Q,\omega)$, i.e. $< \delta\rho(\mathbf{Q},t), \delta\rho(0,0) >$, which is the quantity one obtains experimentally. In the case of a liquid in the hydrodynamic regime, a macroscopic treatment allow to get $\delta\rho(\mathbf{r},t)$ applying the conservation laws of density ρ, momentum $\mathbf{p}$ and energy e:

$$\dot{\rho}(\mathbf{r},t) + \bigtriangledown \cdot \mathbf{p}(\mathbf{r},t) = 0$$

$$\dot{\mathbf{p}}(\mathbf{r},t) + \bigtriangledown \cdot \sigma(\mathbf{r},t) = 0$$

$$\dot{e}(\mathbf{r},t) + \bigtriangledown \cdot \mathbf{J}(\mathbf{r},t) = 0$$

where σ is the momentum current or stress tensor and $\mathbf{J}$ is the energy current. This equations are solved by exploiting the macroscopic expressions for the stress tensor (Navier-Stokes) and energy current (Landau and Lifshitz 1963) and applying the Laplace-Fourier transform technique to solve a set of coupled equations. One achieves [27] the following expression for the dynamic structure factor in the hydrodynamic regime:

$$S(Q,\omega) = \frac{S(Q)}{2\pi}[\frac{\gamma-1}{\gamma}\frac{2D_TQ^2}{\omega^2+(D_TQ^2)^2} + \frac{1}{\gamma}(\frac{\Gamma Q^2}{(\omega+c_sQ)^2+(\Gamma Q^2)^2} + \frac{\Gamma Q^2}{(\omega-c_sQ)^2+(\Gamma Q^2)^2}) \tag{3.8}$$

$$+\frac{Q}{\gamma c_s}[\Gamma+(\gamma-1)D_T][(\frac{\omega-c_sQ}{(\omega+c_sQ)^2+(\Gamma Q^2)^2} + \frac{\omega+c_sQ}{(\omega-c_sQ)^2+(\Gamma Q^2)^2})] \tag{3.9}$$

where:

γ is the ratio of the specific heats at constant pressure and volume

$$\gamma = \frac{c_p}{c_v}$$

D_T is the thermal diffusivity

$$D_T = \frac{\lambda}{\rho c_v \gamma}$$

λ is the thermal conductivity, Γ is the sound attenuation coefficient

$$\Gamma = \frac{1}{2\pi}[D_t(\gamma-1)+\nu_L]$$

ν_L is the kinematic longitudinal viscosity

$$\nu_L = \frac{\eta_L}{\rho} = \frac{4/3\eta_S+\eta_B}{\rho}$$

c_s is the adiabatic sound velocity

$$c_s = \sqrt{\frac{\gamma}{\rho}(\frac{\partial p}{\partial \rho})}$$

The development of this theory is based on two assumptions used to simplify the calculations:

- the fluctuations of the density, energy, temperature and velocity around the equilibrium values are expected to be very small to allow the use of *linearized equations of the fluid mechanics*. This means that terms higher than the first order one (like $\delta\rho^2$) are neglected in the theory.

- the quantities $\gamma D_T Q^2$ and ΓQ^2 are considered much smaller than c_sQ. This means that the widths of the Lorentzians are small compared to the shifts.

The spectrum is composed by three Lorentzian lines and two non-Lorentzian contributions whose amplitude is much smaller compared to the other terms. The Lorentzian peak centered at $\omega = 0$ is called *Rayleigh line*, the two centered at $\omega = \pm c_s Q$ called *Brillouin-Mandelshtam lines* These three Lorentzian lines reflect the presence of three longitudinal modes, they represent two kinds of fluctuations:

- *adiabatic pressure fluctuations* which propagate in the liquid like sound waves with a sound velocity c_s (the reason because we call it adiabatic sound velocity), to them is associated the Brillouin-Mandelshtam doublet. These are propagating modes with a lifetime given by $(\Gamma Q^2)^{-1}$;
- *isobar entropy fluctuations* which do not propagate in the liquid, but are damped because of the thermal conduction. They are diffusive modes and are give rise to the Rayleigh lines.

In the case of Brillouin-Mandelshtam doublet or pressure fluctuations, two dissipative processes are involved due to viscosity and thermal conductivity. In the case of the Rayleigh line, the adiabatic fluctuations at constant pressure are damped only because of the thermal conductivity.
Although the two non-Lorentzian terms induce a slight asymmetry in the Brillouin peaks not appreciable experimentally, they are fundamental for the preservation of the sum rule $\Omega^1(Q) = 0$ calculated using the relation 3.5

3.4 Generalized hydrodynamics

The hydrodynamics description of a fluid is particularly effective at small wave-vectors and frequencies ($Q \to 0, \omega \to 0$). At decreasing wavelengths, namely, when they become comparable to the intermolecular distances, the hydrodynamic approach is no longer valid. This is a consequence of the fact that the derivation of the hydrodynamic theory is based on the assumption that the fluid is a continuous medium and each point in space and time is in thermodynamic equilibrium. An extension of the hydrodynamic theory is therefore necessary to study the fluctuations of hydrodynamic variables in a wider range of wave-vectors and frequencies. In particular, in the length-scale and timescale regions that are characteristic of the motion of a limited number of particles, the basic assumptions

of the hydrodynamic theory starts to fail. An attempt to extend the validity of the basic hydrodynamics theory at high frequencies and wave-vector is provided by the *generalized hydrodynamics*. The generalized hydrodynamics approach exploits the structure of hydrodynamic equations and extends them introducing a space and time dependence of the transport coefficients or, in the Fourier transformed space, a wave-vector (Q) and frequency (ω) dependence of the corresponding Fourier Transformed quantities. This phenomenological approach enables to achieve a generalized expression for $S(Q,\omega)$ valid in the high (Q, ω) region, and which reduces to the hydrodynamics theory expression in the $Q \to 0$ and $\omega \to 0$ limits. Given that the experimental techniques used to investigate the longitudinal acoustic dynamics in this region are inelastic x-rays scattering (IXS) and inelastic neutron scattering (INS), this generalized theory is important for us because it will allow to have analytical expression for the $S(Q,\omega)$ to fit our data. This in turn provides a test for the Generalized hydrodynamic theory and a mean to derive the high (Q,ω) limit of transport properties of the investigated fluid. An efficient approach to the generalization of the hydrodynamics is obtained by introducing a memory effect in the damping mechanisms of the longitudinal modes in the liquid. This requires the introduction of the *memory function formalism*.

3.5 Memory function formalism

The memory function approach, introduced by R. Zwanzig and H. Mori in 1960's, is used to describe time dependent phenomena in dense fluids. It has been initially introduced to extend the Brownian theory of self diffusion. We will use it here in order to show the results of generalized hydrodynamics. The aim is to calculate the spectrum of the correlation function of the density fluctuations. For this reason we start deriving the spectrum of the correlation function of a generic variable. In a system of N interacting particles the time evolution of a generic variable $A(t)$ is expressed by the equation of motion [27]:

$$\frac{dA(t)}{dt} = \{A, H\}(t) = iLA(t) \tag{3.10}$$

where H is the Hamiltonian of the system, the symbol $\{,\}$ denotes the Poisson bracket and L is the Liouville operator associated to the Hamiltonian

$$L = -i\sum_{i}^{3N}(\frac{\partial H}{\partial p_i}\frac{\partial}{\partial q_i} - \frac{\partial H}{\partial q_i}\frac{\partial}{\partial p_i})$$

where q_i and p_i are the generalized coordinates and conjugates momenta of the N particles. The formal solution of the equation 3.10 gives the time evolution of the variable A:

$$A(t) = e^{iLt}A(0)$$

The operator e^{iLt} is called *propagator*. The introduction of a projection operator P which projects an arbitrary vector onto A

$$P = \frac{\langle A(0)^*, ...\rangle}{\langle A(0)^*, A(0)\rangle}A(0)$$

and the application of the properties of the projection operators [27], allow to write the expression 3.10 as:

$$\boxed{\frac{dA(t)}{dt} = i\Omega A(t) - \int_0^t K(\tau)A(t-\tau)d\tau + F(t)} \tag{3.11}$$

known with the name of *generalized Langevin equation* : the term $i\Omega$ accounts for possible existence of a propagation process associated with the time evolution of the dynamical variable $A(t)$, while the integral plays the role of a systematic force and $F(t)$ represents a random force. The functions Ω, $F(\tau)$, $K(\tau)$ are defined as follow:

$$\Omega \equiv \frac{\langle A(0)^*, LA(0)\rangle}{\langle A(0)^*, A(0)\rangle} \quad \textit{frequency function} \tag{3.12}$$

$$F(t) \equiv e^{i(1-P)Lt}i(1-P)LA(0) \quad \textit{random force} \tag{3.13}$$

$$K(t) \equiv \frac{\langle F(0)^*, F(t)\rangle}{\langle A(0)^*, A(0)\rangle} \quad \textit{memory function} \tag{3.14}$$

$1-P$ is a projection operator which projects a generic variable onto a space orthogonal to A and $i(1-P)LA \equiv F(0)$. It is possible to show [27] that the random force $F(t)$ is orthogonal to $A(0)$. This property means that $\langle A(0)^*, F(t)\rangle = 0$ and points out a lack of correlation between $A(0)$ and $F(t)$.

Our interest here is to derive an equation describing the time evolution of the correlation function $C(t) = \langle A(0)^*, A(t) \rangle$ of the dynamical variable $A(t)$. This is easily obtained from equation 3.11 exploiting the fact that $\langle A(0)^*, F(t) \rangle = 0$:

$$\boxed{\frac{dC(t)}{dt} = i\Omega C(t) - \int_0^t K(\tau)C(t-\tau)d\tau} \tag{3.15}$$

This is called *memory function equation* . Both 3.11 and 3.15 are derived from 3.10 without any approximation.

These considerations made for a single property of the system can be generalized to the case of more variables by means of a vector

$$\mathcal{A} = \begin{vmatrix} A_1 \\ \vdots \\ A_M \end{vmatrix}$$

such that at equilibrium $\langle \mathbf{A} \rangle = 0$ and its components A_i cannot be expressed as linear combination of the others, namely, they are linearly independent. In this more general case the theory is reformulated in terms of column vectors and matrices. A formal solution to equation 3.15 is obtained by using the continued fraction representation. This useful method is presented in next section.

3.5.1 Continued fraction representation

The continued fraction representation is an important property of the memory function which enables to get an expression for the correlation function $C(t)$ of a generic dynamical variable $A(t)$. A more accurate analysis of the memory function equation :

$$\frac{dC(t)}{dt} = i\Omega C(t) - \int_0^t K(\tau)C(t-\tau)d\tau \tag{3.16}$$

allows to extract a solution using the Laplace transform technique:

$$z(C(z) - \frac{C(0)}{z}) = i\Omega C(z) + K(z)C(z) \tag{3.17}$$

which yields

$$C(z) = \frac{C(0)}{z - i\Omega + K(z)} \tag{3.18}$$

here $C(z)$ and $K(z)$ are respectively the Laplace transforms of $C(t)$ and $K(t)$ and $z = i\omega$. As a matter of fact, the memory function $K(z)$ is generally unknown. According to 3.14, the memory function $K(t) \equiv \frac{<F(0)^*, F(t)>}{<A(0)^*, A(0)>}$ is itself an autocorrelation function of the random force $F(t)$. This means that the same treatment applied for C(t) can be repeated for $K(t)$ simply rewriting a memory function equation for it:

$$\frac{dK(t)}{dt} = i\Omega_1 K(t) - \int_0^t d\tau M(\tau) C(t - \tau) \tag{3.19}$$

where $M(t)$ is the *second order memory function*. In this way the problem is shifted to the research of a new unknown memory function. The solution in terms of Laplace transform is identical to equation 3.18:

$$K(z) = \frac{K(0)}{z - i\Omega_1 + M(z)} \tag{3.20}$$

The substitution of this relation in 3.18 yields

$$\frac{C(z)}{C(0)} = \frac{1}{z - i\Omega - \frac{K(0)}{z - i\Omega_1 - M(0)}} \tag{3.21}$$

The process, iteratively repeated, gives an expression for C(z) in terms of *Continued Fraction Representation* (CFR)

$$\frac{C(z)}{C(0)} = \frac{1}{z - i\Omega - \frac{K(0)}{z - i\Omega_1 - \frac{M(0)}{z - i\Omega_2 - \cdots}}} \tag{3.22}$$

the coefficients K(0), M(0) can be expressed in terms of the normalized frequency moments ω_C^{2n} of $C(\omega)$ (appendix A)

$$\omega_C^{2n} = \frac{\int_{-\infty}^{\infty} \omega^{2n} C(\omega) d\omega}{\int_{-\infty}^{\infty} C(\omega) d\omega} \tag{3.23}$$

$$K(0) = \frac{\ddot{C(0)}}{C(0)} = \omega_C^2$$

$$M(0) = \frac{\ddot{K(0)}}{K(0)} = \frac{\omega_C^4}{\omega_C^2} - \omega_C^2 \tag{3.24}$$

At increasing of order it becomes more and more arduous to calculate the frequency moments and in addition the physical meaning of the considered correlation function starts to be lost. If we consider autocorrelation functions $C(t)$ even in time [27], the frequency functions Ω_n vanish because of time reverse symmetry and the 3.21 reduces to the following simplified expression:

$$\boxed{\frac{C(z)}{C(0)} = \cfrac{1}{z - \cfrac{K(0)}{z - \cfrac{M(0)}{z - \cdots}}}} \tag{3.25}$$

Thanks to the CFR it is possible to obtain a description of the correlation function C(t) introducing simple models for the memory function. The spectrum $C(\omega)$

$$C(\omega) = \frac{1}{2\pi}\int_{-\infty}^{\infty} e^{-i\omega t} C(t) dt \tag{3.26}$$

is finally obtained from $C(z)$ through the relation

$$C(\omega) = \frac{1}{\pi} Re C(z) \tag{3.27}$$

where Re represents the real part (see appendix B). In next section we will see an application of this formalism.

3.5.2 Memory function and density fluctuations

Let us apply the continued fraction representation to describe the density fluctuation dynamics of liquids. We consider as dynamical variable the density $\rho(r,t)$ and we apply the memory function formalism to its autocorrelation function. The previous equations are retained simply doing the following replacements

$$A(t) \rightarrow \rho(Q,t)$$
$$C(t) \rightarrow F(Q,t)$$
$$C(\omega) \rightarrow S(Q,\omega)$$

C(t) corresponds to the intermediate scattering function F(Q,t) defined by 3.28 and $C(\omega)$ corresponds to the dynamic structure factor defined by 3.3. In this specific case the equation 3.25 becomes:

$$\frac{F(Q,z)}{F(Q,t=0)} = \frac{1}{z - \frac{K(0)}{z+M(Q,z)}} \tag{3.28}$$

where $K(0)$ is the normalized second frequency moment of $S(Q,\omega)$, namely $\omega_0^2(Q) = [K_B T/mS(Q)]Q^2$, K_B is the Boltzmann constant, m is the mass of the molecule. Here only the second order memory function expansion has been considered. The spectrum 3.27 of $F(Q,t)$ corresponds to the dynamic structure factor:

$$S(Q,\omega) = \frac{1}{\pi} ReF(Q,z) \tag{3.29}$$

Since $F(Q,t=0) = S(Q)$, the substitution of 3.28 in 3.29 gives the expression of the dynamic structure factor as a function of the memory function M(Q,z)

$$\frac{S(Q,\omega)}{S(Q)} = \frac{1}{\pi} Re \frac{1}{z - \frac{\omega_0^2(Q)}{z+M(Q,z)}} \tag{3.30}$$

which yields:

$$\boxed{S(Q,\omega) = \frac{1}{\pi} S(Q) \frac{\omega_0(Q)^2 M'(Q,\omega)}{[\omega^2 - \omega_0(Q)^2 - \omega M''(Q,\omega)]^2 + [\omega M'(Q,\omega)]^2}} \tag{3.31}$$

where $M'(Q,\omega)$, $M''(Q,\omega)$ are respectively the real and the imaginary part of the Laplace transform of the memory function $M(Q,t)$

$$M(Q,z) = \int_0^\infty M(Q,t) e^{zt} dt = \int_0^\infty M(Q,t) cos(\omega t) dt - i \int_0^\infty M(Q,t) sin(\omega t) dt$$

$$\equiv M'(Q,\omega) - iM''(Q,\omega)$$

The experimental determination of the dynamic structure factor gives information on the memory function contributing to the general understanding of the dynamics of density fluctuations. The choice of simple models for the memory function is the result of a compromise between physical intuition and mathematical simplicity of the calculations. The main requirements about the model for the memory function $M(Q,t)$ are:

1. analytical simplicity;

2. least violation of the sum rules 3.5

3. easy interpretation of the physical meaning of the analytical results.

3.5.3 Memory function and relaxation processes

A marked characteristic of the liquid state is that the dynamics of the density fluctuations is controlled by relaxation processes. For example, in liquids, the structural rearrangement of the particles takes place with a characteristic time-scale, τ_α, dictated by the local inter-particles interaction and the actual thermodynamic state. The presence of these re-arrangements affects the dynamics of the density fluctuations as it allows energy exchanges between different density fluctuation modes. In this context, one calls *relaxation process* the mechanism governing these energy flows, and, in this specific example, we have described the well known *structural- or α-relaxation process* [28] we will illustrate better in the following. Other relaxation processes may be active, each one characterized by a specific underlying physical mechanism. One of the open problems in the physics of the liquid state is to understand on a general ground the common features of these relaxation processes. In simple monatomic liquids both kinetic and mode-coupling theories predict the existence of two distinct relaxation processes [2] and, this prediction has been demonstrated both by numerical simulations [3, 4] and by experiments [5]. In these theories, one of the two processes is the α-relaxation, and the other is a faster process (*microscopic* or *instantaneous* process) which is thought to be associated with the interactions between an atom and the "cage" of its nearest neighbours. Other relaxation processes, beyond the α and the instantaneous processes, associated with the internal molecular degrees of freedom may be observed in molecular liquids. In glass-forming systems, one also finds the same relaxation processes pattern. In this case, by driving the system to the glassy state, where the structural arrest freezes the α-process and τ_α becomes extremely large, is still possible to clearly observe the microscopic process [6]. An effective experimental method to study and identify relaxation processes is the determination of the dynamic structure factor, $S(Q,\omega)$, and, in particular its inelastic features due to collective excitations which, at momentum transfer Q, are observed at energy $\hbar\Omega(Q)$. The dispersion relation of $\Omega(Q)$ allows to define an "apparent" sound velocity, $c(Q) = \Omega(Q)/Q$, which is a constant in the low Q-limit, and decreases with Q approaching the inverse of the inter-particle distance d. Whenever a relaxation process with characteristic time τ is active, $c(Q)$ has a

further Q-dependence which shows up as a transition from a low frequency value, c_o, to a high frequency one, c_∞. This transition takes place when the condition $\Omega(Q) \approx 1/\tau$ is fulfilled. The amplitude of the jump between c_∞ and c_o is related to the strength, Δ, of the coupling between the density fluctuations and the degrees of freedom involved in the relaxation process. Multiple relaxation processes will give rise to multiple "jumps" in $c(Q)$ (Figure 3.1). We describe in the following the thermal, the structural and the microscopic relaxation processes and the analytical way to take them into account in the description of the dynamic structure factor.

Thermal relaxation

The propagation of a compressional wave in a liquid generates a periodic variation of pressure at any point and thus very rapid oscillations of the local temperature. This happens because in all pure liquids, the specific heat at constant pressure c_p exceeds that at constant volume c_v ($\gamma = c_p/c_v > 1$) hence heat flows from an hotter and compressed region to a cooler and less dense one. The passage of a wave determines therefore an energy transfer from the wave packet to the energy of the liquid, *i.e.* the compressional wave at some point is absorbed. The two properties of the liquid governing this energy absorption are the viscosity and the thermal conductivity. Viscous losses take place because of the shearing motion of the propagating longitudinal plane wave and thermal absorption is due to the heat flow since all liquids are thermally conductive. The combined effect of viscosity and heat conduction is generally referred to as *classical absorption*. Except for liquid metals, which have high heat conductivity, the role played by heat conductivity is small compared to that played by viscosity [**?**]. However measurements of this kind of absorption in many liquids showed that the experimental value is higher than the classical absorption, the difference is called *excess absorption* and is related to the bulk viscosity associated with the compression of the liquid. This excess absorption or η_B implies further mechanisms of energy losses which have been thought to be of relaxational nature. Thermal relaxation effects are observed in a liquid in which exchanges between external and internal degrees of freedom require a finite time characteristic of the nature of the process. Thermal relaxation occurs when the acoustic energy is taken up by one of the internal modes. For liquids in which thermal relaxation plays the important role there is no obvious correlation between the temperature dependence of η_B and η_S and the

ratio η_B/η_S is often very high (> 20) [?]. In addition, in the case of thermal relaxation a velocity dispersion is observed in the relaxation region with a difference between the high and low-frequency sound speed of the order of 5-10% [29]. Since to reveal a relaxation the frequency domain investigated has to be of the same order of magnitude of $1/\tau$ (best coupling-see below), and since the thermal relaxation time for several liquids is of the order of $10^{-10}s$ (GHz range in the frequency domain), the light scattering is probably the best probe to study thermal relaxations. This relaxation manifests in the Brillouin light scattering spectrum with a further contribution centered at zero energy transfer in addition to the central elastic line (Rayleigh) and the inelastic doublet (Brillouin-Mandelstam). It is referred to as Mountain peak because it was initially predicted by Mountain [30](1966)

Structural relaxation

The structure of the liquid state is characterized by the lack of long-range order and changes in pressure and temperature correspond to changes in its local of order. If a variation of the structural state takes place, changes in the interactions between the molecules, due to structural rearrangements, implies lost or gain of energy. As a consequence, the specific heat c_p of the liquid is higher compared to the one of the solid because of the presence of these structural contributions. The same happens for the compressibility χ and the expansion coefficient α. To study how structural effects influence the properties of a liquid, it is necessary to probe the system in a time scale slower compared to the relaxation time of the structural process. There are two operational methods to proceed: the first corresponds to make a systematic study of the system by changing the temperature, the second is to investigate the system response in different frequency domains and therefore using radiation probes of different energies. In the first case in fact a decrease in temperature induces an increase of the relaxation time. The relaxation can be classified on the base of the relationship between the period (T) of the sound wave and the relaxation time τ characteristic of the process. The so-called *viscous regime* is probed whenever $T \gg \tau$. In this regime, the rearrangements (relaxation) can be regarded as instantaneous processes. Consequently the acoustic propagation takes place along different states of equilibrium (adiabatic approximation). If on the contrary $T \ll \tau$, the rearrangement process is very slow and the fluid response turns out to be "frozen". Within this short time scale the perturbation induced by the sound wave propagates elastically. This is the so-called *elastic*

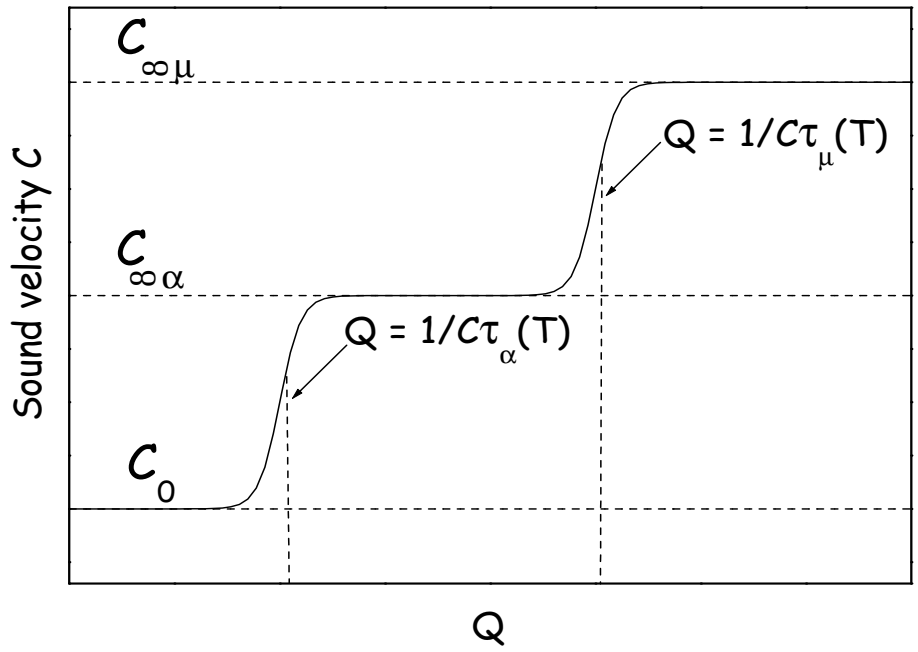

Figure 3.1. behaviour of the sound velocity as a function of Q the doted lines are the zero and infinite frequency limiting value.

regime. In the intermediate region the dynamical behaviour is usually called *viscoelastic* . Here the dynamics of sound propagation strongly depends on the (Q,ω) of the probed density wave. In a fluid perturbed by an acoustic propagation, local changes in pressure make the particles to move from high-density regions to low density ones to restore an equilibrium configuration. The structural relaxation is therefore the result of structural rearrangements of the system because of local changes in density and temperature. It is typical of highly viscous fluids and is strongly temperature dependent. The "structural" rearrangement of the system is not achieved instantaneously but in the simplest case, in an exponential way.

Microscopic relaxation

The relaxation processes introduced above are respectively of thermal and viscous nature: the thermal relaxation is due to the coupling of density fluctuation with the internal degrees of freedom, the structural relaxation is due to structural rearrangement of the particles. Besides the structural relaxation another viscous relaxation process has to be

taken into account. This is the *microscopic* relaxation process known also as *instantaneous* or *μ-process*. It is thought to be associated with the interaction of an atom and the cage of its neighbours. It represents the relaxation of the oscillatory motion of a tagged particle in its first solvation shell. When the cage particles move, they allow the tagged (in-cage) particle to diffuse. This additional viscosity relaxation is not cooperative, is temperature independent and is faster compared to the structural one. It lies in the 10^{-13} s time-scale. As already described at the beginning of this section we are able to identify a relaxation process looking to the jumps of the sound velocity. In the case of α- and μ- relaxation processes, one expects that $c(Q)$ goes from c_o to $c_{\infty\alpha}$ because of the α-process, and then from $c_{o\mu} = c_{\infty\alpha}$ to c_∞ because of the μ-process, being this order based on the observation that τ_α is always larger than τ_μ (Figure 3.1).

The analytical way to take into account a relaxation process is to introduce memory function ansatzs able to describe the different decay channels. In particular the three relaxation processes: thermal, structural and microscopic are introduced in the theory by considering the memory function as composed of three contributions. We indicate the thermal part with the subscript $_{TH}$, the structural part with α and the microscopic part with μ as follow:

$$M(Q,t) = M_\alpha(Q,t) + M_\mu(Q,t) + M_{TH}(Q,t)$$

These contributions can be further divided into two subgroups which emphasize two different relaxation mechanisms: the first of viscous nature, including the α and the μ process and the second of thermal character describing the coupling of the density fluctuation to the thermal modes. This allow to write the previous memory function as:

$$M(Q,t) = M_L(Q,t) + M_{TH}(Q,t)$$

where the subscripts $_L$ refers to longitudinal and $M_L(Q,t) = M_\alpha(Q,t) + M_\mu(Q,t)$. An expression for the memory functions can be obtained by imposing that in the low Q limit, $Q \to 0$, $F(Q,s)$ or $S(Q,\omega)$ in 3.28 and 3.31 reduces to the hydrodynamic expressions. This yields for the thermal contribution $M_{TH}(Q,t)$

$$M_{TH}(Q,t) = (\gamma - 1)\omega_0^2(Q)e^{-D_T Q^2}$$

$$M(Q,t) = M_\alpha(Q,t) + M_\mu(Q,t) + (\gamma - 1)\omega_0^2(Q)e^{-D_T Q^2}$$

where $\gamma = c_p/c_v$ is the specific heat ratio, $\omega_0^2(Q) = [K_B T/mS(Q)]Q^2$ is the normalized second frequency moment defined in 3.5 D_T is the thermal diffusivity. If $\gamma \approx 1$, which is the physical case we analyze in next chapters, this term can be neglected.

3.5.4 Damped Harmonic Oscillator (DHO) model

In the one relaxation process scenario, the simplest model for $M_L(Q,t)$ is the δ-function behaviour or *Markovian approximation*:

$$M_L(Q,t) = 2\Gamma(Q)\delta(t) \tag{3.32}$$

It takes into account all the fast processes which characterize the dynamics at short times. Its Laplace transform:

$$M_L(Q,z) = \Gamma(Q)$$

allows to extract the real $M_L'(Q,\omega) = \Gamma(Q)$ and the imaginary part $M_L''(Q,\omega) = 0$ to be inserted in the equation 3.31 which transforms in:

$$S(Q,\omega) = \frac{S(Q)}{\pi}\frac{\Omega^2(Q)\Gamma(Q)}{[\omega^2 - \Omega^2(Q)]^2 + [\omega\Gamma(Q)]^2} \tag{3.33}$$

this expression is referred to as the damped harmonic oscillator (*DHO*) for $S(Q,\omega)$. It shows inelastic side peaks at

$$\omega_{peak} = \pm\omega_0\sqrt{1 - \frac{\Gamma^2(Q)}{2\Omega^2(Q)}}$$

To understand the physical meaning of the parameters $\Omega(Q)$ and $\Gamma(Q)$ entering in the DHO model, we compare 3.33 with

$$S(Q,\omega) = \frac{S(Q)}{\pi}\frac{2\Gamma Q^2[(c_s Q)^2 + (\Gamma Q^2)^2]}{[\omega^2 - (c_s Q)^2 - (\Gamma Q^2)^2]^2 + [2\Gamma Q^2\omega]^2} \tag{3.34}$$

which is the inelastic part of the hydrodynamic $S(Q,\omega)$ 3.9 with $\gamma \approx 1$. Eq. 3.33 and 3.34 match only if the following requirements are satisfied:

$$\begin{cases} \Gamma(Q) = 2\Gamma Q^2 = \nu_L Q^2 \\ \Omega^2(Q) = (c_s Q)^2 + (\Gamma Q^2)^2 \end{cases} \tag{3.35}$$

This shows that the parameter $\Gamma(Q)$ provides informations on the kinematic longitudinal viscosity ν_L and the parameter $\Omega(Q)$ provides informations on the adiabatic sound velocity in the limit

$$\Gamma Q^2 \ll c_s Q$$

This also point out that the results of hydrodynamics can be formally deduced by a microscopic memory function approach with a memory function $M_L(Q,t)$ such that:

$$M_L(Q,t) = 2\nu_L Q^2 \delta(t)$$

This simple model, valid in the low Q limit, will be used in part, to extract the values of the parameters for the spectra presented in next two chapters.

3.5.5 Viscoelastic model

Aiming to describe the dynamics of density fluctuations at increasing wave-vectors the further step is the introduction of a memory function with a finite characteristic decay time. The simplest approximation is an exponential decay or Debye ansatz:

$$M_L(Q,t) = \Delta^2(Q) e^{-t/\tau(Q)} \tag{3.36}$$

where, according to relation 3.24, $\Delta^2(Q)$ is defined by

$$\Delta^2(Q) = M(Q,t=0) = \frac{\omega_S^4(Q)}{\omega_0^2(Q)} - \omega_0^2(Q) \equiv \omega_\infty^2(Q) - \omega_0^2(Q)$$

The equation 3.36 is generally referred to as *viscoelastic model* for $S(Q,\omega)$. This simple model accounts for the analitical semplicity in the calculation of $S(Q,\omega)$ and preserves the fourth frequency moment ω_S^4 of $S(Q,\omega)$. It is expected to give a resonable description of the dynamical behaviour of the system when Q approaches the first maximum Q_m of the static structure factor $S(Q)$.
The expression for the dynamic structure factor is achieved by introducing the real $M_L'(Q,\omega)$ and the imaginary $M_L''(Q,\omega)$ part of the Laplace transform of the memory function 3.36 in 3.31:

$$M(Q,z) = \frac{\Delta^2(Q)}{z + \frac{1}{\tau(Q)}}$$

$$M'_L(Q,\omega) = \Delta^2(Q)\frac{1}{\omega^2\tau(Q)^2+1}$$

$$M''_L(Q,\omega) = \Delta^2(Q)\frac{\omega}{\omega^2\tau_\alpha(Q)^2+1}$$

The low wave-vectors and low frequencies ($Q \to 0$, $\omega \to 0$) limits of $M(Q,z)$ gives $M(Q \to 0, z \to 0) = \Delta^2(0)\tau(0)$. A comparison with the hydrodynamic expression of the memory function $M(Q \to 0, z) = \Gamma(Q \to 0) = \nu_L Q^2$, allows to extract a finite value for the relaxation time $\tau(0)$

$$\tau(0) = \frac{\nu_L Q^2}{\Delta^2(0)}$$

The values of τ evaluated with this relation lies in the subpicosend time scale for simple liquids. Although for Q values such that $Q \approx Q_m$ the viscoelastic model is in good agreement with the experimental results [31, 32], it starts to fail for smaller wave-vectors as shown for liquid alkali metals [2, 5]. The failure has been attributed to the neglect of additional relaxation processes which make the single time description break down.
This is the case, for example, of simple monatomic liquids in which the presence of two distinct relaxation processes is predicted [2, 3, 4, 5]: one of the two processes is the structural or α-relaxation, and the other is the faster process, the microscopic or μ whose physical meaning has previously been described. In the two relaxation processes scenario, we model $M_L(Q,t)$ by the sum of two exponential decay contributions:

$$M_L(Q,t) = \Delta^2_\alpha(Q)e^{-t/\tau_\alpha(Q)} + \Delta^2_\mu(Q)e^{-t/\tau_\mu(Q)} \tag{3.37}$$

where $\Delta^2_\alpha(Q) = [c_{\infty\alpha}(Q)^2 - c_0(Q)^2]Q^2$, and $\Delta^2_\mu(Q) = [c_\infty(Q)^2 - c_{\infty\alpha}(Q)^2]Q^2$ are the strengths of the two processes. When the μ-process is very fast with respect to the investigated timescale, like it happens for example in liquid water [1], one expects that the second term of 3.37 is approximated by a δ-function and the $M_L(Q,t)$ transforms in:

$$M_L(Q,t) = \Delta^2_\alpha(Q)e^{-t/\tau_\alpha(Q)} + \Gamma_\mu(Q)\delta(t) \tag{3.38}$$

with $\Gamma_\mu(Q) = \Delta^2_\mu\tau_\mu(Q)$. Its Laplace transform:

$$M_L(Q,z) = \frac{\Delta^2(Q)}{z+\frac{1}{\tau_\alpha(Q)}} + \frac{\Gamma_\mu(Q)}{2Q^2}$$

allows to obtain the expression for $S(Q,\omega)$ In the the low Q, low ω hydrodynamic region, we have $M_L(Q \to 0, z \to 0) = (\omega_\infty^2(0) - \omega_0^2(0))\tau_\alpha(0) + \frac{\Gamma_\mu(0)}{2Q^2}$ which compared with the hydrodynamic one $M(Q \to 0, z) = \Gamma(Q \to 0) = \nu_L Q^2$, enables to extract an expression for the relaxation time in the two relaxation processes scenario:

$$\tau_\alpha(0) = \frac{\nu_L - \frac{\Gamma_\mu(0)}{2Q^2}}{c_{\infty\alpha}^2(0) - c_0^2(0)} \tag{3.39}$$

ν_L and c_0 are respectively the kinematic longitudinal viscosity and the adiabatic sound velocity. We will use this last model to analyze the experimental spectra presented in the following chapters.

Chapitre 4

La dynamique aux hautes fré quences de beaucoup de systè mes liquides a é té é tudié e soit expé rimentalement par diffusion iné lastique des rayons X (IXS) et par diffusion Brillouin de la lumiè re (BLS) soit numé riquement par des simulations de dynamique molé culaire (MD). Un grand effort a é té fourni pour comprendre comment les proprié té s dynamiques des diffé rents liquides dé pendent du potentiel d'interaction caracté ristique des systè mes é tudié s. Une attention particuliè re a é té porté e aux gaz nobles et aux liquides mé talliques : pour les premiers les interactions entre les particules sont habituellement modé lisé es avec les potentiels Lennard-Jones, alors que pour les seconds elles sont modé lisé es avec des pseudo-potentiels. Une autre classe trè s importante de liquides à considé rer sont les systè mes à liaison hydrogè ne. Ils sont d'un é norme inté rt à cause de la forte influence de la liaison hydrogè ne sur leurs proprié té s microscopiques. En effet ils sont caracté risé s par une interaction entre les particules hautement directionnelle due à la pré sence de cette liaison. Il serait trè s inté ressant d'é tablir une connexion entre les proprié té s dynamiques de ces systè mes et le type d'agré gat a liaison hydrogè ne spé cifique du systè me. Afin d'introduire ces systè mes nous pré sentons dans ce chapitre un bref ré sumé de notre connaissance actuelle de leur comportement. Le chapitre est organisé comme suit :

dans le Par. 4.2 est donné e une description gé né rale des systè mes à liaison hydrogè ne et de leurs principales proprié té s.

Le Par. 4.3 est dé dié au systè me à liaison hydrogè ne le plus é tudié : l'eau.

Dans le Par 4.4 afin de caracté riser la dynamique à hautes fré quences des systè mes à liaison hydrogè ne, nous introduisons les deux liquides sujets de cette thè se : l'acide fluorhydrique (HF) et les solutions $(HF)_x(H_2O)_{1-x}$.

Chapter 4

Collective dynamics in hydrogen bonded liquid systems

4.1 Introduction

The collective dynamics of many liquid systems has been investigated both experimentally by inelastic neutron scattering (INS), inelastic X-rays scattering (IXS) and Brillouin light scattering (BLS) and numerically by molecular dynamic simulations (MD). A big effort has been done to understand how the dynamic properties of different liquids depend on the characteristic interparticle interaction potential of the system under study. In this respect particular attention has been payed to noble gases and liquid metals. The interparticle interaction for the former are usually modeled by Lennard-Jones potentials whereas the latter are represented in terms of pseudo-potentials. Another very important class of liquids to consider are the hydrogen bonded (HB) liquid systems. The enormous interest is found in the strong influence of hydrogen bond on their microscopic properties. In fact they are characterized by a highly directional interparticle interaction due to the HB. It is intriguing to establish a connection between the dynamical properties of these systems and the specific HB arrangement. In order to give a basic insight into the collective dynamics of hydrogen bonded liquids we present in this chapter a brief summary on our actual understanding on their behaviour. It is organized as follow:
in **Sec. 4.2** a general description of the HB systems together with their main properties is reported.
Sec 4.3 is devoted to the most studied HB liquid system: water.

In **Sec 4.4**, aiming to characterize the high frequency dynamics of HB liquid systems, we introduce the two HB liquids subject of the investigations of this thesis work, hydrogen fluoride (HF) and $(HF)_x(H_2O)_{1-x}$ solutions. We illustrate the general open questions related to the relaxation phenomena in highly associated liquids.

4.2 Hydrogen bonded systems

The physical and chemical properties of a system are largely determined by the character and strength of the intermolecular interactions. For instance, the very specific properties of liquid water find their origin in the very strong hydrogen-bond interactions between water molecules. For this reason, many studies have been devoted to the structure and dynamics of the hydrogen-bond network in highly associated liquids. The concept of *hydrogen bond* is based on the fact that electronegative atoms such as N, O, F and Cl, pull the distribution of electrons away from other less electronegative atoms bound to them through covalent bonds. This creates slightly positive polar atoms which are attracted to the slightly negative ones. This dipolar attraction forms the basis of hydrogen bonding. In 1920 *W. M. Latimer* and *W. H. Rodebush* [33] recognized the importance of the hydrogen bond and of its extensive occurrence. They used this concept to discuss the properties of highly associated liquids such as water and hydrogen fluoride. They attributed to it the cause of association of water and of its unique chemical and physical properties. "Water...shows tendencies both to add and give up hydrogen, which are nearly balanced. Then...a free pair of electrons on one water molecule, might be able to exert sufficient force on a hydrogen held by a pair of electrons on another water molecule to bind the two molecules together... Indeed the liquid may be made up of large aggregates of molecules, continually breaking up and reforming under the influence of thermal agitation. Such an explanation amounts to saying that the hydrogen proton, held between 2 octets, constitutes a weak bond". According to *L. Pauling* [34] "...under certain conditions an atom of hydrogen is attracted by rather strong forces to two atoms, instead of only one, so that it may be considered to be acting as a bond between them". The result is the formation of a *hydrogen bridge* between two neighbour molecules, for that also the name hydrogen bridge has been used. The hydrogen bond is a weak bond, its strength is about 20 times lower than a covalent bond and its energy lies in the range of $2 \div 10 Kcal/mole$. Because of its small bond energy and the small activation energy involved in its formation and rupture, it plays

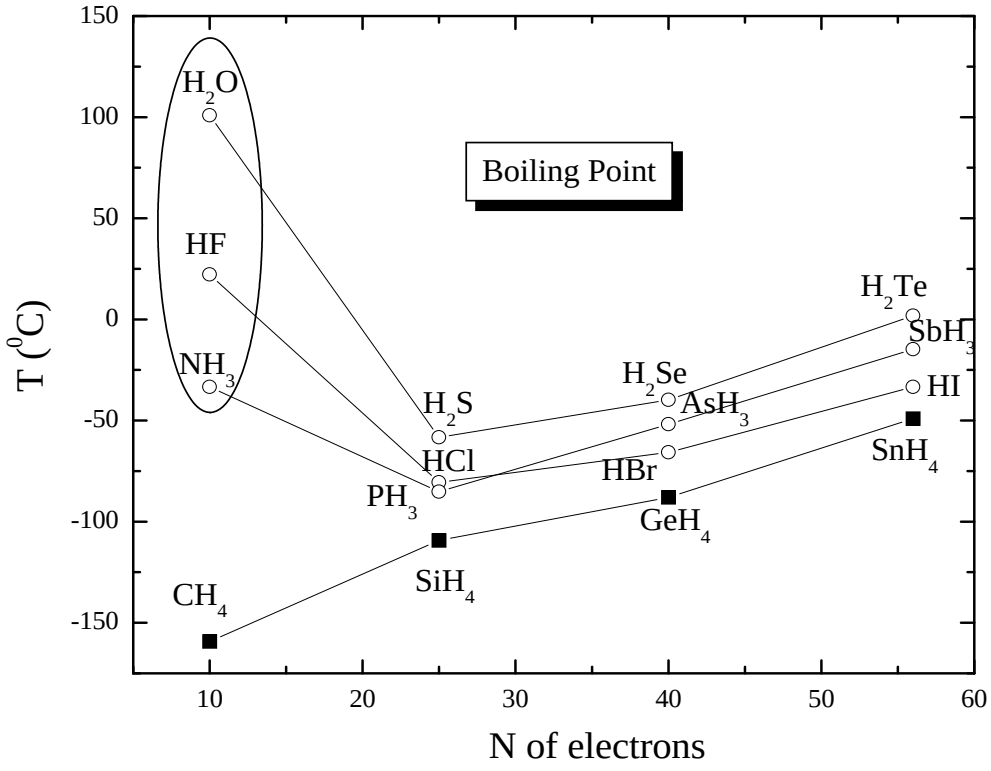

Figure 4.1. Boiling point of hydrides of elements of the same Group of the periodic table [35].

an important role in reactions at room temperature. An increasing electronegative atom, has an increase capacity to form hydrogen bonds. Even if the H-bond involves association of two molecules, the resulting H-bonded complexes are not limited to dimeric linkages; in liquid water and hydrogen fluoride (HF), for instance, multiple bonded arrangements occur. In general the formation of hydrogen bonds in a compound or in a solution may produce chains, rings or three dimensional networks with a consequent alteration of the mass, size, shape and arrangements of the aggregates.

In Figure 4.1 the boiling point of *hydrides* (elements which form compounds with hydrogen) is plotted to show how the presence of the H-bond affects this property in compounds of the most electronegative atoms (NH_3, H_2O, HF).

In addition to inorganic compounds also all the organic molecules containing the group O-H (hydroxyl group) (like methanol, ethanol, formic acid, acetic acid) and the group N-H (like methylamine) are capable of hydrogen bonding. In this thesis one of the most

strongly associated liquids has been considered: hydrogen fluoride (HF). It is one of the simplest model system and apart from its importance as prototype system, it plays an important role in many technical applications as solvent for chemical reactions and etching processes. Because of its high reactivity, the structural and dynamic properties of HF, are much less known than those of water. In the following table we resume the main features of this two systems in terms of H-bond

hydrogen fluoride (HF)	water (H_2O)
1 H-bond for each molecule	2 H-bonds for each molecule
linear chain like arrangement	three dimensional arrangement
H-bond energy $\approx 28 KJ/mole$	H-bond energy $\approx 20 KJ/mole$

4.3 The water case: a recall

In the framework of hydrogen bonded liquids, water has been extensively investigated; we give here a brief report on previous studies and on the current understanding of its collective dynamics. One of the peculiarity of this liquid is the phenomenon of *fast sound*: the existence of high frequency collective excitations which propagate with a velocity much higher than that of the ordinary sound up to momentum transfers comparable with the inverse of the intermolecular average distance. This finding, highly controversial at the time of its discovery, as we will see, is in fact the fingerprint of a very strong relaxation process active in water and associated with the HB. It was observed for the first time by Rahman and Stillinger in 1974 [36] who studied the dynamic structure factor $S(Q,\omega)$ of this liquid by molecular dynamic simulations. They found the existence of two propagating modes with sound velocity of 1500 m/s and 3000 m/s respectively. The first experimental evidence of fast sound in water came out from inelastic neutron scattering (INS) experiments [37] which found a sound excitation propagating with a velocity of $\approx 3300 m/s$ in a momentum transfer range of $3.5 \div 6 nm^{-1}$. The main disadvantage of this experiment was the reduced (Q,ω) region explored because of the kinematic limitations of the neutron scattering technique. This didn't allow to observe the mode at lower energy. An important contribution in this direction came from the development of the inelastic x-ray scattering (IXS) technique [24, 25, 39]. It gave the possibility to study the dynamic structure factor of water exploiting some very important advantages: first among all the possibility to investigate a much wider (Q,ω) region. This measurements

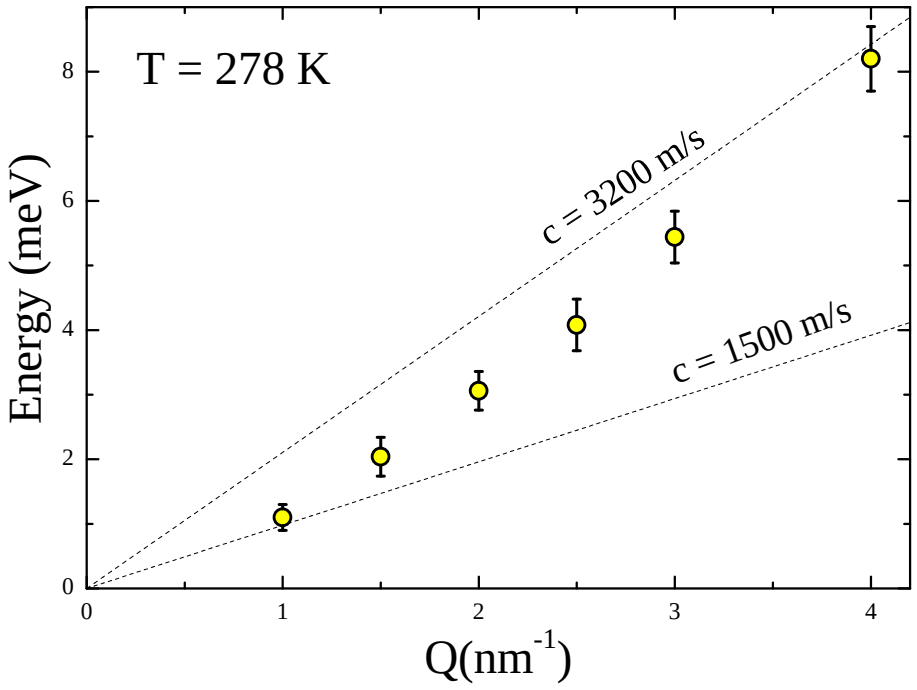

Figure 4.2. Dispersion curve for water at the indicated temperature obtained by IXS [38]. The upper dotted line is the linear fit to the data in the $4 \div 10 nm^{-1}$ Q range [38], the lower dashed lines indicated the adiabatic sound velocity.

confirmed those previously done with INS and demonstrated the presence of fast sound in a wider momentum transfer region $4 \div 10 nm^{-1}$. It also showed (Figure 4.2) that in the Q region comprised between $1 nm^{-1}$ and $4 nm^{-1}$ the velocity of sound of the longitudinal acoustic excitations undergoes a characteristic dispersion, similar to that pictorially reported in Figure 3.1. This accounted for the highly discussed difference between the low frequency and high frequency sound velocities in liquid water. A similar behaviour was already observed in many glass forming liquids [] in which such transition is observed in presence of an α-relaxation (see Section 3.5.3) and takes place at a Q-value such that the condition $\omega\tau_\alpha \approx 1$ is fulfilled, where ω is the frequency of the sound excitation and τ_α is the structural relaxation time.

To better understand the origin of this phenomenon in water, further studies as a function of temperature, density and pressure were done [40]. They showed that the transition from the hydrodynamic sound velocity to the high frequency limit takes place at a Q value which is temperature dependent. In particular increasing temperature, the transition

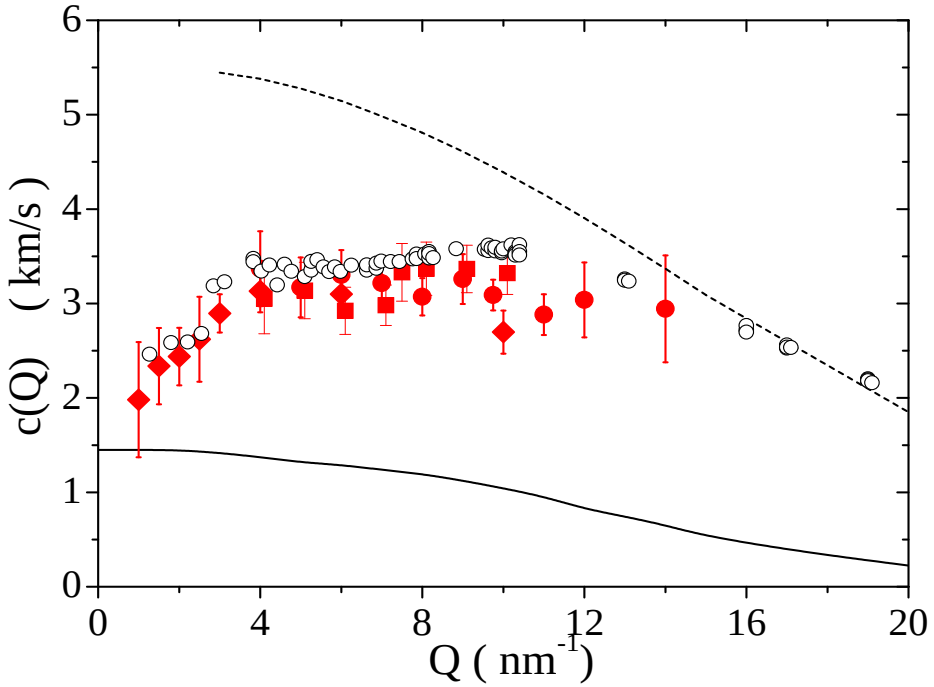

Figure 4.3. Q dependence of experimental and theoretical velocities of sound in water. Open circles, MD simulations [42]; full squares, circles and diamonds, IXS data [38]; solid (dashed) line, zero (infinite) frequency limit [43].

takes place at increasing Q. This demonstrate the presence of a relaxation process whose phenomenology is consistent with the one of the structural or $\alpha-$relaxation typic of glass-forming systems [41]. At variance with them, for which the structural relaxation time τ_α is typically studied at temperatures such that its value is of the order of nanosecond (10^{-9} s), in water τ_α lies in the sub-picosecond (10^{-12} s) region and lower values are prevented by the nucleation of the crystalline state upon cooling. This small values for τ make the condition $\omega\tau \approx 1$ to be met at tera-hertz frequencies and therefore it can be studied experimentally with the IXS method. It has been found that τ_α follows an Arrhenius behaviour and the derived activation energy is comparable to the energy of the hydrogen bond in water. This has led to think that this relaxation is associated to the rearrangements of the molecular structure and in particular of the hydrogen bonded clusters in the liquid.

A summary of our current understanding of the collective dynamics in terms of apparent sound velocity is reported in Figure 4.3 . Experimental and numerical simulation data

points for ambient conditions fall between the $c_o(Q)$ and $c_\infty(Q)$ curves determined by computer simulations. We observe a positive dispersion of $c(Q)$ from $c_o(Q)$ ($\approx$1500 m/s at $Q = 0$) to a value of $\approx$ 3200 m/s in the Q region Q=2$\div$4 nm^{-1}. Extensive temperature and density dependent studies have shown that this positive dispersion is associated to the structural relaxation process [28]. It is then tempting to cast the water case in the general relaxation frame introduced in the previous chapter. In particular:

1. it is important to better understand the relation between a network of hydrogen bonds in presence of structural relaxation ($\alpha-$process);

2. In the case of water, there is still a large difference between $c_{\infty\alpha}(Q) = 3200m/s$ and $c_\infty(Q) = 5000m/s$ at Q=6 nm^{-1}. Can this difference be interpreted as due to the microscopic relaxation (μ-process)? This observation, evident in the low Q region, is less obvious at large Q where the difference between $c_{\infty\alpha}$ and $c_\infty(Q)$ is much smaller.

4.4 The hydrogen fluoride (HF) case: open questions

Besides water, many other liquid systems of organic and inorganic nature are characterized by hydrogen bond. The structural and dynamic properties of these liquids are strongly influenced by the strength and the number of the hydrogen bonds between nearest neighbour molecules. Aiming to characterize the relaxation phenomena of the associated liquids, the present work has been devoted to make a comparative study of water and other hydrogen bond liquids. In this respect we have chosen pure hydrogen fluoride (HF), the inorganic system with the strongest hydrogen bond and $(HF)_x(H_2O)_{1-x}$ solutions. The main difference between HF and H_2O is the uni-dimensional vs. three-dimensional nature of the HB network. Consequently is of great interest to determine the evolution of the collective dynamics from the phenomenology of one liquid to that of the other. As in water in fact, one may expect to observe the phenomenon of fast sound probably associated with the structural rearrangement of the hydrogen bond network characteristic of the liquid. Several open questions are related to this **structural relaxation**:

- The first concerns the *time scale* of the relaxation: in water in fact, the relaxation time associated to the structural process lies in the sub-picosecond region. This is the same order of magnitude of the lifetime of the H-bond. *Is the structural relaxation time in hydrogen bonded liquid systems related to the lifetime of the H-bond ?*

- The second question concerns the *strength* of the relaxation: it depends on the specific system and is related to the interaction potential between molecules. *How does the specific molecular arrangement affect the strength of the relaxation in HB liquids*

- The third question concerns the *activation energy* of the process: *is the activation energy of the structural relaxation related to the activation energy necessary to make and break H-bonds?*

One of the objectives of this thesis is therefore to asses the relevance of the hydrogen bond on the dynamics of associated liquids by using BLS and IXS methods. Another important point concerns the presence of the **microscopic relaxation** process. In simple monatomic liquids both kinetic and mode-coupling theories predict the existence of two distinct relaxation processes [2] and, this prediction has been demonstrated both by numerical simulations [3, 4] and by experiments [5]. In these theories, one of the two processes is the structural relaxation, and the other is the microscopic one both described in Chapter 3. The outlined scenario seems to point that the $\alpha-$ and $\mu-$ relaxation processes are universal features of the liquid state. In this context, however, no attempt has been made so far to include the important class of hydrogen bonded liquids. A question awaits clarification:

- *Are both the structural and microscopic relaxation process present also in hydrogen bonded liquid systems?*

With the aim to shed light on all these aspects concerning the high frequency dynamics of hydrogen bonded liquids, we will present in next chapter the IXS experimental study of HF and $(HF)_x(H_2O)_{1-x}$ solutions.

Chapitre 5

Ce chapitre est dédié à la description de tous les aspects expérimentaux liés à les mesures du facteur de structure dynamique $S(Q,\omega)$ de l'acide fluorhydrique (HF) et des solutions $(HF)_x(H_2O)_{1-x}$. A cause de la haute réactivité de ces systèmes, le développement du montage expérimental est d'une importance primordiale pour la réussite de l'expérience.
Le chapitre est organisé comme en suit :
Dans le Par. 5.2 nous discutons les principaux problèmes concernant l'laboration d'une cellule pour l'échantillon, et nous arrivons à la conclusion qu'une cellule spécifique est nécessaire pour chaque échantillon; puis nous décrivons en détail chaque partie de l'assemblage et la préparation de l'échantillon.
Dans le Par. 5.3 sont présentées les mesures de la résolution en nergie des cinq analyseurs. Ces résolutions seront convoluées avec les modèles théoriques dans le prochain chapitre afin de faire les ajustements des données expérimentales.
Dans le Par. 5.4 nous présentons les mesures de la cellule vide, c'est-à-dire la contribution à l'intensité totale diffusée due à la cellule: on verra que cette contribution peut tre négligée dans le cas de l'HF alors qu'elle doit tre prise en considération pour l'analyse des spectres des solutions $(HF)_x(H_2O)_{1-x}$.

Chapter 5

Sample environment and experimental set-up

5.1 Introduction

This chapter is devoted to the description of all the experimental aspects related to the measurements of the dynamic structure factor of pure hydrogen fluoride (HF) and $(HF)_x(H_2O)_{1-x}$ solutions. Due to the high reactivity of these two systems, in fact, the design and development of an appropriate experimental set-up is mandatory to succeed in the experiment. The chapter is organized as follow:
in **Sec. 5.2** we discuss the main problems concerning the design and development of a sample cell ending that a specific cell is necessary for each sample; then we describe in details each part of the assembly and the sample preparation.
In **Sec. 5.3** the measurements of the energy resolutions of the five analyzers are shown. This resolutions will be convoluted with the theoretical models in order to fit the experimental data, as we will see in next chapter.
In **Sec. 5.4** we report the "empty cell" measurements, namely, the contribution to the total scattered intensity due to the sample cells: we will see that this contribution can be neglected in the case of HF whereas it has to be taken into account for $(HF)_x(H_2O)_{1-x}$ analysis of the spectra.

5.2 Sample environment

We present here a specific apparatus developed to study the dynamic structure factor of hydrogen fluoride (HF) and $(HF)_x(H_2O)_{1-x}$ solutions by inelastic x-rays scattering. We

start discussing some aspects that have to be taken into account for the design and the construction of the cell.

- Choice of materials. Only fluoride containing plastic, like Teflon and stainless steel resist to the chemical reactivity of HF whereas the choice is limited to the Teflon in the case of $(HF)_x(H_2O)_{1-x}$. The behaviour of metals, alloys and plastics in presence of hydrogen fluoride and one $(HF)_x(H_2O)_{1-x}$ solution (x=0.35) is reported in Figure 5.1.

Metals and alloys	Alluminium and its alloys	Copper	Nickel	Monel	Inconel	Tantalum	Titanium	Tin	Zinc	Silver	Platinum	Gold
HF	D	C	A: T<100^{0}C	A	A	D	D	D	A	A	A	A

A Good resistance

B Fairly good resistance depending on service conditions

C Fairly good resistance in absence of oxygen

D Poor resistance

Plastics	LDPE	HDPE	PP	PMP	PVC	PC	PS	SAN	ABS	ACECRYLIQUE	PTFE	PFA	E-CTFE
Temperature ^{0}C	20 | 50	20 | 50	20 | 50	20 | 50	20 | 50	20 | 50	20 | 50	20 | 50	20 | 50	20 | 50	20 | 50	20 | 50	20 | 50
$(HF)_{0.35}(H_20)_{0.65}$	● ●	● ●	● ●	● ●	◐ ◐	○ ○	◐ ◐	◐ ◐	○ ○	◐ ◐	● ●	● ●	● ●
HF	A T<60^{0}C		A		C		A T<20^{0}C				A T<250^{0}C		

● Excellent resistance no corrosion

◐ Good resistance minor corrosion

◐ Limited resistance moderate corrosion

○ Minor resistance not recommended

Figure 5.1. Behaviour of metals, alloys and plastics in presence of hydrogen fluoride and one $(HF)_x(H_2O)_{1-x}$ solution (x=0.35).

- Choice of the windows for the passage of the incident and scattered x-rays beam. They have to be chosen in such a way as to minimize their contribution to the total scattering and to be resistant to the corrosion of HF and $(HF)_x(H_2O)_{1-x}$. In order to satisfy both these conditions we opted for sapphire windows (Al_2O_3) in the case of HF. Their measured contribution to the total scattered intensity is in fact negligible. Unfortunately this material cannot be used for $(HF)_x(H_2O)_{1-x}$ because it does not resist to the chemical etching of the solutions, we had therefore to resort to Teflon again.

- Sample length. This is the distance between the windows for the incoming and scattered beam of the cell. This length is established in order to have the better compromise between the attenuation of the signal due to the absorption of the sample and the scattering volume.

Because of what mentioned above two different cells based on similar schemes but developed with different materials and some structural variations have been made: one for pure HF and another for $(HF)_x(H_2O)_{1-x}$ solutions.

HF and $(HF)_x(H_2O)_{1-x}$ solutions physical properties

We resume here the main physical properties for HF and $(HF)_x(H_2O)_{1-x}$ solutions. In Figure 5.2 the melting point, the boiling point and the density of the $(HF)_x(H_2O)_{1-x}$ solutions are plotted as a function of concentration, while the same properties for the two limiting case, HF and H_2O are reported in Table 5.2

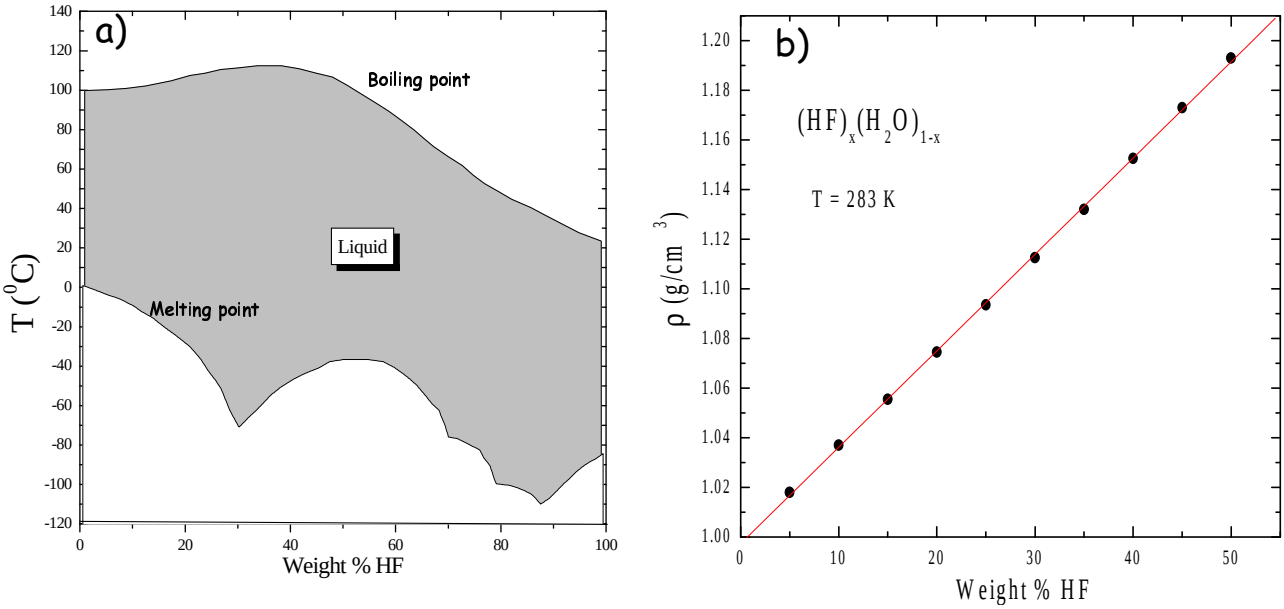

Figure 5.2. (a) Melting point, boiling point [44] and (b) density [45] for $(HF)_x(H_2O)_{1-x}$ solutions as a function of concentration.

	Molecular weight	ρ (g/cm^3) $(T = 273\ K)$	Melting point (K)	Boiling point (K)	$\gamma = c_p/c_v$ (T=273K)
HF	20	1.04	193	292	1.14
H_2O	18	1.002	273	373	1.006

HF sample cell

It is suited to study the sample in the liquid phase, namely in a temperature range between 19^0C and -80^0C.

In Figure. 5.3 the drawing of the cell is reported: the body has been realized in stainless steel; its length, $L = 1cm$, has been established considering the linear attenuation coefficient μ of liquid HF at 21748 eV and choosing $L = 1/\mu$ as discussed in Sec.1.3.1 Two sapphire windows of $250\mu m$ thickness and $6mm$ diameter, have been applied to allow the passage of the incident and scattered beam. They have been glued on a holder plate which has then been screwed to the body cell. An o-ring of parofluor has been applied between the holder and the cell to guarantee a good tightness of the windows. A stainless steel 316 angle valve at the entrance of the cell enables to feel the cell and to confine the sample.

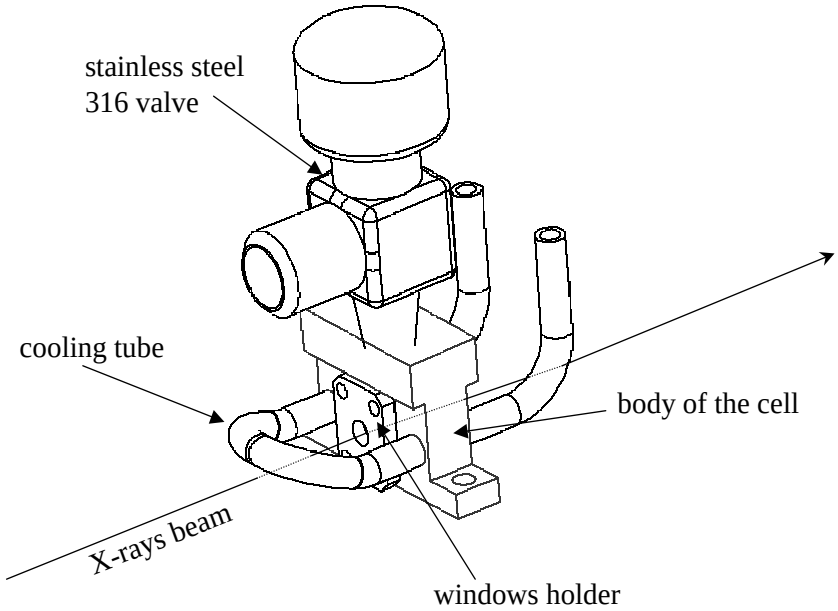

Figure 5.3. Sample cell used to measure the dynamic structure factor of hydrogen fluoride (HF) by inelastic x-ray scattering and Brillouin light scattering.

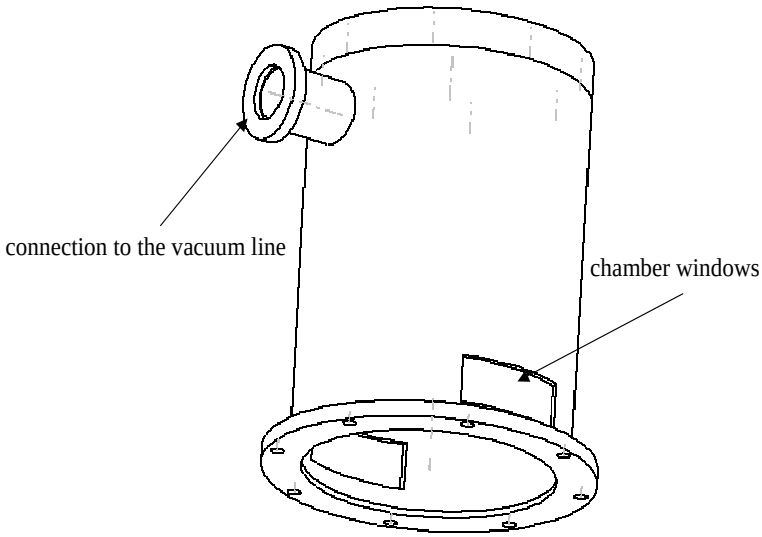

Figure 5.4. Stainless steel vacuum chamber to isolate the sample cell from the external environment [46].

Two stainless steel tubes, passing through the body of the cell, allow the passage of the refrigerator liquid used to cool down the sample. The cell has been fixed on a stainless steel flange (diameter 11.5 cm) (Figure 5.6) through an insulating Teflon plate to reduce thermal exchanges.

$(HF)_x$ $(H_2O)_{1-x}$ sample cell

This cell is very similar in shape to the one used for pure HF. $(HF)_x(H_2O)_{1-x}$ solutions are liquid at room temperature and this fact simplifies the operations related to the filling procedure avoiding the necessity of using any valve. The cell has been designed to study the sample at room pressure, at fixed temperature T= 283 K and in a momentum transfer range of $1 \div 15$ nm^{-1}. In Figure 5.5 the drawing of the cell is reported. The main body is done in copper it has two apertures: the first, on the top, of cylindrical shape with a diameter of $\approx 1cm$ embodies the sample container; the second, on the lateral walls, is necessary to allow the x-rays beam to pass through the sample, its width is calculated so as to avoid cuts to the scattered beam at the analyzed angles. The sample container is a cylinder in Teflon with a diameter of $\approx 1cm$, length comparable to the x-rays photo-absorption of $(HF)_x(H_2O)_{1-x}$ solutions at $E \approx 21KeV$. In this case the windows are the walls of the cell themselves. For this reason they have been chosen as thin as possible (

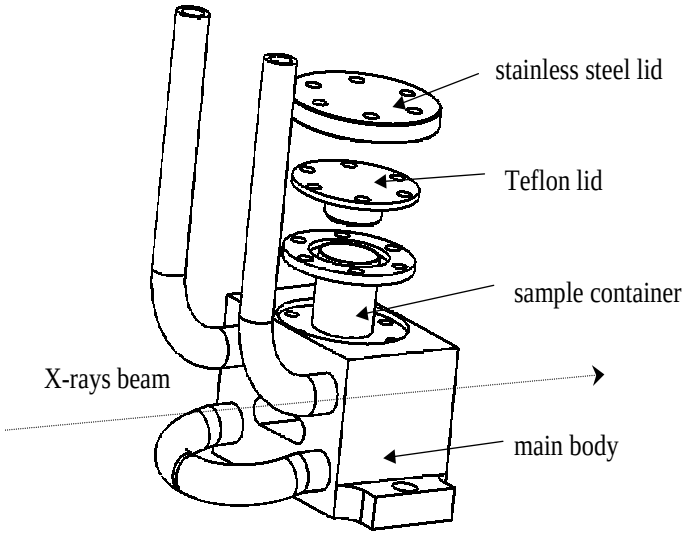

Figure 5.5. Sample cell used to study the dynamic structure factor of $(HF)_x(H_2O)_{1-x}$ solutions by inelastic x-ray scattering.

0.5 mm thick) to reduce the absorption of the incoming and scattered radiation and to decrease the scattering contribution due to the Teflon. In the upper part of the cylinder, a groove for the o-ring in parofluor is present, it guarantees the tight when the lid in Teflon is screw closing the container. To better fix the screws, a second lid in stainless steel has been used since the softness of Teflon does not allow to shut tightly without breaking the cell. The tubes in copper, which pass through the body of the cell, are used to allow the cooling liquid to pass and to thermalize with the sample. The temperature is read by means of a TYPE K thermocouple. The rest of the assembly, chamber, cooling system and L-shape holder, is the same for HF and $(HF)_x(H_2O)_{1-x}$ solutions.

Chamber

A stainless steel chamber (Figure 5.4) of the same diameter of the flange has been applied to isolate the cell from the external environment. It is connected to a vacuum line to better cool down the sample, to avoid the scattering of the air surrounding the cell and to reduce the risk of contamination of the environment in case of leaks. Two kapton windows, 100 μm thick, glued on the chamber, allow the passage of the beam. Their width is such that the radiation scattered by the sample does not suffer any cut at the higher scattering angle investigated.

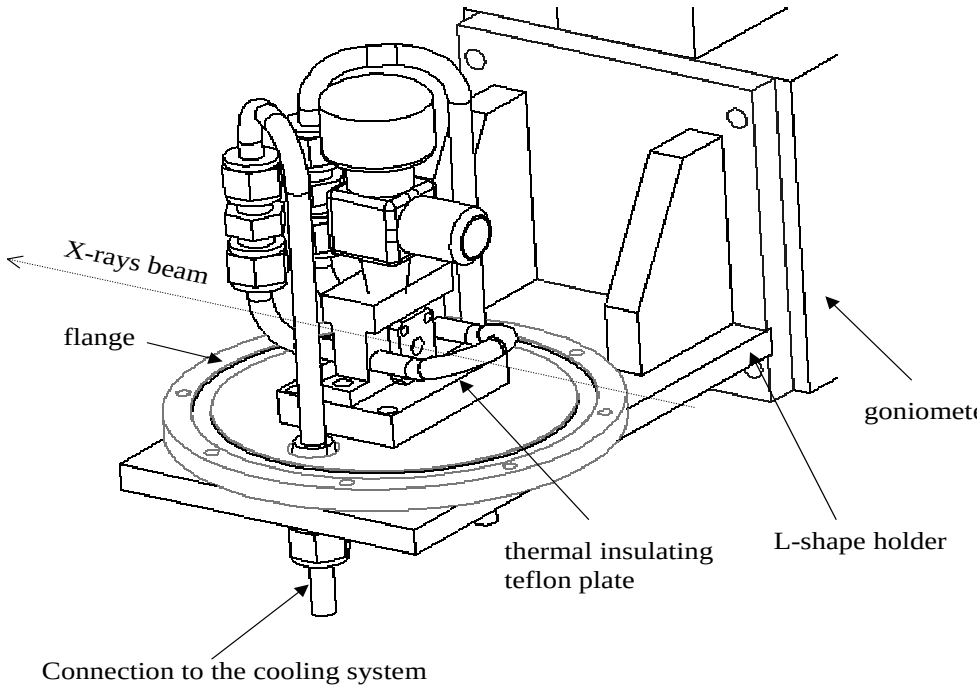

Figure 5.6. Sample set-up mounted on the goniometer of the sample stage of the beam-line ID16.

Cell plus chamber have been screwed on an L-shape holder (Figure 5.6) adapted to the sample stage goniometer of the spectrometer which is used to align the cell with respect to the beam.

All the drawings concerning the HF and $(HF)_x(H_2O)_{1-x}$ solutions sample cells are reported in Appendix1 and Appendix2.

Cooling system

To cool down the sample a liquid flux cryostat DC50-K75 Haake has been used. The bath was filled with methanol, liquid recommended in the temperature range $-75^0 \div -10^0 C$. Thanks to some tricks we reduced the thermal dispersion improving the performances of the cooling system: the section and the length of the tubes connecting the bath with the cell has been chosen as small as possible to decrease the exchange surface with the air; the tubes have been wrapped with a protective layer of thermal insulating poliuretan; the vacuum level in the chamber has been pushed up to $\approx 1 \cdot 10^{-6} mbar$. All this enabled to

reach a minimum sample temperature of -60^0C.

Filling apparatus

The line to fill the cell was composed of a Teflon tube connecting directly the main body of the sample cell to the HF bottle (pure gas 99.9% from Air Products). On this tube three valves were present: the first between the experimental set-up and the external nitrogen line, the second connected to the vacuum pump and the third linked to the safety absorption cartridge (soda-lime). The tightness of the cell and of each part of the filling line was successfully tested by doing a detailed leak check with a helium detector. In order to avoid any the contamination of the sample with air and water, the cell was evacuated before the filling.

$(HF)_x$ $(H_2O)_{1-x}$ preparation

We analysed four different mixtures of water and hydrogen fluoride $(HF)_x(H_2O)_{1-x}$ with x = 0, 0.2, 0.4, 0.73. The samples were prepared starting from solutions of hydrogen fluoride, 40% and 73% nominal value, from Fluka. To verify the accuracy of these values we did volumetric measurements using flasks in Teflon with a volume of 25 ml and 50 ml and a precision balance ($\pm 1mg$). We proceeded in the following way:

- we weighted the empty flask of 50 ml,
- we filled the flask with 50 ml of hydrogen fluoride 40% and weighted the flask+solution,
- we calculated the weight of the solution by simple subtraction (flask+solution-flask)
- we calculated the density ρ of the solution by dividing its weight by the volume(50 ml) of the flask.
- we compared the obtained value of ρ with the one of Figure 5.2 (b) [45] which allows to extract the right concentration.

We applied the described procedure to verify the face values of the 40% 73% solutions, while we prepared the 20% by diluting with demineralised water the mixture hydrogen fluoride 40%.

5.3 Experimental resolutions

The $S(Q,\omega)$ of HF has been studied as a function of the wave vector Q by rotating the 6.5 m horizontal arm on which the five independent analyzers (described in chapter 2) are held one next to each other with a constant angular offset. This imply that each spectrum is affected by the resolution of the corresponding analyzer with whom it has been acquired (Figure 5.7). The spectra have been collected using the Si(11,11,11) configuration which corresponds to an incident beam of E = 21748 eV energy and to a resolution of $\approx$ 1.5 meV. The resolution of each analyzer, has been measured by using a sample of PMMA (plexiglass) with a thickness of 5 mm and rotating the horizontal arm in such a way as to be, with the considered analyser, at $Q \approx 10nm^{-1}$ i.e. the maximum of the

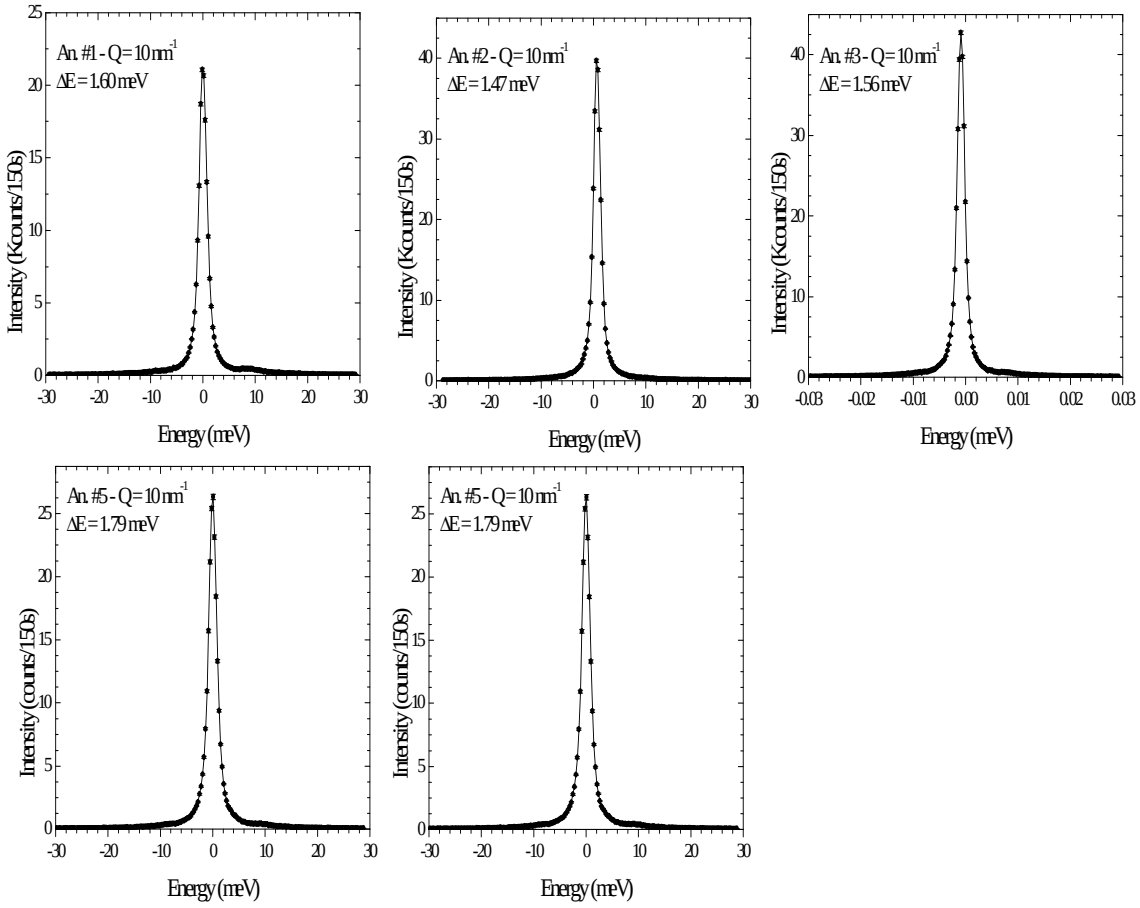

Figure 5.7. Energy resolution of the five analyzers

structure factor S(Q) of the PMMA. In this way the elastic contribution is dominant compared to the inelastic one and the effective size source introduces a small geometric contribution to the energy resolution.

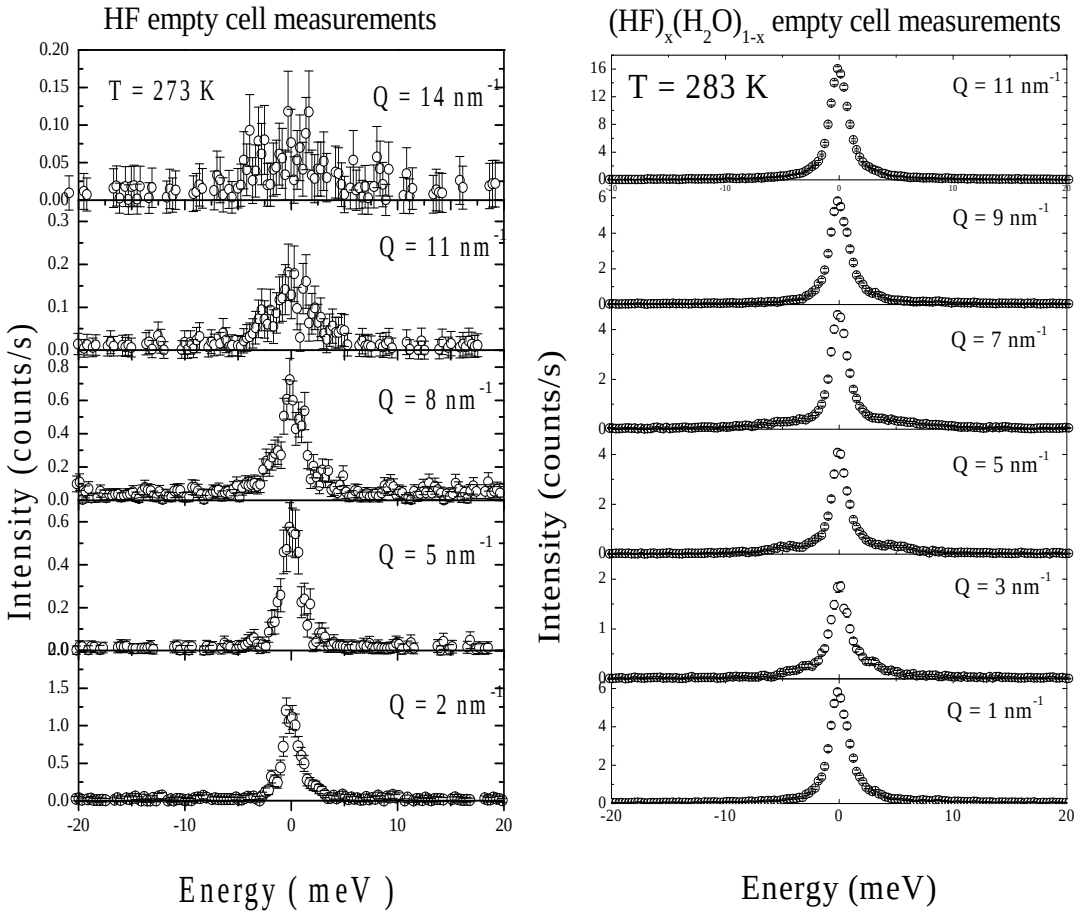

Figure 5.8. A sample of the empty cell measurements at the indicated Q value and temperature for the two different sample cells used in the experiment.

5.4 Empty cell measurements

We report in this section the empty cell scans at selected Q for the two different cells previously described. In Figure 5.8 the intensity scattered by the empty cell used for HF is shown. This contribution is due to the two sapphire windows of total thickness is 0.5 mm. As we will see in the next section, this intensity is negligible compared to the signal

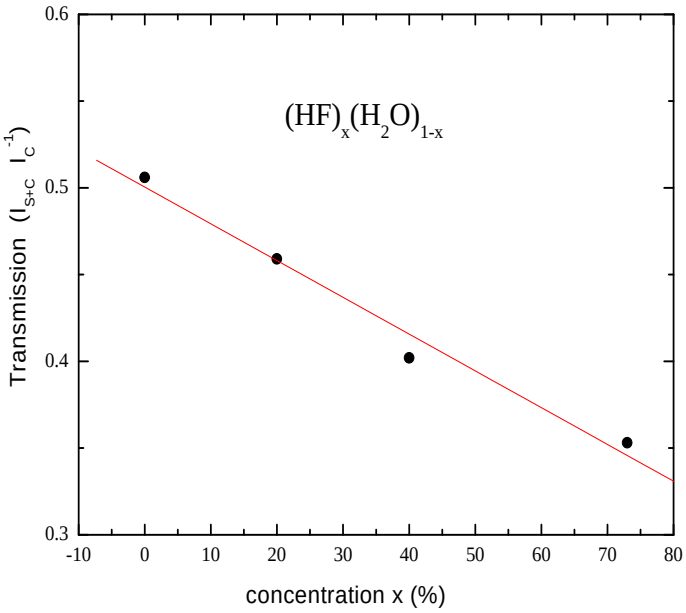

Figure 5.9. Ratio I_{S+C}/I_C for $(HF)_x(H_2O)_{1-x}$ as a function of concentration. I_{S+C} is the intensity transmitted by the cell filled with the sample and I_C is the intensity transmitted by the empty cell.

scattered by the sample. The transmission of HF has also been measured $I_{S+C}/I_C = 0.45$ where I_{S+C} is the intensity transmitted by the cell filled with the sample and I_C is the intensity transmitted by the empty cell. Similar measurements are reported in Figure 5.8 for the empty cell used for $(HF)_x(H_2O)_{1-x}$ solutions at some selected Q values and at T = 283 K. At difference with sapphire, this contribution, due to 1 mm of Teflon, cannot be neglected with respect to the signal scattered by the sample. In order to take it into account we measured the ratio I_{S+C}/I_C for each solution and we exploited it to subtract the empty cell contribution to the total scattered intensity. In Figure 5.9 the values of this ratio have been reported as a function of concentration.

Chapitre 6

Dans ce chapitre nous présentons les résultats expérimentaux obtenus en étudiant le facteur de structure dynamique $S(Q,\omega)$ de deux systèmes à liaison hydrogène, sujet de ce travail de thèse : l'acide fluorhydrique (HF) et les solutions $(HF)_x(H_2O)_{1-x}$. La dynamique collective de l'HF a été étudiée avec deux techniques différentes: la diffusion Brillouin de la lumière (BLS) et la diffusion inélastique des rayons X (IXS), pour caractériser la transition du régime hydrodynamique et macroscopique sondé par BLS au régime mesoscopique exploré par IXS. Afin d'éclaircir le comportement dynamique des liquides associés, nous avons comparé nos résultats avec ceux de l'eau. Ensuite, puisque la principale différence entre l'acide fluorhydrique et l'eau concerne la nature des agrégats à liaison hydrogène, nous avons exploré la dynamique des solutions $(HF)_x(H_2O)_{1-x}$ par IXS afin de décrire le passage du comportement dynamique d'un liquide à l'autre. Nous essayons de donner une réponse à toutes les principales questions présentées dans le Chapitre 4 concernant les phénomènes de relaxation dans les liquides à liaison hydrogène. Le chapitre est organisé comme de suit:

le Par. 6.2 est dédié à la présentation des mesures BLS sur l'HF. Les donnée sont analysées avec le model DHO décrit dans le Chapitre 3, pour obtenir la vélocité adiabatique du son et la viscosité cinétique longitudinale de l'HF à partir de la position et la largeur des pics inélastiques.

Dans le Par 6.3 nous présentons les expériences sur l'HF faites avec IXS. Les courbes de dispersions à différentes températures sont obtenues a partir de l'analyse DHO et sont comparées avec les résultats hydrodynamiques BLS. La transition de la vélocité du son c(Q) de la valeur adiabatique (obtenu avec BLS) à la valeur aux hautes fréquences, souligne la présence d' un processus de relaxation actif. Une étude plus approfondie avec le

modèle viscoélastique, présenté dans le Chapitre 3, permet de caractériser cette relaxation avec le temps de relaxation et l'intensité du processus ainsi que de démontrer son origine structurelle. Une comparaison avec des simulations de dynamique moléculaire donne les informations nécessaires pour discuter nos résultats expérimentaux en termes de deux processus de relaxation. Finalement nous résumons et discutons les principaux résultats sur l'HF.

Dans le Par. 6.4 les mesures IXS sur les solutions $(HF)_x(H2O)_{1-x}$ *sont présentées en fonction de la concentration à température fixée. Les courbes de dispersion sont également présentées. Comme dans le cas de l'HF une analyse viscoélastique des données confirme la présence du processus de relaxation structurale aux hautes concentrations de HF.*

Chapter 6

Study of the collective dynamics in HF and $(HF)_x$ $(H_2O)_{1-x}$ solutions

6.1 Introduction

In the following chapter we present the experimental results obtained by measuring the dynamic structure factor $S(Q,\omega)$ of the two hydrogen bonded (HB) liquid systems considered in this thesis work: hydrogen fluoride (HF) and $(HF)_x(H_2O)_{1-x}$ solutions. The collective dynamics of HF is investigated with two different techniques: Brillouin light scattering (BLS) and inelastic X-rays scattering (IXS) to characterize the transition from the hydrodynamic macroscopic regime (BLS), to the mesoscopic regime (IXS). Aiming to shed light on the behaviour of the collective dynamics of high associated liquids, we compare these results with those existing on water. Then, since the main difference between HF and H_2O lies in the different HB arrangement and properties, the collective dynamics of $(HF)_x(H_2O)_{1-x}$ solutions is investigated by IXS with the aim to describe the passage from the behaviour of one liquid to the other. We try to provide an answer to the main open questions presented in Chapter 4 concerning the relaxation phenomena in HB liquids.

The chapter is organized as follow:

Sec. 6.2 is devoted to the presentation of the BLS measurements on HF. The data are analysed in term of the DHO model in order to extract the adiabatic sound velocity and the kinematic longitudinal viscosity of HF from the position and the width of the inelastic peaks respectively.

In **Sec. 6.3** we present the IXS experiments on HF. The dispersion curves at different temperatures are derived from a DHO analysis and compared with the hydrodynamic BLS results. The transition of the sound velocity $c(Q)$ from the adiabatic value (obtained with BLS) to the high frequency limit, highlights the presence of an active relaxation process. A more refined study in terms of the viscoelastic model, allows to characterize this relaxation by extracting relaxation time and strength of the process and to demonstrate its structural origin. A comparison with existing molecular dynamic simulations provides the necessary information to discuss the experimental results in the framework of a two relaxation processes scenario. We finally summarize and discuss the main results on HF. In **Sec. 6.4** the IXS measurements on $(HF)_x(H_2O)_{1-x}$ solutions are reported as a function of concentration at fixed temperature. The dispersion curves determined with the DHO model are presented. As in the case of HF a viscoelastic analysis of the data confirms the presence of the structural relaxation at higher concentrations of HF. A scaling mass model is proposed which allows to give an estimation of the sound velocity at different concentrations of HF.

6.2 Study of the dynamic structure factor of HF by Brillouin light scattering

The dynamic structure factor of HF in the **hydrodynamic regime** has been studied by *Brillouin* light scattering using a Sandercock-type multi-pass tandem Fabry-Perot interferometer in Perugia (Italy) characterized by high **contrast** ($> 5 \cdot 10^{10}$), **resolution** (FWHM $\approx$ 0.1 GHz) and a **finesse** of about 100. The wavelength of the incident radiation was $\lambda = 514.5nm$ and the light scattered by the sample was collected in the back-scattering geometry ($\theta = 180^0$). The **free spectral range** (FSR) was set to 10 GHz, the integration time was approximately 2.5 $s/channel$. The polarization of the incident light was vertical while the light scattered by the sample was collected in the unpolarized configuration. The aim of the present measurement is to determine the energy position of the Brillouin doublets due to the propagation of sound modes and their width. From this two experimental observations, it is possible to extract information about the *adiabatic sound velocity* $\mathbf{c_s}$ and the *longitudinal kinematic viscosity* $\nu_\mathbf{L}$.

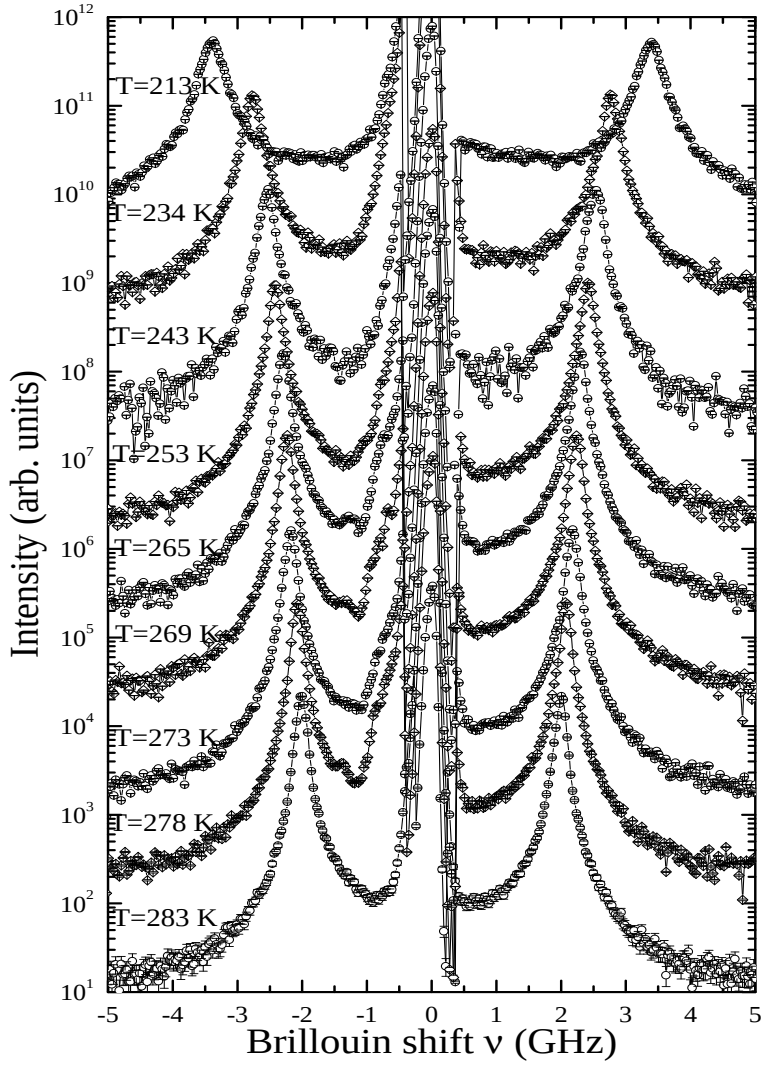

Figure 6.1. Unpolarized Brillouin light scattering spectra at the indicated temperatures in logarithmic scale. They are shifted on the y-axis one respect to the other.

6.2.1 Experimental data

Brillouin spectra have been collected in the $213 - 283\ K$ temperature range, being $T_B = 292\ K$ the boiling point of HF and $T_M = 193\ K$ its melting point. We used the sample cell and conditions as previously described in Chapter 5. The collected unpolarized spectra are shown in Figure 6.1 in logarithmic scale. The central part represents the cut of the pinhole used to avoid that the spectra are affected by elastic stray light coming from spurious reflections. In Figure 6.2 we report a selection of the measured spectra in linear

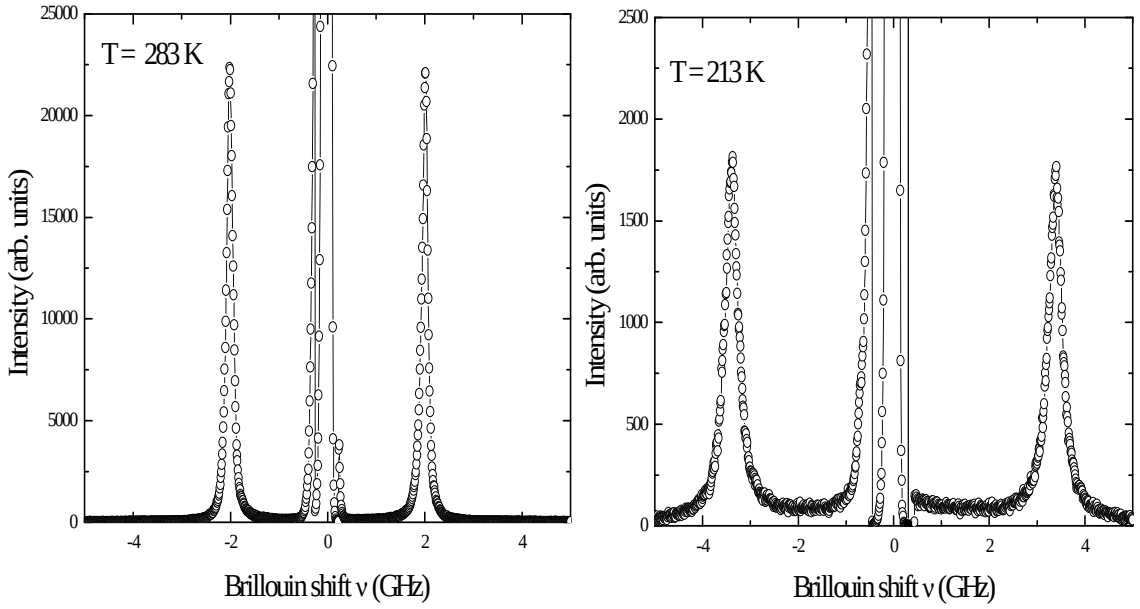

Figure 6.2. Unpolarized Brillouin light scattering spectra in linear scale at the lowest and highest investigated temperature .

scale, at the lowest (T = 213 K) and highest (T = 283 K) investigated temperatures. The spectrum at T = 213K, shows a prominent background between the central unshifted component and the Brillouin peaks, it extends symmetrically on either side of the central component to the Brillouin doublets.

This is the *Mountain* contribution [30], a quite broad background compared to the central line that becomes increasingly broad at decreasing temperatures, where it starts to affect the shape of the inelastic peaks. We do not take into account this contribution in the analysis of the spectra presented in the following.

6.2.2 Data reduction: adiabatic sound velocity and kinematic longitudinal viscosity

The quantities of interest are the width and the position of the Brillouin peaks because they are directly related to the sound velocity c_s and to the kinematic longitudinal viscosity ν_L of HF. To this purpose the experimental data have been fitted in a limited region around the inelastic peaks with a fitting function obtained by the convolution of the instrumental resolution $R(\omega)$ with the damped harmonic oscillator (DHO) described in Chapter 3.

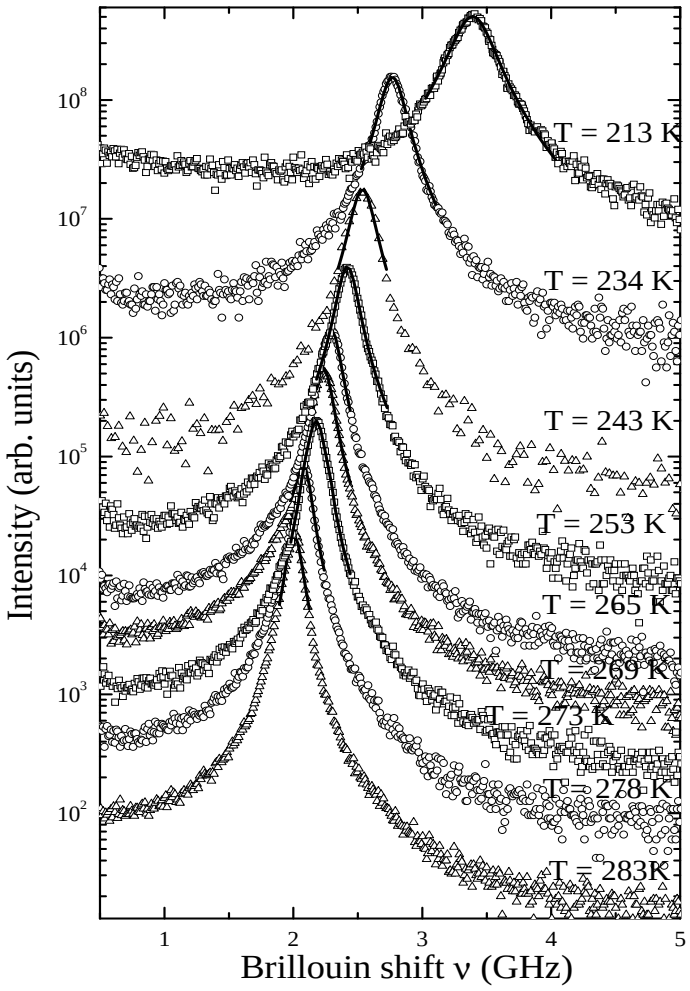

Figure 6.3. Stokes part of the unpolarized Brillouin light scattering spectra of HF in logarithmic scale at the indicated temperatures. The data (open symbols) are superimposed to the fit (solid line) .

$$I(\omega) = R(\omega) \otimes A \frac{2\Gamma\Omega^2}{(\Omega^2 - \omega^2)^2 + (2\omega\Gamma)^2} \tag{6.1}$$

The curves resulting from the fitting procedure are reported in Figure. 6.3 superimposed to the data. The two relevant independent parameters are $\Omega = 2\pi\nu_0$ and 2Γ, namely, the position and the full width half maximum (FWHM) of the longitudinal-acoustic modes. By exploiting the relations $\Omega = c_s Q$ and $\nu_L = 2\Gamma/2\pi$, the adiabatic sound velocity c_s and the kinematic longitudinal viscosity ν_L are obtained. To this purpose it is necessary to

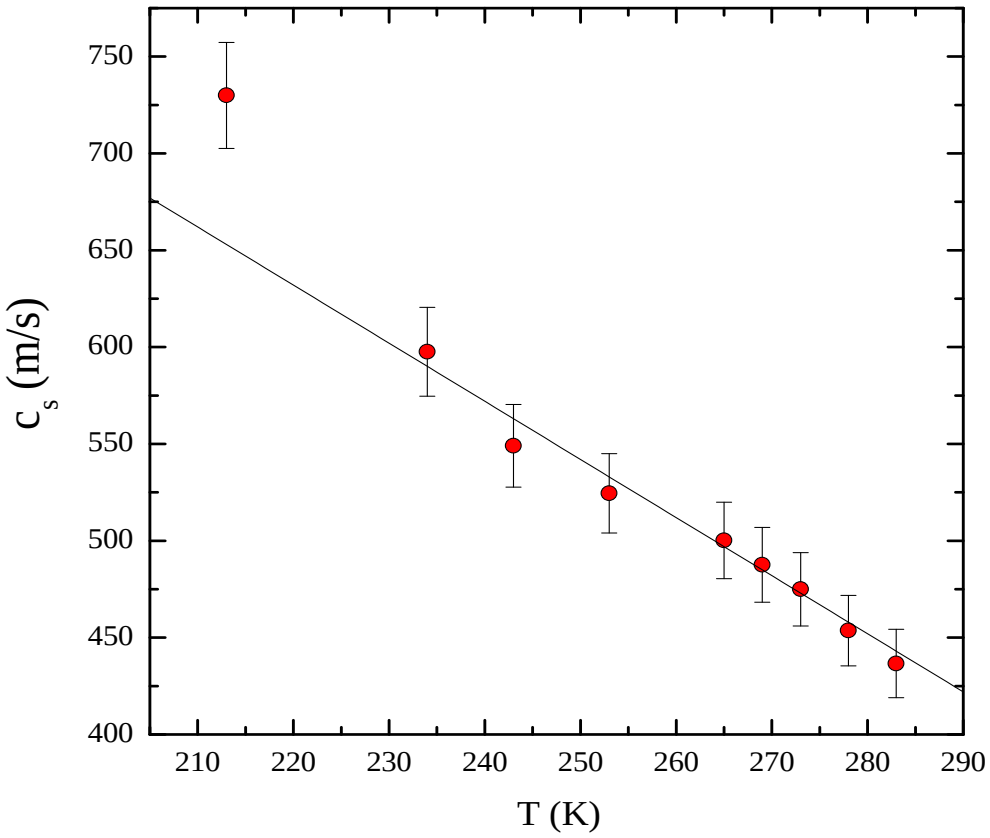

Figure 6.4. Sound velocity values from Table 6.1 as calculated from the position of the Brillouin light scattering peak in backscattering geometry ($\theta = 180^0$) (full circles). The linear fit has been done excluding the point at lower temperature as discussed in the text.

know Q:

$$Q = \frac{4\pi n}{\lambda} sin(\frac{\theta}{2}) \tag{6.2}$$

where n is the refractive index and $\theta = 180^0$ represents the scattering geometry. The temperature dependence of the refractive index $n(T)$ has been obtained by exploiting the Clausius-Mossotti relation:

$$\frac{n(T)^2 - 1}{n(T)^2 + 2} = \frac{4}{3}\pi\rho(T)\alpha \tag{6.3}$$

where α is the optical polarizability and ρ the density of HF. By using the values of $n(T \approx 293K)$ [47] and $\rho(T \approx 293K)$ [45] we calculated a temperature independent value

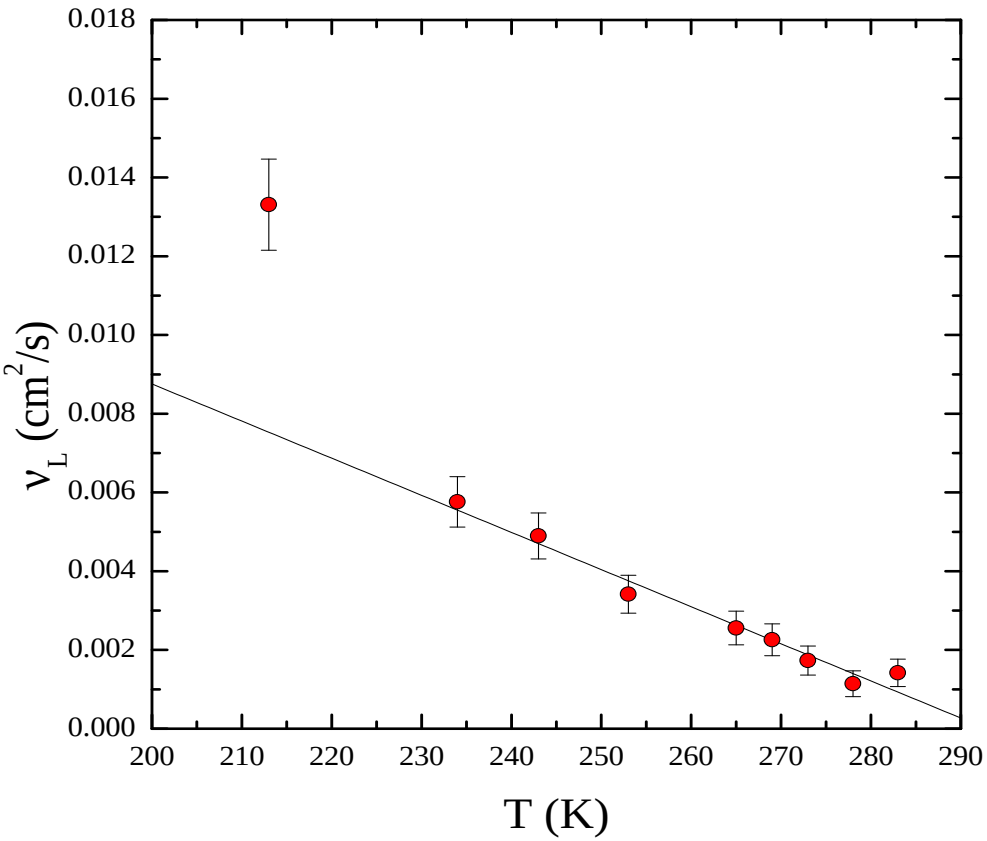

Figure 6.5. Kinematic longitudinal viscosity obtained from the width of the Brillouin peak according to the DHO model (full circles). The linear fit has been obtained excluding the point at T=213 K as discussed in the text.

of α. The data for $n(T)$ have been extrapolated for each temperature by using the same relation once known the temperature dependence of $\rho(T)$. Its expression obtained from the literature [45] is given by:

$$\rho(T) = -0.002 \cdot T + 1.616 \tag{6.4}$$

with ρ in g/cm^3 and T in K. The calculated values of the sound velocity c_s and the kinematic longitudinal viscosity ν_L are shown in Figure 6.4 and Figure 6.5 respectively. As previously discussed, the fit function used is a simple DHO convoluted with the instrumental resolution. No further contributions have been included to take into account the Mountain mode which affects clearly the shape of the Brillouin peak at the lowest temperature (T = 213 K). For this reason the point at $T = 213K$ has been excluded in

T (K)	ν_0 (GHz)	$2\Gamma/2\pi$ (GHz)	$Q(nm^{-1})$	c_s (m/s)	ν_L cm^2/s
213	3.37	0.56	0.029	730	0.0133
234	2.74	0.24	0.029	600	0.0058
243	2.51	0.20	0.029	550	0.0049
253	2.39	0.14	0.029	530	0.0034
265	2.27	0.10	0.029	500	0.0026
269	2.21	0.09	0.028	490	0.0023
273	2.15	0.07	0.028	480	0.0017
278	2.05	0.05	0.028	450	0.0011
283	1.97	0.06	0.028	440	0.0014

Table 6.1. Values of the frequency position ν_0 and of the width 2Γ of the Brillouin peaks as obtained by the fit with the function 6.1. Q values from the expression 6.2 are also reported together with the calculated sound velocity c_s and kinematic longitudinal viscosity ν_L.

the linear fits of Figure 6.4 and 6.5. The $c_s(T)$ follows a linear behaviour characterized by a temperature dependence well represented by the equation:

$$c_s(T) = -3 \cdot T + 1290 \tag{6.5}$$

where c_s is in m/s and T in K. The same as been done for the kinematic longitudinal viscosity ν_L for which the linear fit provides a temperature behaviour described by the relation:

$$\nu_L(T) = -0.0943 \cdot 10^{-3} \cdot T + 0.0276 \tag{6.6}$$

where $\nu_L(T)$ is in cm^2/s and T in K. All the values of Q, of the fit parameters and of the calculated ν_L and c_s, are reported in Table 6.1.

6.3 Study of the high frequency collective dynamics of HF by inelastic x-ray scattering

In this section we report the IXS measurements done to probe the dynamics of HF in the **mesoscopic regime**. We compare these data with the BLS results to characterize

the transition from the hydrodynamic regime to the mesoscopic and with existing MD simulations on liquid hydrogen fluoride (HF).

6.3.1 Experimental data as a function of Q and T

The $S(Q,\omega)$ has been studied at four temperatures in the range 214-283 K and exactly at T = 283 K, T = 254 K, T = 239 K and T = 214 K as a function of the wave vector in the ranges $2 \div 31nm^{-1}$ for the spectra at T = 239 K and $1 \div 15nm^{-1}$ for the spectra at the other temperatures. Each scan took 180 min and each spectrum at fixed Q was obtained by summing up to 6 scans. We used the experimental set-up described in Chapter 5.
We report in Figure 6.6 a sample of the measured spectra at the investigated temperature and at increasing momentum transfer, they are compared with the instrumental resolution. The peak centered around zero energy transfer shows a strong Q dependence, becoming increasingly broader with increasing Q and narrower in the region where one also finds the first sharp diffraction peak (FSDP) in the static structure factor (de Gennes narrowing [48]), the characteristic asymmetry is due to the detailed balance.

6.3.2 DHO analysis

A first raw analysis of the spectra has been done in terms of the damped harmonic oscillator (DHO) model [49]. As described in Chapter 3, in the memory function approach, this model is obtained from a Markovian approximation and implies a δ function for the central line in the energy domain. To take into account a finite width for the quasi-elastic central peak of our spectra, we used a Lorentzian.
The resulting fitting function is composed by a DHO for the inelastic signal, a Lorentzian for the central peak and a non constant background $B(\omega) = A + B\omega$:

$$S(Q,\omega) = P_c(Q)\frac{\Gamma_c(Q)}{\omega^2 + \Gamma_c^2(Q)} + P_l(Q)\frac{\Gamma_l(Q)\Omega^2(Q)}{(\omega^2 - \Omega^2(Q))^2 + (\omega\Gamma_l(Q))^2} + B(\omega) \qquad (6.7)$$

where $\pi P_c(Q)$ and $\pi P_l(Q)$ are the areas of the elastic and inelastic contribution respectively, $\Gamma_c(Q)$ is the FWHM of the central line, $\Gamma_l(Q)$ is the inelastic damping, $\Omega(Q)$ is the propagation frequency of the collective modes.
The detailed balance has been taken into account during the fitting procedure by multiplying the classical $S(Q,\omega)$ by $\hbar\omega\beta/(1-e^{\hbar\omega\beta})$ as discussed in section 3.2. The final fitting

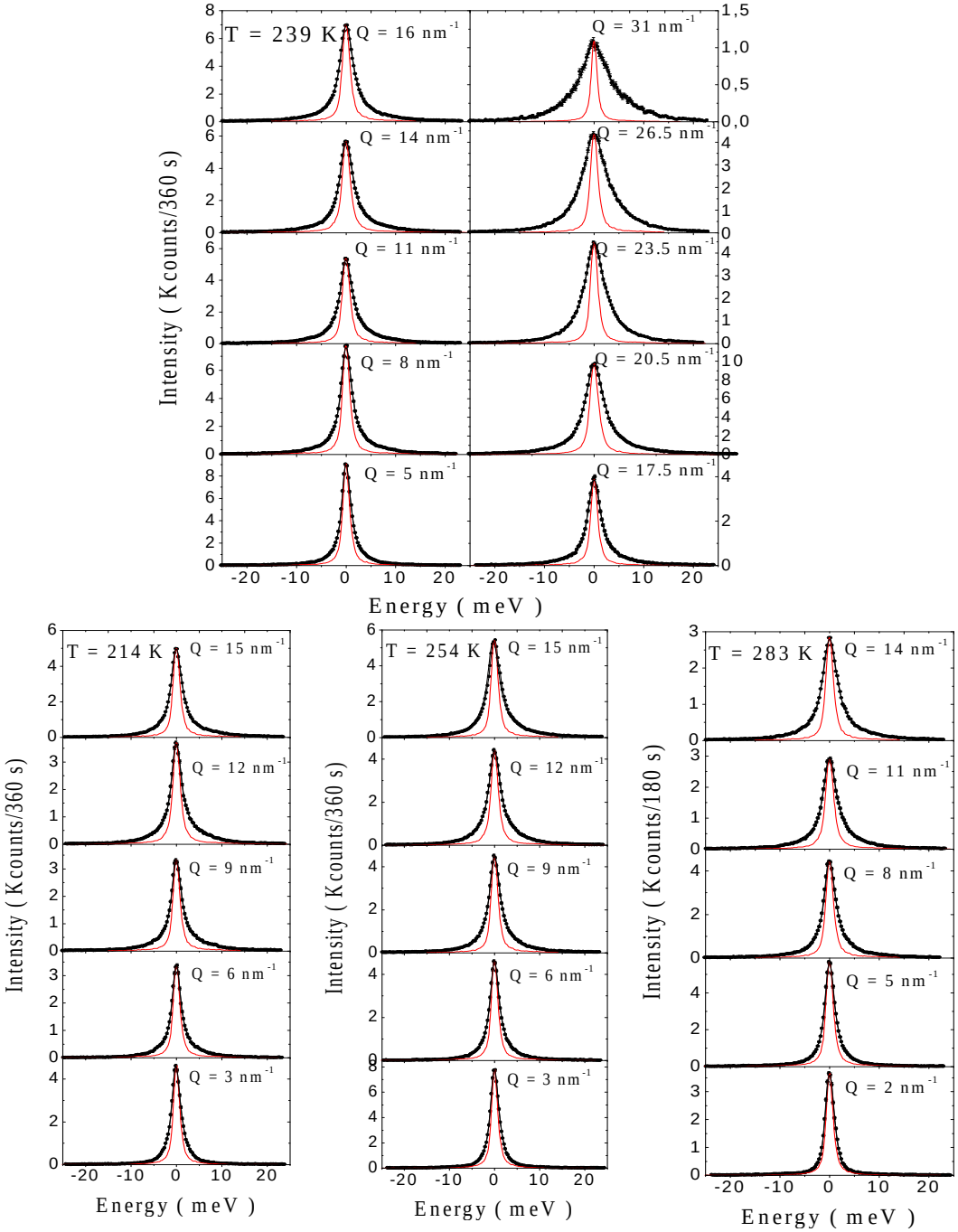

Figure 6.6. *a*) IXS spectra of HF at fixed temperatures $T = 214\ K, 239\ K, 254\ K, 283\ K$ and at some selected Q. The raw data (lines + symbol) are plotted together with the corresponding experimental resolutions (dashed lines).

function was obtained by convolution with the instrumental resolution $R(\omega)$:

$$I(Q,\omega) = R(\omega) \otimes \frac{\hbar\omega\beta}{1-e^{\hbar\omega\beta}} S(Q,\omega) \tag{6.8}$$

where $\beta = K_B T$. An example of the fit, done using a standard χ^2 minimization routine, is reported in Figure 6.7(a) at T = 239 K in the low Q region ($1 \div 7 nm^{-1}$). The de-convoluted inelastic part of the current spectra, $\omega^2/Q^2 S_i(Q,\omega)$ -whose maxima correspond to the parameter $\Omega(Q)$- is also plotted in Figure 6.7(b). The parameter we are interested in is $\Omega(Q)$, which corresponds to the frequency of the sound modes. The dispersion curve $\Omega(Q)$ vs. Q is shown in Figure 6.9 for the low Q region data at the four analysed temperatures. For Q between 4-5 and 7 nm^{-1}, they show a linear dependence with a slope corresponding to sound speed values substantially higher than the adiabatic sound speeds c_o measured

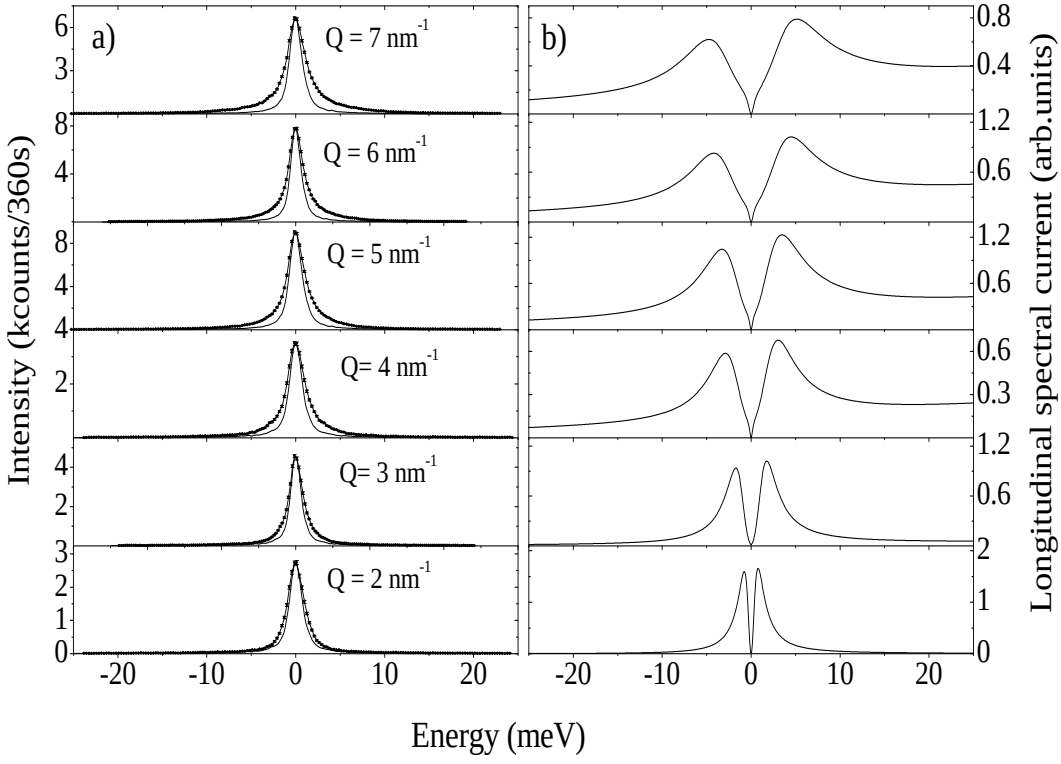

Figure 6.7. *a*) IXS spectra of HF at fixed temperature $T = 239K$ and at the indicated moment transfer Q plotted together with the corresponding experimental resolutions (solid lines). *b*) Resolution de-convoluted inelastic part (DHO) of the longitudinal spectral current.

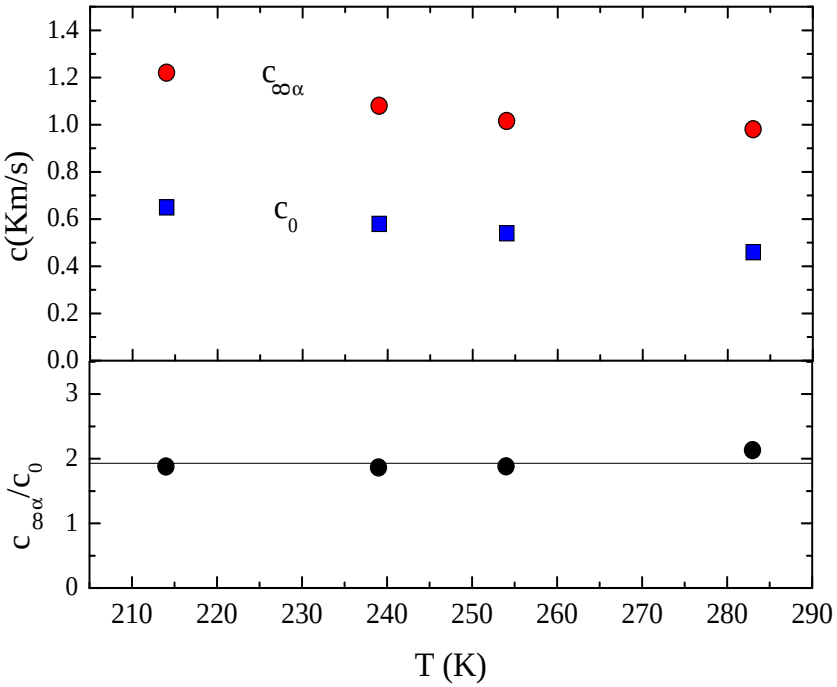

Figure 6.8. (a) Behaviour of the sound velocity in HF as a function of the temperature : c_0 (full squares), $c_{\infty\alpha}$ (full circles). (b) Sound velocities ratio $c_{\infty\alpha}/c_0$.

with the BLS technique (Section 6.2).

Moreover, in the 2 to 4 nm^{-1}, the IXS data are compatible with a transition of $c(Q)$ from its low frequency value c_o to the higher value. This increase of $c(Q)$ is then interpreted as due to the $\alpha-$relaxation discussed in Section 3.5.3, and it comes out to be quite similar to that of water previously shown in Figure 4.2. As in the case of water, also here, in fact, the ratio $c_{\infty\alpha}/c_o$ is close to two. In Table 6.2 an Figure 6.8, the values of c_0, $c_{\infty\alpha}$, and $c_{\infty\alpha}/c_o$ at the four investigated temperatures are reported.

T (K)	c_0 (m/s)	$c_{\infty\alpha}$ (m/s)	$c_{\infty\alpha}/c_o$
214	650	1220	1.9
239	600	1080	1.9
254	530	1010	1.9
283	460	980	2.2

Table 6.2. Values of the adiabatic sound velocity c_0 as measured with BLS technique (Section 6.2) for HF at the four investigated temperatures. It is compared with the high frequency limit $c_{\infty\alpha}$ obtained with IXS. The values of the ratio $c_{\infty\alpha}/c_o$ are also reported.

6.3.3 Viscoelastic analysis

A more formal procedure to describe the effect of a relaxation process in the $S(Q,\omega)$ is based on the viscoelastic model. As described in Section 3.5.5, in this approach the $S(Q,\omega)$ is expressed as:

$$S(Q,\omega) = I(Q)\frac{\omega_0(Q)^2 M'(Q,\omega)}{[\omega^2 - \omega_0(Q)^2 - \omega M''(Q,\omega)]^2 + [\omega M'(Q,\omega)]^2} \tag{6.9}$$

where $\omega_0(Q)^2 = (K_B T/mS(Q))Q^2$ is the normalized second frequency moment of $S(Q,\omega)$, K_B is the Boltzmann constant, m is the mass of the molecule and $M'(Q,\omega)$, $M''(Q,\omega)$ are respectively the real and the imaginary part of the Laplace transform of the memory function $M(Q,t)$. As discussed previously, we model $M(Q,t)$ by the sum of an exponential decay contribution and a δ-function :

$$M(Q,t) = \Delta_\alpha^2(Q)e^{-t/\tau_\alpha(Q)} + \Gamma_\mu(Q)\delta(t) \tag{6.10}$$

where $\Delta_\alpha^2(Q) = [c_{\infty\alpha}(Q)^2 - c_0(Q)^2]Q^2$, is the strength of the α process and $\Gamma_\mu(Q) = \Delta_\mu^2\tau_\mu(Q)$. As, similarly to water in fact, one expects that the microscopic relaxation process or μ-process, described in Section 3.5.3 is very fast with respect to the investigated timescale [1]. The experimental data were fitted to the convolution of the experimental resolution function with the dynamic structure factor model given by Eq. 3.36.
The relevant independent parameters are $c_{\infty\alpha}(Q)$, $c_o(Q)$, $\tau_\alpha(Q)$ and $\Gamma_\mu(Q)$. In Figure 6.10 we show the values obtained for $c_{\infty\alpha}(Q)$ and $c_0(Q)$, together with those for $c(Q)$ as deduced from the data of Figure 6.9 applying the relation $c(Q) = \Omega(Q)/Q$. We observe that the positive dispersion found for $c(Q)$ by the DHO analysis takes place between the values of

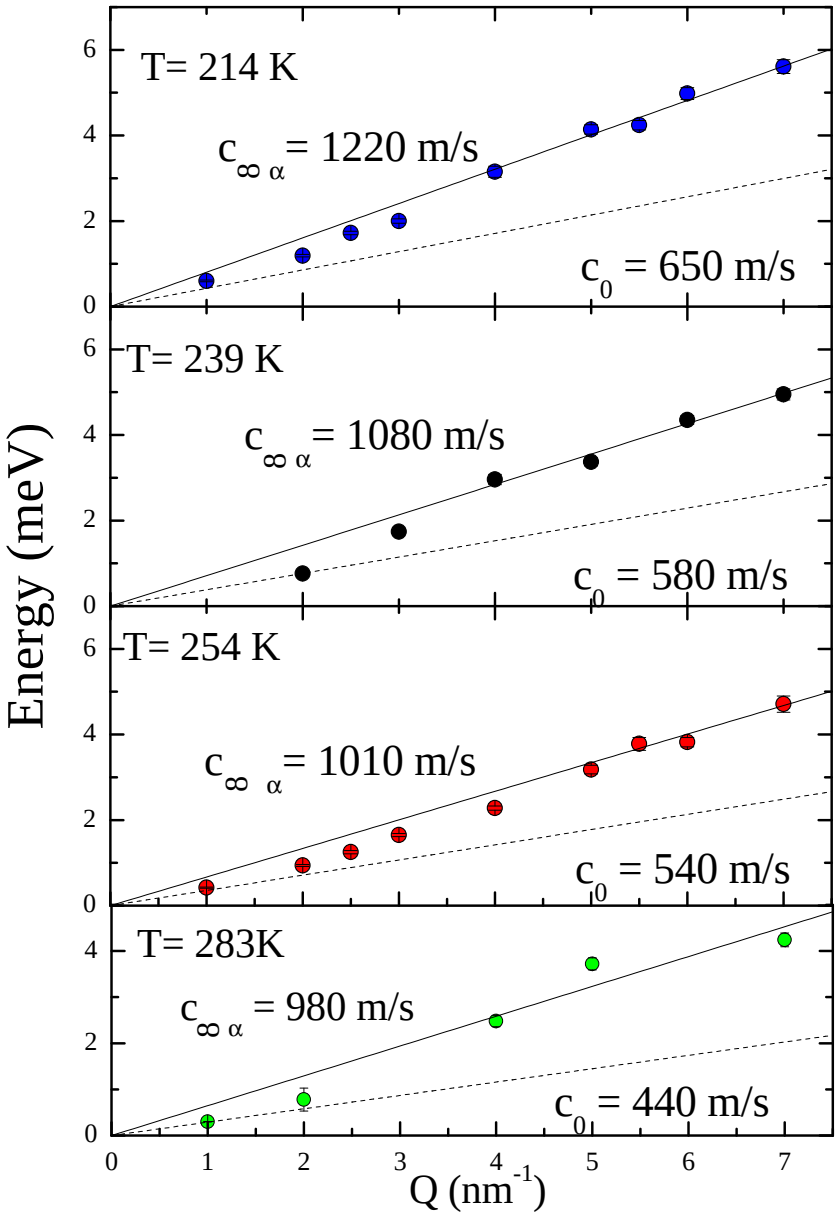

Figure 6.9. Dispersion curve at the indicated temperatures. The upper full lines are the linear fits to the high-Q data. The lower dashed lines indicate the adiabatic sound velocity as measured by Brillouin light scattering as shown in Section 6.2.

$c_o(Q)$ and $c_{\infty\alpha}(Q)$, derived from the viscoelastic analysis. Therefore, this finding confirms the hypothesis that the transition of $c(Q)$ is governed by the α- process. In particular, for Q larger than 4 nm^{-1}, the coincidence of $c(Q)$ and $c_{\infty\alpha}(Q)$ tells us that the α- process is

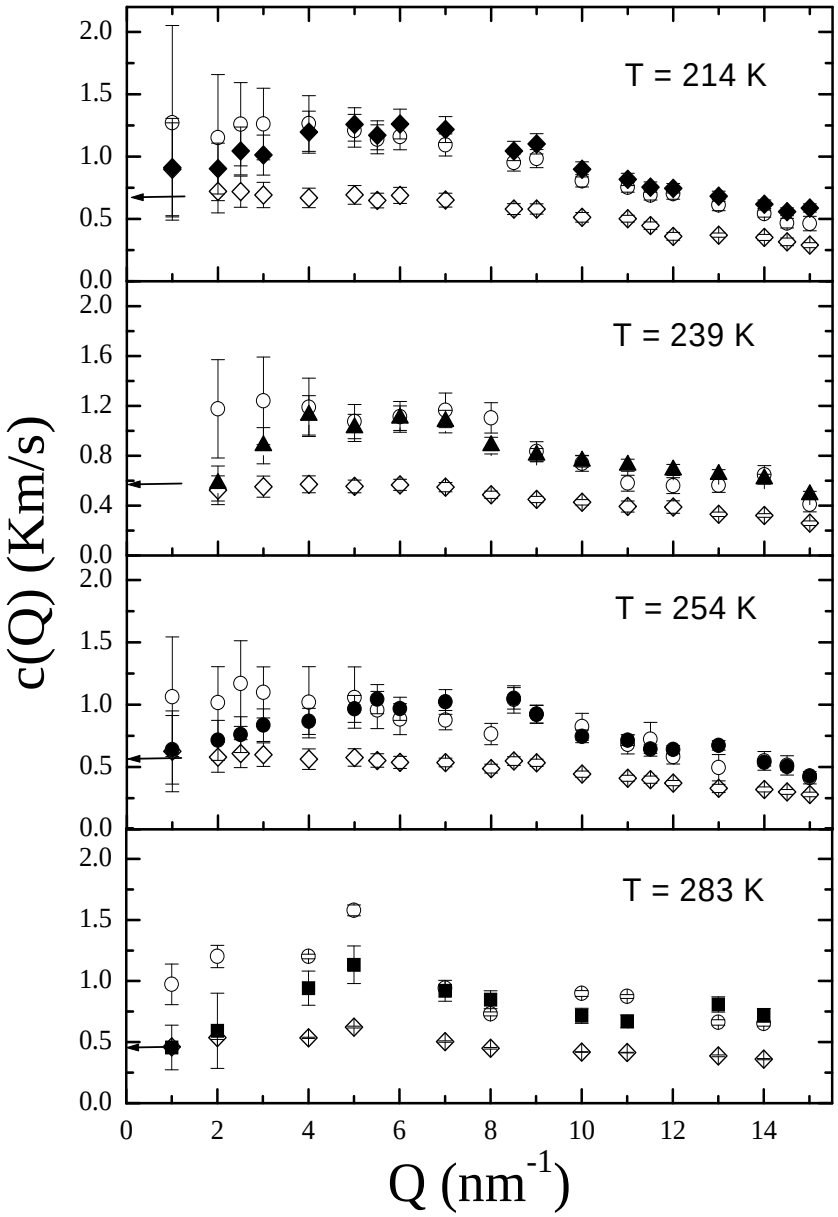

Figure 6.10. Q-dependence of the sound velocities $c_0(Q)$ (open diamonds) and $c_{\infty\alpha}(Q)$ (open circles) from a viscoelastic analysis, together with $c(Q)$ (full symbols) from Fig. 6.9. The value of the adiabatic sound velocity c_0 is indicated by the arrow [50].

not observed at time scales shorter than 0.2 *ps i.e.* at excitation frequencies for Q larger than 4 nm^{-1}. In the explored Q region, there is no evidence for a further dispersion of $c(Q)$ that could be associated to the μ- process. However, this two relaxation scenario,

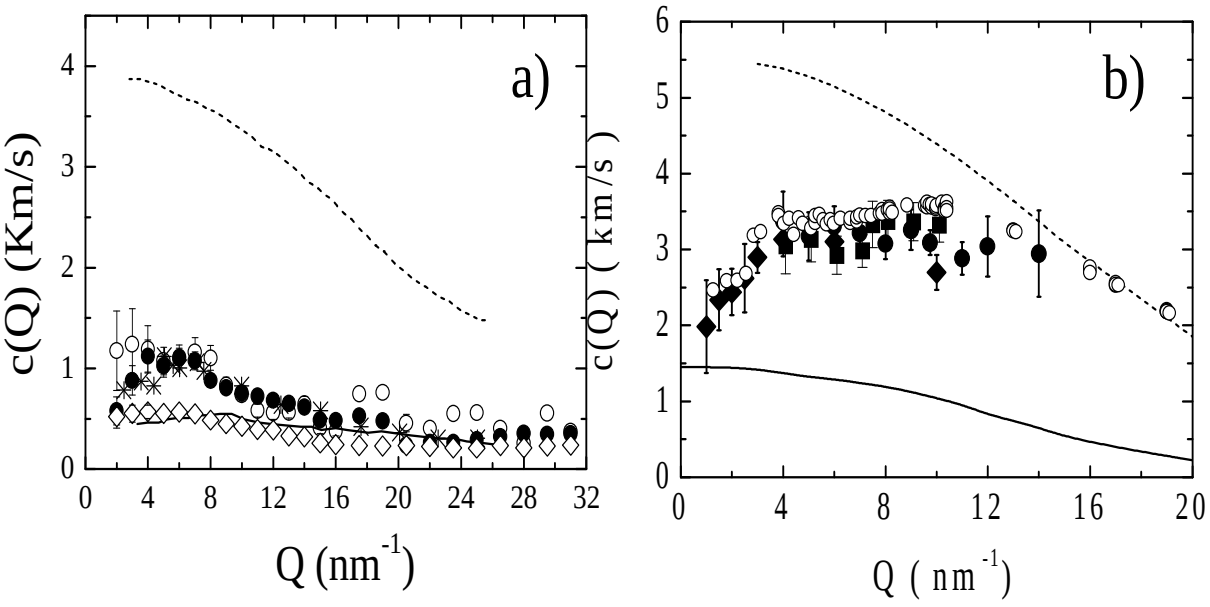

Figure 6.11. a)Q-dependence of the sound velocities at T = 239 K from this thesis: $c_0(Q)$ (open diamonds) and $c_{\infty\alpha}(Q)$ (open circles), $c(Q)$ (full circles) and at T = 203 K from MD results [51]: $c_0(Q)$ (solid line), $c_{\infty\mu}$ (dashed line), c(Q) (stars). b) Q-dependence of experimental and theoretical velocities of sound in water. Open circles, MD simulations [42]; full squares, circles and diamonds, IXS data [38]; solid (dashed) line, zero (infinite) frequency limit [43].

where both α and μ- process are active in HF, is supported by recent molecular dynamics simulation studies on HF [51, 52, 53].

Similarly to Figure 4.3 for liquid water, reported again here for completeness in Figure 6.11 b), in Figure 6.11 a) we compare the sound velocities at $T = 239\ K$ with numerical simulation results [51]: *i)* $c_o(Q)$ as derived from the simulated static structure factor (as explained in Section 3.2), *ii)* $c(Q)$ as derived from the maxima of the simulated longitudinal current spectra (as explained in Section 3.2) and *iii)* $c_\infty(Q)$ as derived from the fourth moment of the dynamic structure factor (as explained in Section 3.2, 3.5.5). It is worth to note that the quantity $c_{\infty\alpha}(Q)$ does not have a simple expression in terms of microscopic variables, and cannot be directly evaluated numerically. In spite of the slightly different thermodynamic points between the experiment (T=239 K) and the simulation (T=203 K), we observe an excellent agreement between the two common sets of data, i. e. for

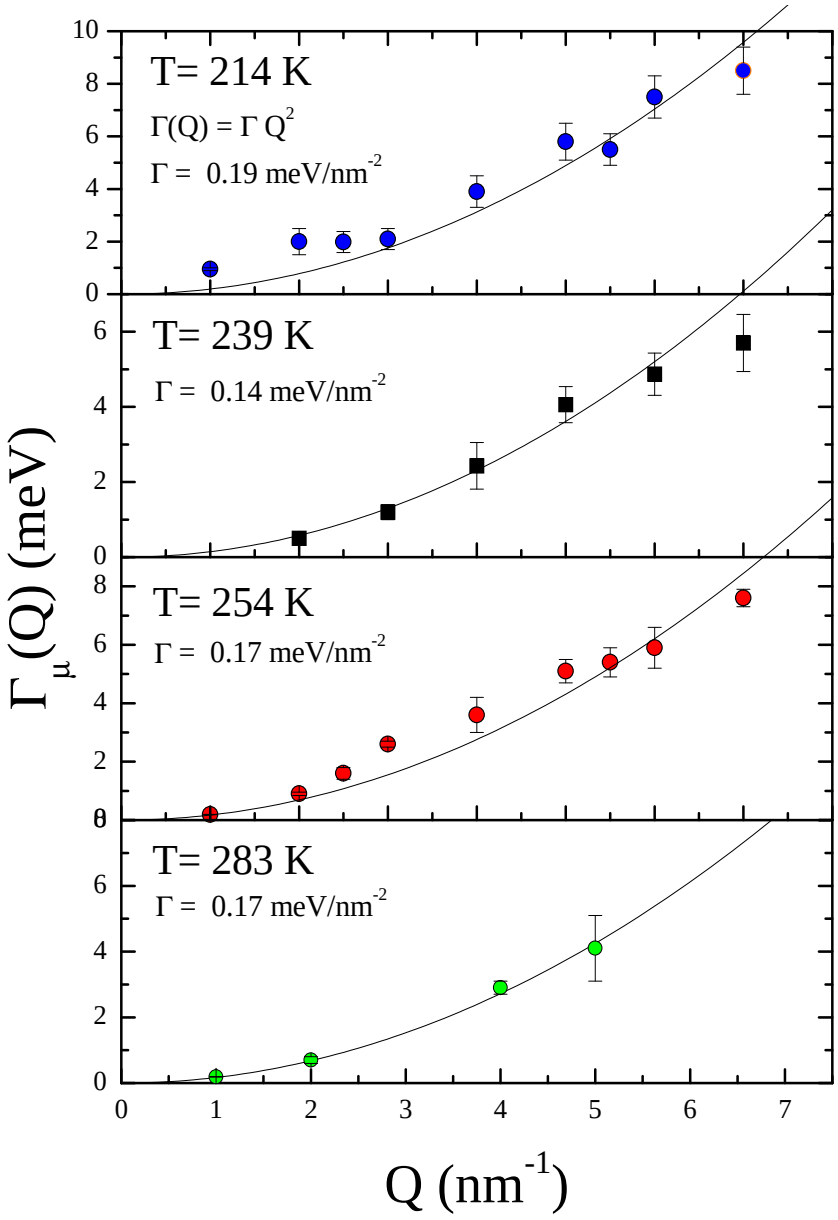

Figure 6.12. Q-dependence of the parameter $\Gamma_\mu(Q)$ (full circles) in liquid HF at the analysed temperatures from a viscoelastic analysis. The full lines are the parabolic fits to the low-Q data.

$c_o(Q)$ and $c(Q)$. This agreement implies that the interaction potential model used in the simulation matches well the properties of the real system. The important information emerging from the comparison of the data in Figure 6.11, is the very large difference

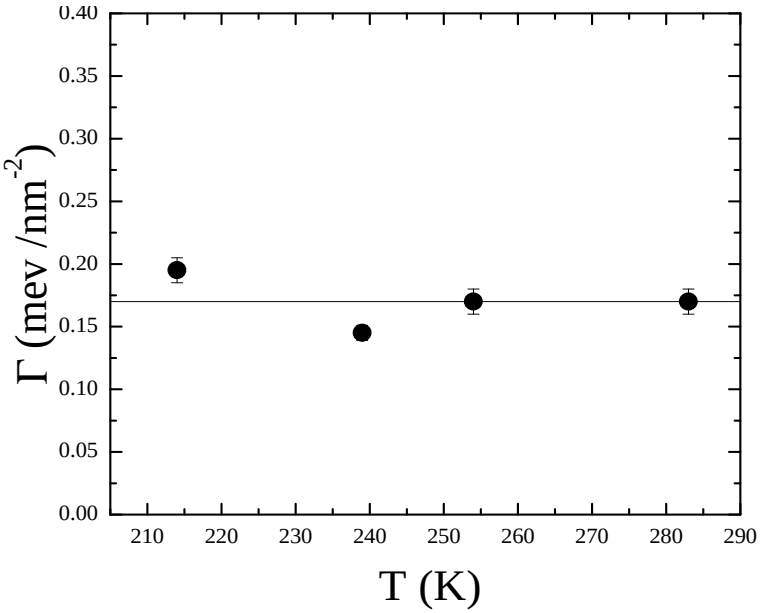

Figure 6.13. T dependence of the non relaxing parameter Γ in liquid HF. In this temperature range Γ is almost temperature independent (full line) being $\Gamma = (0.170 \pm 0.025) meV/nm^{-2}$

.

between the (measured) $c_{\infty\alpha} = c_{o\mu}$ and the (calculated) c_∞. This, in turn, implies not only the existence of the μ-process, but also that, in HF, this process has a relative strength substantially larger than in water over the whole considered Q range, which extends beyond the first peak in the static structure factor.

In Figure 6.12 the Q-dependence of the parameter $\Gamma_\mu(Q)$ of equation 6.10 is reported at the four analysed temperatures. The data follow a quadratic law, they have been fitted with a parabolic function

$$\Gamma_\mu(Q) = \Gamma Q^2$$

It yields values of Γ which appear to be temperature independent as shown in Figure 6.13 being $\Gamma = (0.170 \pm 0.025) meV/nm^{-2} = (2.6 \pm 0.4) \cdot 10^{-3} cm^2/s$. This result is consistent with previous findings according to which the microscopic relaxation is a temperature independent process.

The Q dependence of the relaxation time $\tau_\alpha(Q)$ is reported in Figure 6.14 at the four

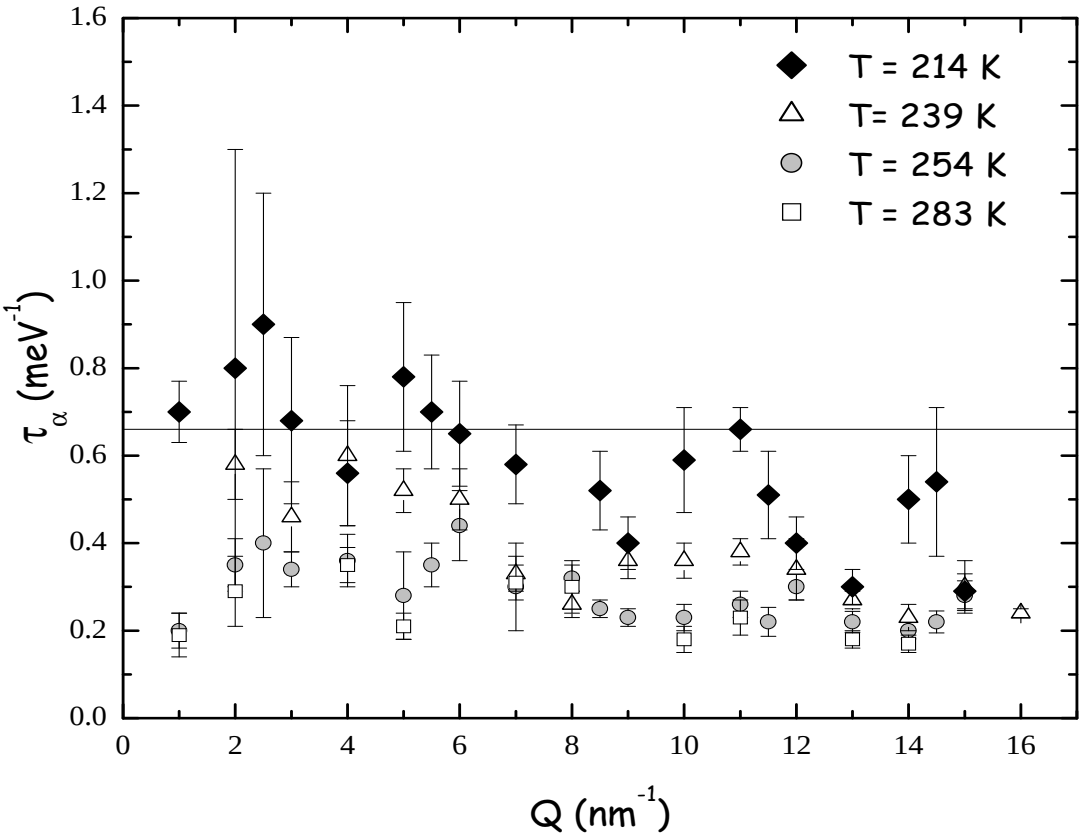

Figure 6.14. Q-dependence of the relaxation times $\tau_\alpha(Q)$ from the viscoelastic analysis at the indicated temperatures. The timescale corresponding to the experimental resolution $(1.5meV)$ (full line) is also reported.

investigated temperatures in the range $1 \div 16nm^{-1}$. It shows a decrease at increasing Q as already observed in water [1] and many other systems [2]. They are compared to the timescale corresponding to the experimental resolution (1.5 meV) (full line). A constant fit at low Q provides, for each temperature, Q independent values of this parameter. They are plotted on a linear scale in Figure 6.15 as a function of the temperature. In the explored temperature range, the τ_α behavior is well described by the Arrhenius law (full line):

$$\tau_\alpha(T) = \tau_0 e^{\frac{E_a}{K_B T}} \tag{6.11}$$

with an activation energy $E_a = (1.9 \pm 0.2) Kcal/mole$ and $\tau_0 = (6 \pm 2)10^{-15} s$. Exploiting the low Q values of $\tau_\alpha(Q)$ of Figure 6.15 together with the low Q extrapolations of the

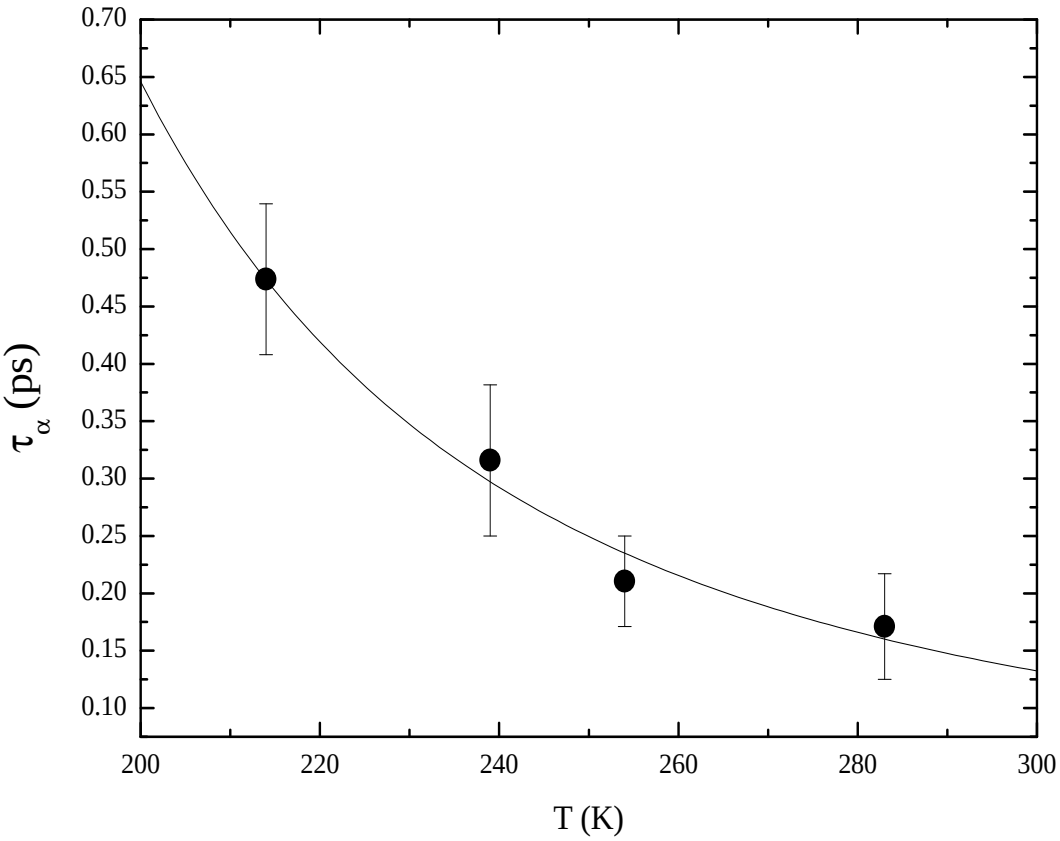

Figure 6.15. T dependence of the low-Q extrapolation of the relaxation times $\tau_\alpha(Q)$ of Figure 6.14 together with the Arrhenius fit (full line) of Eq. 6.11.

other fit parameters, it is possible to calculate the kinematic longitudinal viscosity ν_L from the relation 3.39:

$$\nu_L = \tau_\alpha(0)(c^2_{\infty\alpha}(0) - c^2_0(0)) + \frac{\Gamma_\mu(0)}{2Q^2} \tag{6.12}$$

where c_0 is the adiabatic sound velocity measured by Brillouin light scattering as discussed in Section 6.2. The values found are consistent with the hydrodynamic ones as shown in Figure 6.16. This numerical equivalence gives further support to the validity of the employed viscoelastic model. A molecular dynamics (MD) study of the transport coefficients (longitudinal and shear viscosity, thermal diffusivity and conductivity) of hydrogen fluoride [52] provides two values for the longitudinal viscosity η_L, one at T = 205 K $\eta_L(T = 205K) = 0.91 \cdot 10^{-2} g/cms$ and the other at T = 279 K $\eta_L(T = 279K) = 0.38 \cdot 10^{-2} g/cms$. They are reported in Figure 6.5 after rescaling for the

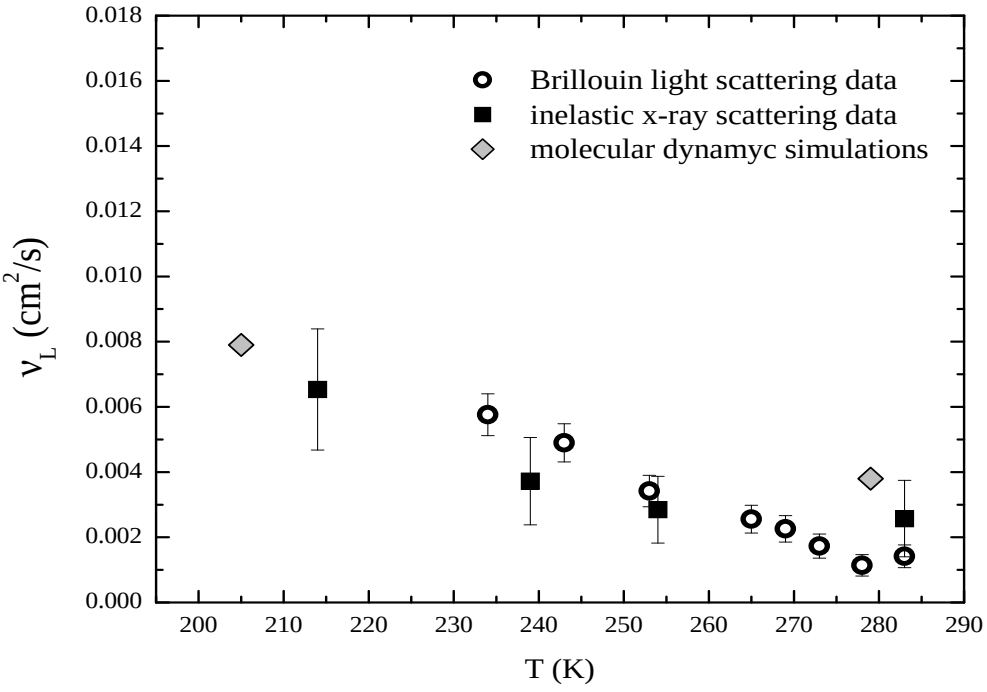

Figure 6.16. Temperature dependence of the kinematic longitudinal viscosity: from IXS as calculated through Eq. 6.14 (full squares), from the Brillouin light scattering values of section 6.2 (open circles) and from molecular dynamic simulations at $T = 205K$ and $T = 279K$ (full diamonds) [52].

density of Eq. 6.4 according to the relation $\nu_L(T) = \eta_L(T)/\rho(T)$.

In Figure 6.17 we report the relaxation time for hydrogen fluoride on an Arrhenius plot compared with the one of liquid water [1]. The activation energy found in water was $E_a = (3.8 \pm 0.6) Kcal/mole$ [1] while the one for hydrogen fluoride is $E_a = (1.9 \pm 0.2) Kcal/mole$ as previously discussed. It is worthwhile to relate the values of the activation energies to the different networks present in the two liquids. As described Chapter 4 hydrogen fluoride forms linear chains with one hydrogen bond for each molecule while the preferred arrangement of water is the three-dimensional tetraedric structure with two hydrogen bonds for each molecule. If we indicate with n_{HB-H_2O} and n_{HB-HF} the number of hydrogen bonds for H_2O and HF respectively and E_{a-H_2O}, E_{a-HF} the activation energies for the two liquids, the following relation is satisfied:

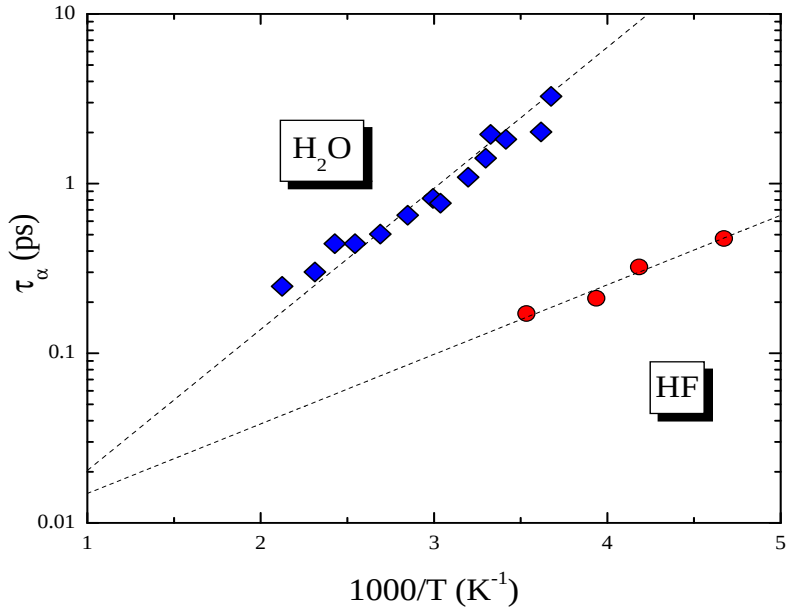

Figure 6.17. Arrhenius plot for the relaxation time as obtained from viscoelastic analysis of the dynamical structure factor for water (full diamonds) [1] and hydrogen fluoride; The dashed lines indicate the best linear fit to the data and their slop give an activation energy of $3.8 Kcal/mole$ for water and $1.9 Kcal/mole$ for HF.

$$\frac{E_{a-H_2O}}{n_{HB-H_2O}} \approx \frac{E_{a-HF}}{n_{HB-HF}} \tag{6.13}$$

In previous studies on water [54] the activation energy has been associated with that of the H-bond ($\approx 5 Kcal/mole$). The result of Eq. 6.13 reinforces the idea that the structural relaxation process involves the H-bond networks of the system and it seems also to suggest that the activation energy of the process is strictly related to the number of H-bonds to make and break more than to the strength of each H-bond.

Finally in Figure 6.18 we report the ratio $c_{\infty\alpha}/c_o$ for three hydrogen bonded liquid systems: water [38], hydrogen fluoride from this work, and methanol [55]. The x-axis represents the energy for each molecule, namely, the energy of each bond times the number of H-bonds for each molecule. In the case of water and HF we used the data of Table 4.2, in the case of methanol we considered an H-bond energy of $\approx -17 KJ/mole$ for each bond and one H-bond for each molecule. The data show a slight decrease of the ratio $c_{\infty\alpha}/c_o$ as the strength of the total H-bond energy decreases.

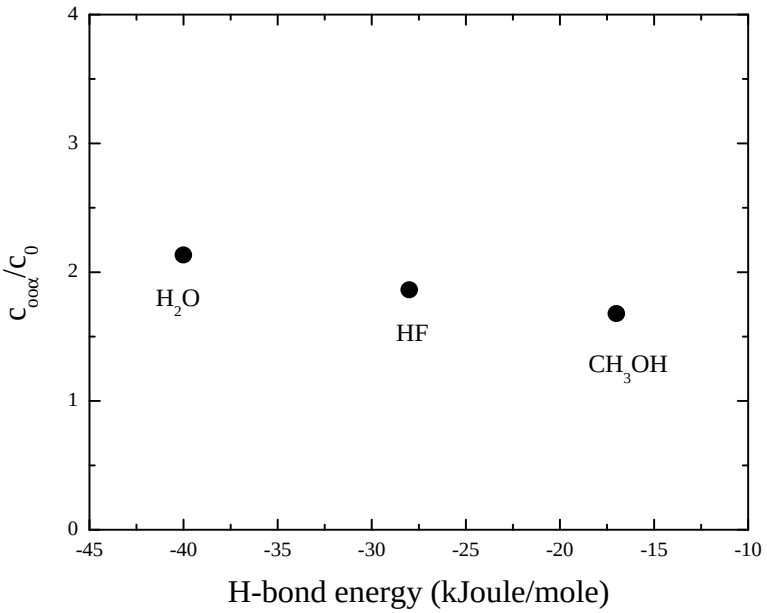

Figure 6.18. Ratio $c_{\infty\alpha}/c_0$ as a function of the hydrogen bond energy for each molecule in the case of three hydrogen bonded liquid systems: water, hydrogen fluoride and methanol [55].

6.3.4 Conclusions

In this section we have demonstrated that similarly to liquid water, the collective dynamics of liquid hydrogen fluoride is characterized by a **structural** relaxation process in the sub-picosecond time scale. It takes place in a Q range between $1 \div 7nm^{-1}$ and in a temperature region comprised between $214 \div 283K$. An accurate analysis done with two different models, the DHO and the viscoelastic, has shown the consistency of the two sets of results and the presence of a transition of the sound velocity from the low frequency limit to the high frequency one. This provide strong evidence for the existence of a relaxation process whose structural character is suggested by its temperature dependence. A parallel with existing MD simulations [51] reveals a large difference between the measured $c_{\infty\alpha}$ and the calculated c_∞, implying the presence of a further relaxation, that we identify as the **microscopic** relaxation process discussed in section 3.5.3. Finally, comparing BLS and IXS measurements and MD simulations, we provide a strong indication that, similarly to simple and glass-forming liquids, also hydrogen bonded liquids present *two* relaxation processes affecting their high frequency collective dynamics. These two processes produce a

phenomenology consistent with the α- and μ- processes, thus suggesting their universality in the liquid state. The strengths of these two processes are, however, dependent on the specific system. In particular - contrary to simple liquids where $c_\infty/c_o \approx 1.2$ and $c_{\infty\alpha}$ differs from c_o by few percent [5] - the strengths of these relaxation processes are much larger in hydrogen bonded liquids: at low Q in both water and HF $c_{\infty\alpha}/c_o \approx 2$, while $c_\infty/c_o \approx 3$ in water and ≈ 7 in HF. It is intriguing to understand the origin of these quantitative differences, and it could be of interest to asses whether they are correlated to the different hydrogen bond networks existing in water and HF.

6.4 Study of the high frequency collective dynamics of $(HF)_x(H_2O)_{1-x}$ by inelastic x-ray scattering

6.4.1 Experimental data as a function of Q and concentration

We studied the dynamic structure factor $S(Q,\omega)$ of five different mixtures of water and hydrogen fluoride $(HF)_x(H_2O)_{1-x}$ with x = 0, 0.2, 0.4, 0.73, 1. We worked at fixed temperature $T = 283\ K$ and at normal pressure. The $S(Q,\omega)$ has been investigated as a function of wave vector Q in the range $1 \div 15 nm^{-1}$. Each scan took about 180 min and each spectrum at fixed Q was obtained by summing up to 3 scans. The data have been normalized to the intensity of the incident beam. The empty cell contribution, represented by the Teflon windows, has already been subtracted to the total scattered intensity. The IXS spectra are reported in Figure 6.19. The $S(Q,\omega)$ shape shows a strong dependence from the concentration passing gradually from a situation in which a peak centered at zero energy transfer is present (pure HF) to the case of pure water with inelastic peaks clearly distinguishable with the naked eye.

6.4.2 DHO analysis

As already described in the case of pure HF, a preliminary analysis of the spectra has been accomplished by fitting the data with the DHO model. In Figure 6.20 we report the resulting line-shapes superimposed to the data. The contribution of the central peak and of the inelastic side peaks are individually shown.

The main fit parameter, $\Omega(Q)$, provides an estimate of the current maxima. It has been

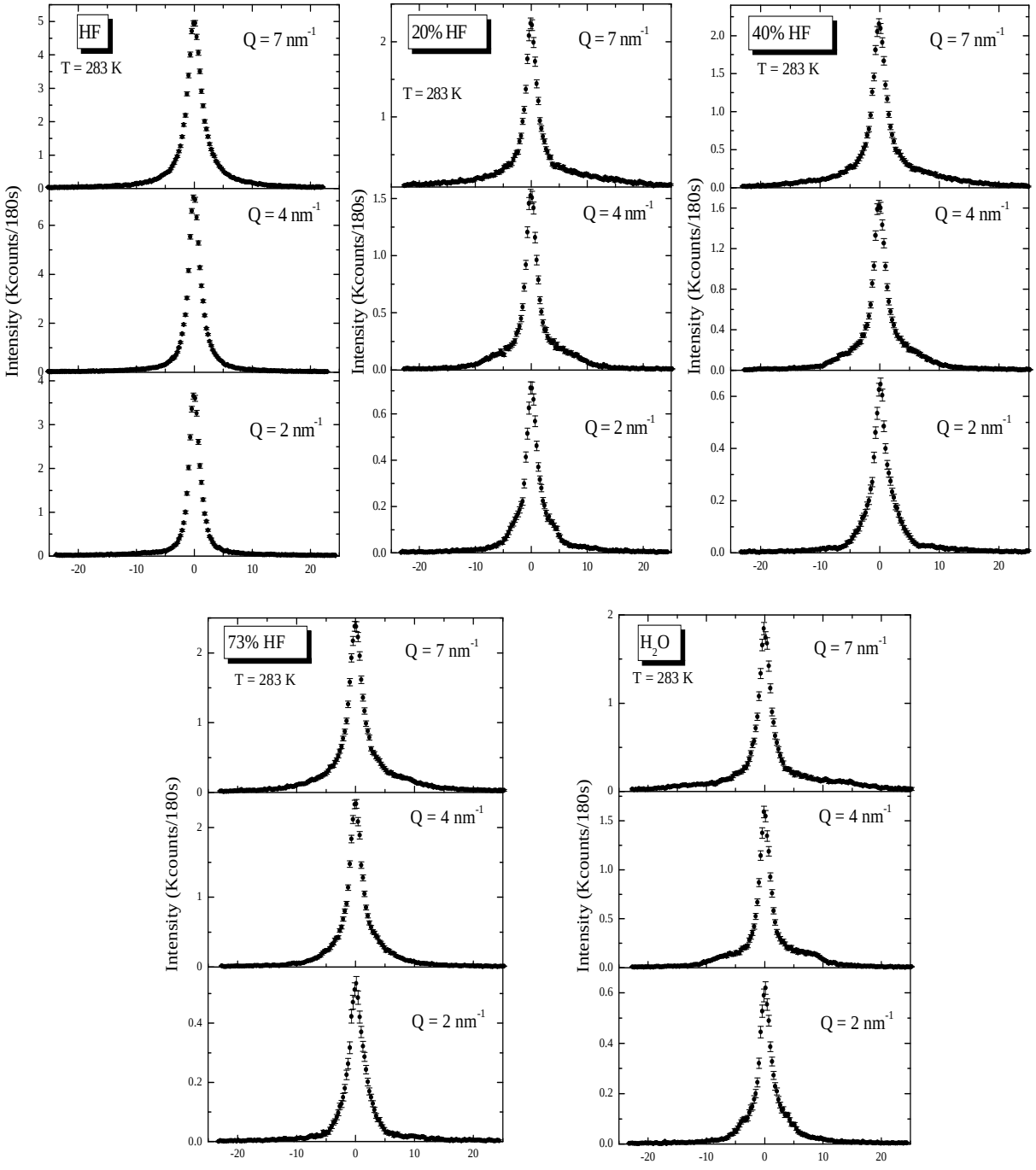

Figure 6.19. IXS spectra of $(HF)_x(H_2O)_{1-x}$ solutions with x = 0,0.2,0.4,0.73 compared with pure HF at $T = 283\ K$ at some selected Q values.

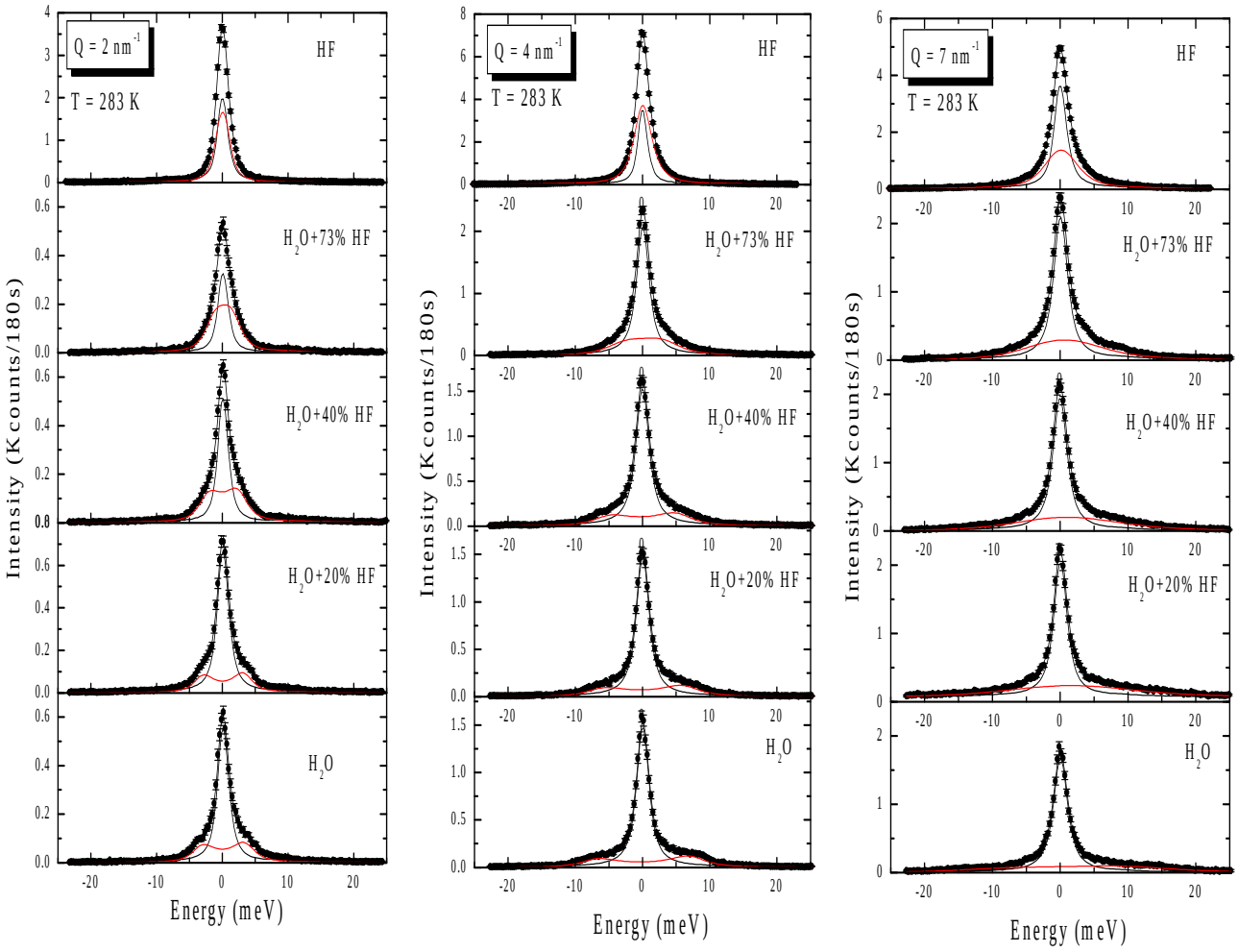

Figure 6.20. IXS spectra of $(HF)_x(H_2O)_{1-x}$ solutions with x = 0, 0.2, 0.4, 0.73 compared with pure HF at $T = 283\ K$ at some selected Q values shown together with the total fits and the individual components.

plotted in Figure 6.21 as a function of Q in the range $1 \div 9nm^{-1}$ at the investigated concentrations. As with pure liquids the dispersion curves of these binary solutions show a linear behaviour in the low Q region. It may be noted that their slope decreases at increasing concentration of hydrogen fluoride. To allow a more detailed analysis we report in Figure 6.22 the dispersion curve at each concentration individually plotted and compared with the respective adiabatic sound velocity [44]. From this graph it is evident that passing from pure hydrogen fluoride (bottom) to pure water (top) the transition of the apparent sound velocity $\Omega(Q)/Q$ takes place at decreasing Q with decreasing concentra-

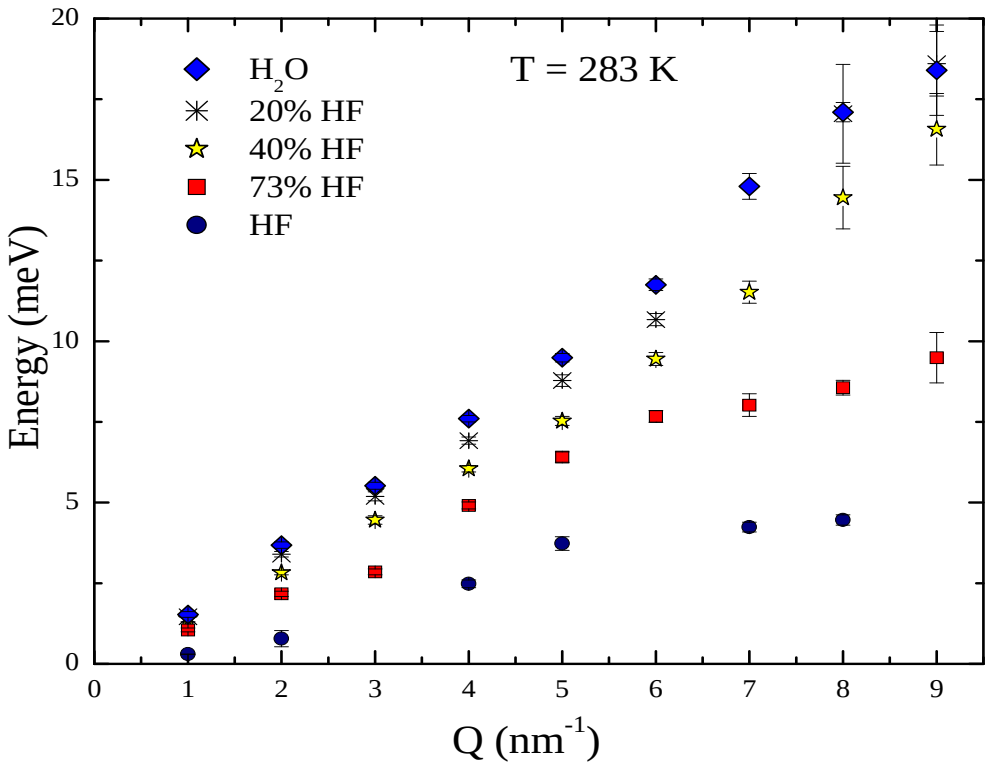

Figure 6.21. Dispersion curves of $(HF)_x(H_2O)_{1-x}$ solutions with $x = 0$ (diamonds), 0.2 (asterisk), 0.4 (stars), 0.73 (squares). They are compared with the one of pure HF (circles) at $T = 283\ K$.

tion of HF falling in the region $Q \leq 1nm^{-1}$ for the 40 % HF and 20 % HF solutions and for pure water. In these last three cases a linear fit in the $1 \div 7nm^{-1}$ Q range provides a value of the sound velocity substantially higher than the adiabatic one. In the case of pure HF and 73 $\%HF$ solution, the dispersion curves show a linear dependence for Q between 4 nm^{-1} and 7 nm^{-1} with a slope corresponding to a sound velocity higher of the adiabatic one. Furthermore, in the $1 \div 4nm^{-1}$ Q region, the data show a transition of the sound velocity $c(Q)$ from the low frequency value to the higher one. This means that, as in the case of pure HF at different temperatures, the structural or α relaxation discussed in Section 3.5.3 is present at higher concentration of HF. However our results on pure water at $T = 283\ K$ cannot be directly compared with the ones of Figure 4.2 due to the two different used fitting procedures. Here in fact we fitted the inelastic part of the spectra with a simple DHO model while in the data of Figure 4.2 a further inelastic

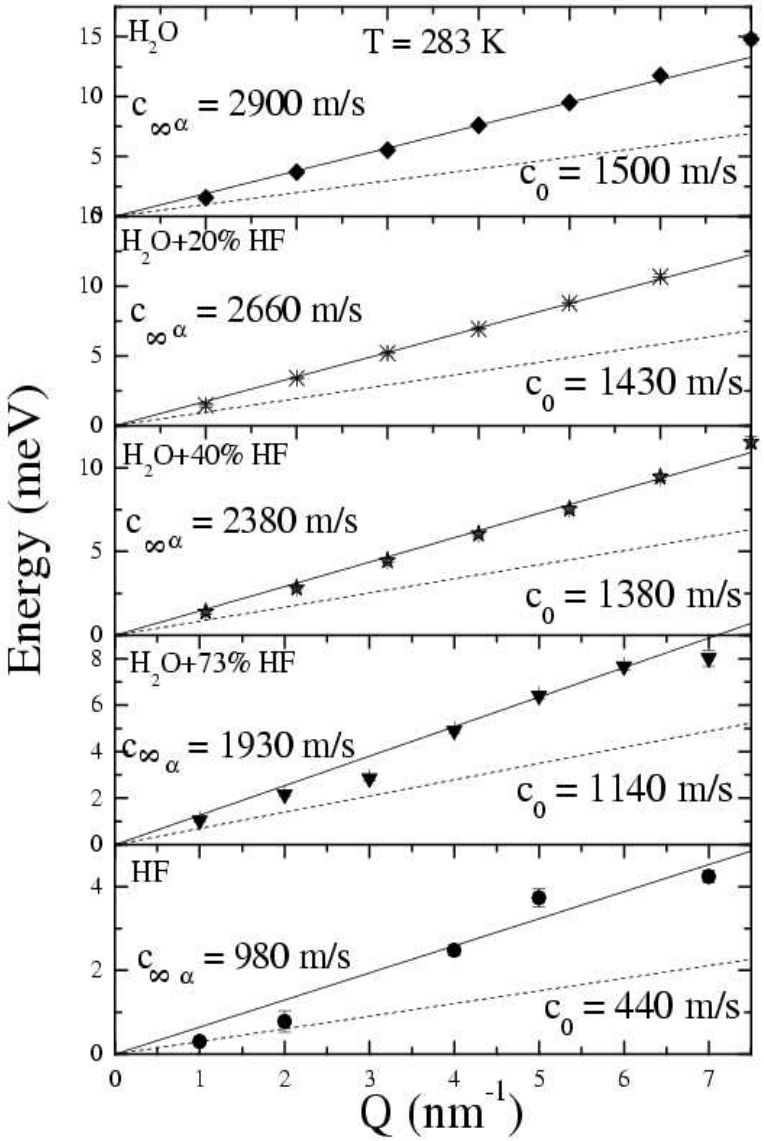

Figure 6.22. Dispersion curves for $(HF)_x(H_2O)_{1-x}$ solutions at the indicated concentrations at $T = 283\ K$. The upper full lines corresponds to the linear fits in a Q range described in the text. The slope of the lower dashed lines corresponds to the adiabatic sound velocity [44].

contribution has been introduced to take into account the transverse modes.

A comparison between the high frequency sound velocity $c_{\infty\alpha}$, as obtained by IXS and the adiabatic sound velocity, as obtained from reference [44], is reported in Figure 6.23(a). Changing the concentration, the $c_{\infty\alpha}/c_0$ ratio shown in Figure 6.23(b) is always close to

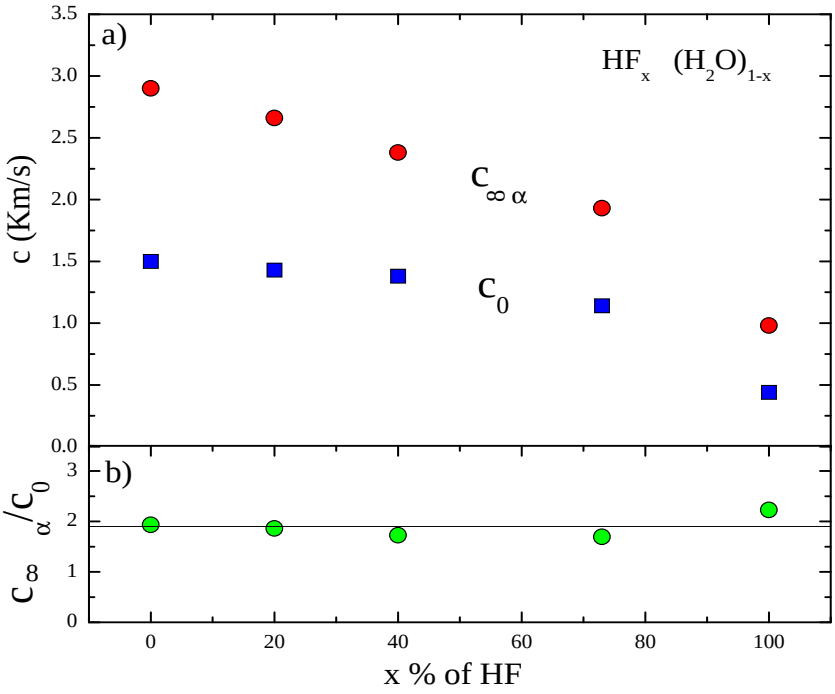

Figure 6.23. (a) Behaviour of the sound velocity in $(HF)_x(H_2O)_{1-x}$ solutions as a function of the concentration at $T = 283\ K$: c_0 (full squares), $c_{\infty\alpha}$ (full circles). (b) Sound velocities ratio $c_{\infty\alpha}/c_0$.

two as for the two limit compounds water and HF.

In order to understand the influence of the mass of the hydrated clusters of the HF molecules on the longitudinal modes and to find therefore a mass scaling model for the sound velocity, we analyse in more detail the way in which, depending on the concentration, the molecules of water and HF arrange themselves to form different aggregates. Detailed studies on aqueous solutions of hydrogen fluoride [56, 57, 58, 59, 60, 61] revealed the presence of a strongly bound complex, dynamically fluctuating between two main structures:

$$FH \cdots H_2O \rightleftharpoons F^- \cdots H_3O^+$$

where the dots $(\cdots)$ indicate the presence of a link due to a strong hydrogen bond. This behaviour was observed at dilute aqueous solutions as well as at higher concentrations (50%). These informations lead us to image our solutions as composed by clusters of HF and H_2O molecules whose mass is easily calculated. To simplify the description of

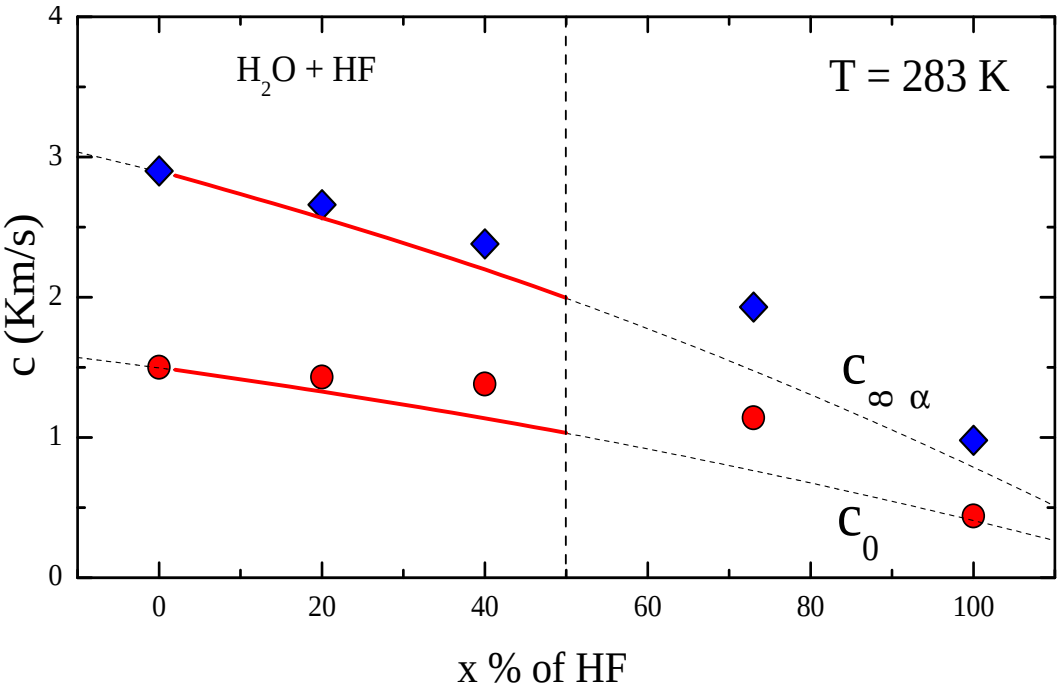

Figure 6.24. Infinite frequency sound velocity $c_{\infty\alpha}$ (full diamonds) as measured by IXS and adiabatic sound velocity [44] (full circles) in $(HF)_x(H_2O)_{1-x}$ solutions as a function of the concentration at $T = 283\ K$ compared with the values calculated according to the mass scaling law described in the text (full line).

our system it is suitable to define with X_1 the new aggregate and in particular to set $X_1 = FH\cdots H_2O$. Then we indicate with M_{H_2O}, M_{HF}, M_{X_1}, the masses of hydrogen fluoride, water and the new entity respectively whose values are $M_{H_2O} = 18$ $M_{HF} = 20$ $M_{X_1} = 38$

To calculate the scaling mass law for the sound velocity, indicating with x the concentration of HF, we can imagine that in the region $x < 0.5$ the X_1 aggregates are plunged in a see of HF molecules; while for $x = 0.5$ we deal with a liquid system made up of only X_1 clusters. The solution is equivalent to a liquid composed of particles with an average atomic mass [62, 63, 64]

$$M_{AV}(x) = \alpha_1(x)M_{X_1} + \beta_1(x)M_{HF}$$

where $\alpha_1(x) = x/(1-x)$ and $\beta_1(x) = (1-2x)/(1-x)$.

A simple mass scaling law allows an estimation of the measured sound velocity as a

function of concentration [62, 63, 64]

$$c(x) = c_{H_2O}\sqrt{\frac{M_{H_2O}}{M_{AV}(x)}}$$

The measured values and the calculated one are reported in Figure 6.24. The theoretical values of $c(x)$ (full line) calculated in the range $0 < x \leq 0.5$ have been extrapolated up to $x = 1$.

6.4.3 Viscoelastic analysis

Whenever a relaxation process is present, a more detailed analysis of the spectra is accomplished in term of the viscoelastic model (Section 3.5.5). As in the case of HF, we use the procedure described in sections 6.3.3 to get information on the dynamical behaviour of the main fit parameters $c_{\infty\alpha}(Q)$, $c_0(Q)$, $\tau_\alpha(Q)$ and $\Gamma_\mu(Q)$ at all the investigated concentrations. In Figure 6.25 $c_{\infty\alpha}(Q)$, $c_0(Q)$ are reported together with the apparent sound velocity $c(Q) = \Omega(Q)/Q$ obtained from the dispersion curves $\Omega(Q)$ of Figure 6.22. We observe that in the case of water, 20 % HF and 40 % HF solutions the c(Q), found with the DHO analysis, lies completely on the $c_{\infty\alpha}$ points except for $Q = 1nm^{-1}$; this reinforce the idea that in these three cases the transition of the sound velocity $c(Q)$ has already happened and that the system is un-relaxed. At decreasing concentration and in particular for 73 % HF solution and pure HF the transition of $c(Q)$ found with the DHO analysis takes place between the values of $c_0(Q)$ and $c_{\infty\alpha}(Q)$ supporting the hypothesis of the presence of the α relaxation in both cases. The parameter related to the strength of the microscopic relaxation process $\Gamma_\mu(Q) = \Delta_\mu^2\tau_\mu(Q)$ is reported at all the investigated concentrations in Figure 6.26. As already observed in HF, it follows a quadratic behaviour. The result of the fit, done with the parabolic function,

$$\Gamma_\mu(Q) = \Gamma Q^2$$

provides values of Γ which are plotted in Figure 6.27. While in the case of HF Γ turned out to be temperature independent, it shows a dependence on the concentration in the case of $(HF)_x(H_2O)_{1-x}$ solutions, in particular we observe that, being the ratio $\Gamma_{H_2O}/\Gamma_{HF} \approx 2$ (the two limiting points in the graph), the microscopic relaxation process is faster in HF than in water.

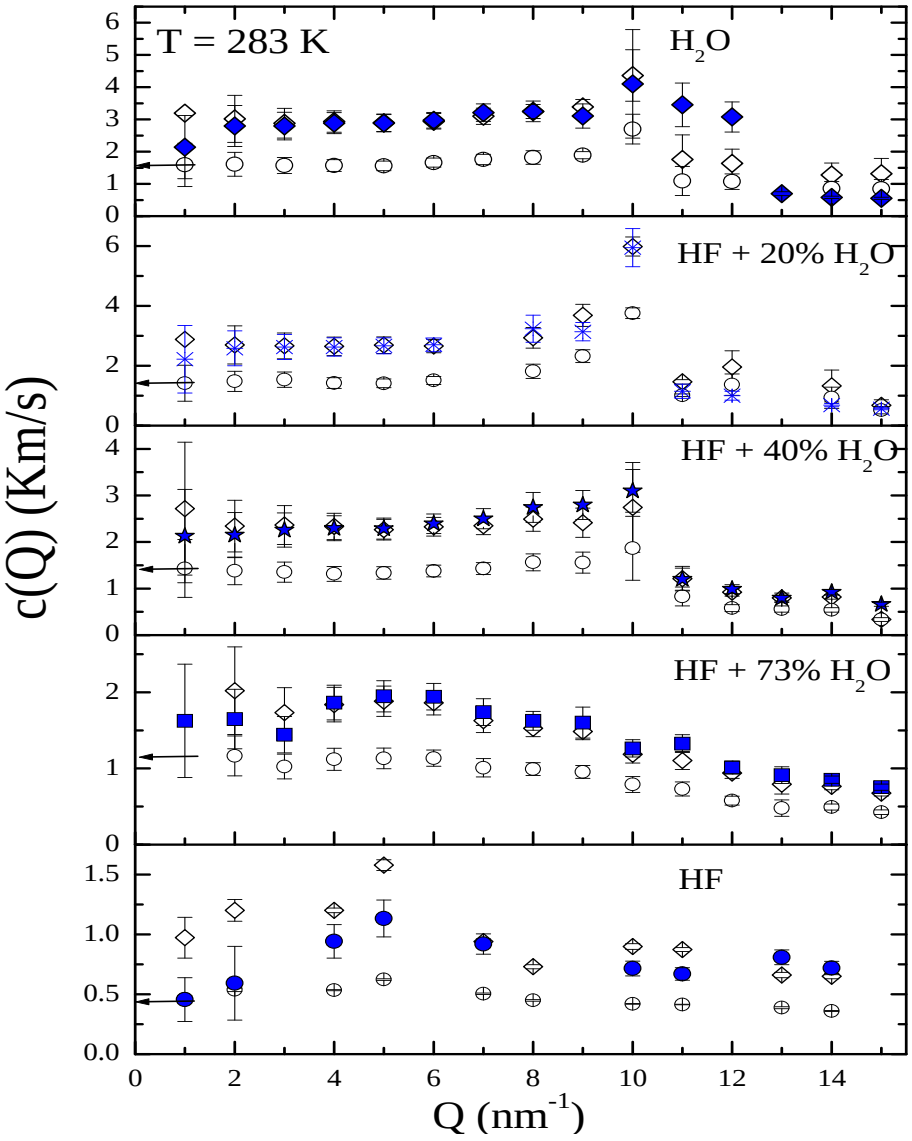

Figure 6.25. Q-dependence of the sound velocities $c_0(Q)$ (open diamonds) and $c_{\infty\alpha}(Q)$ (open circles) from a viscoelastic analysis in $(HF)_x(H_2O)_{1-x}$ solutions, together with $c(Q)$ (full symbols) from Fig. 6.22 at $T = 283\ K$. The value of the adiabatic sound velocity c_0 is indicated by the arrow [44].

The Q dependence of the last fit parameter $\tau_\alpha(Q)$ is shown in Figure 6.28 at all the investigated concentrations, it is worthwhile to note that the values of $\tau_\alpha(Q)$ in the case of pure HF are lower than the ones for water, this means that in hydrogen fluoride the structural relaxation is quicker than in water. This can be attributed to the fact that

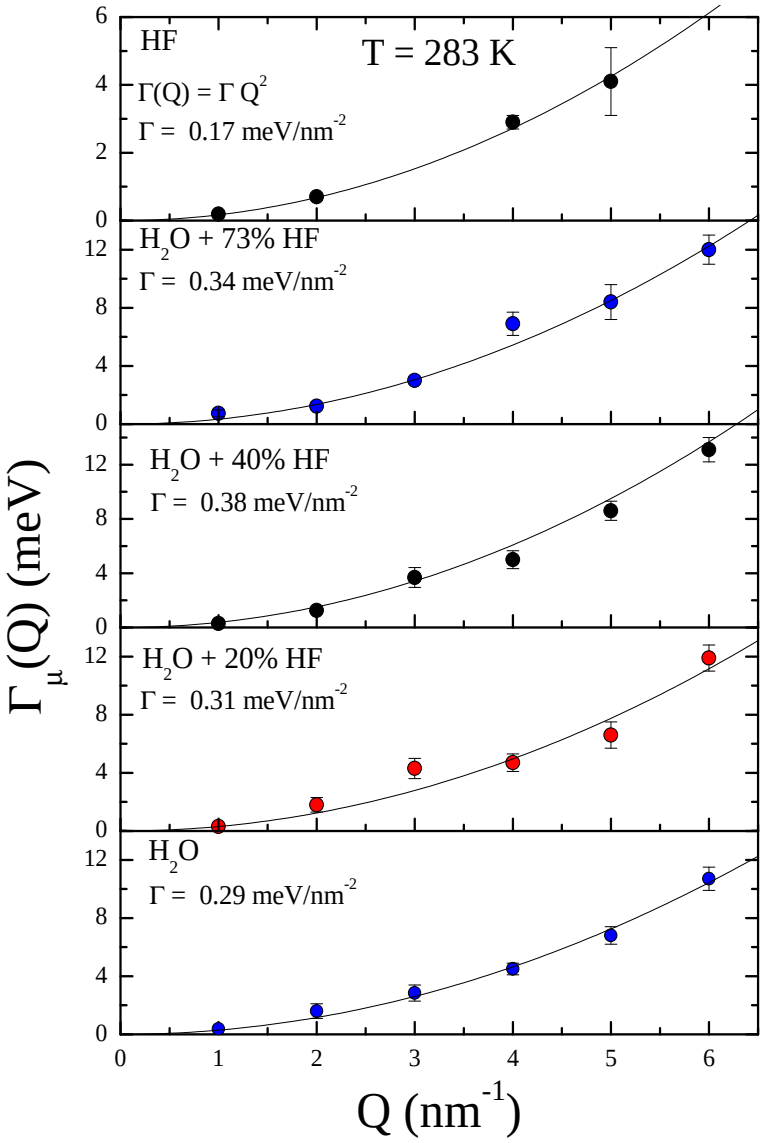

Figure 6.26. Q-dependence of the parameter $\Gamma_\mu(Q)$ (full circles) from a viscoelastic analysis in $(HF)_x(H_2O)_{1-x}$ solutions at $T = 283\ K$. The full lines represent the parabolic fits to the low-Q data.

the chain-like structures of HF molecules are "more free" respect to the three dimensional clusters of water. From the graph it comes out also that the error bars on the data decrease passing from pure water to pure HF as a proof of the fact that the viscoelastic analysis becomes more and more appropriate. A constant fit of the data in the low Q region has provided values of $\tau_\alpha(0)$ plotted in Figure 6.29(a). In Figure 6.29(b) we report the

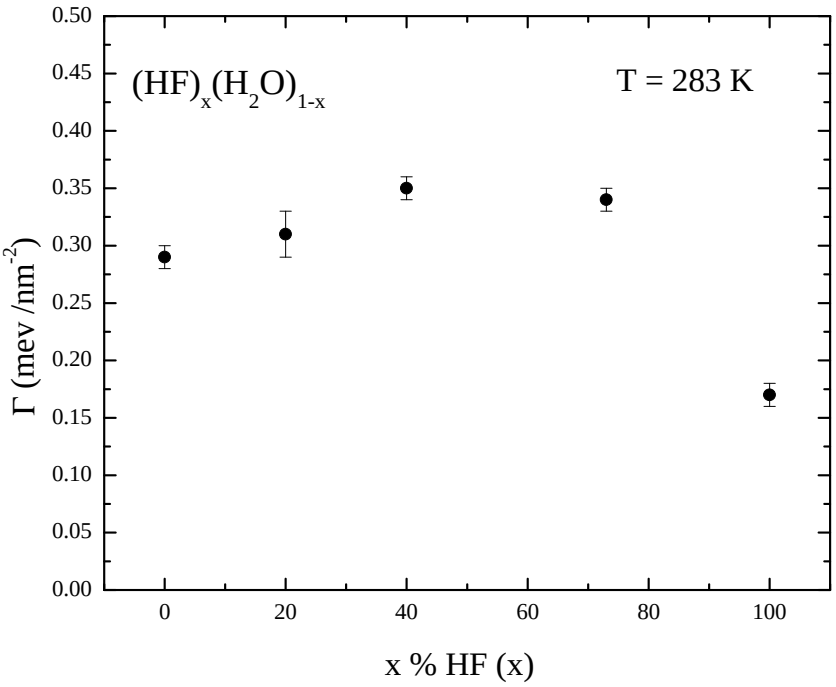

Figure 6.27. Dependence on the concentration of HF of the parameter Γ in $(HF)_x(H_2O)_{1-x}$ solutions, at $T = 283\ K$.

kinematic longitudinal viscosity as a function of concentration of HF. It has been obtained by exploiting the low Q values of the four viscoelastic fit parameters $c_0(Q)$, $c_{\infty\alpha}(Q)$, $\Gamma_\mu(Q)$ and $\tau_\alpha(Q)$ related through the expression 3.39:

$$\nu_L = \tau_\alpha(0)(c^2_{\infty\alpha}(0) - c^2_0(0)) + \frac{\Gamma_\mu(0)}{2Q^2} \tag{6.14}$$

already used in the case of pure HF. This relation has been applied in the hypothesis of absence of the contribution to the viscosity due to the fluctuations of concentration, hypothesis justified by the fact that the two pure liquids have a very similar molecular mass. The experimental data have been compared with the predictions of the Raoult's law of classical physical chemistry []. According to it a given property P in a binary solution, is described in terms of a simple linear dependence on the composition of the solution according to the law [65, 66]:

$$P = x_1P_1 + x_2P_2$$

where x_is are the mole fraction and P_is are the values of the property P of the pure

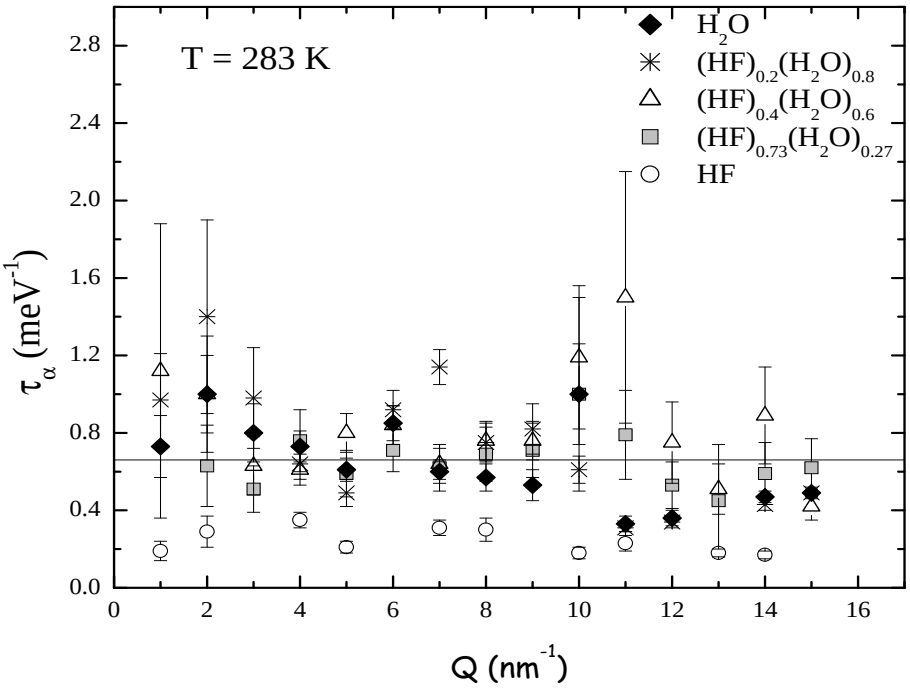

Figure 6.28. Q-dependence of the relaxation time $\tau_\alpha(Q)$ from a viscoelastic analysis in $(HF)_x(H_2O)_{1-x}$ solutions at $T = 283\ K$. The time scale corresponding to the experimental resolution is also reported (full line).

liquids. The dashed line on Figure 6.29(b) is the result of the Raoult's law applied to the kinematic longitudinal viscosity ν_L according to:

$$\nu_L(x) = x\ \nu_{L-HF} + (1-x)\ \nu_{L-H_2O} \tag{6.15}$$

where x is the concentration of HF, $\nu_{L-HF} = 0.003\ cm^2/s$ and $\nu_{L-H_2O} = 0.035\ cm^2/s$ are the experimental values of nu_L for the two pure liquids. The comparison of the theoretical law with the linear fit to the data (solid line) shows a good agreement. This finding reinforce the hypothesis that, for these systems, the fluctuations of concentration can be really neglected without introducing any deviation of the kinematic longitudinal viscosity from the Raoult's law.

6.4.4 Conclusions

In this section, we have characterized the structural relaxation process in $(HF)_x(H_2O)_{1-x}$ solutions as a function of the concentration (x= 0, 0.2, 0.4, 0.73, 1) at fixed temperature

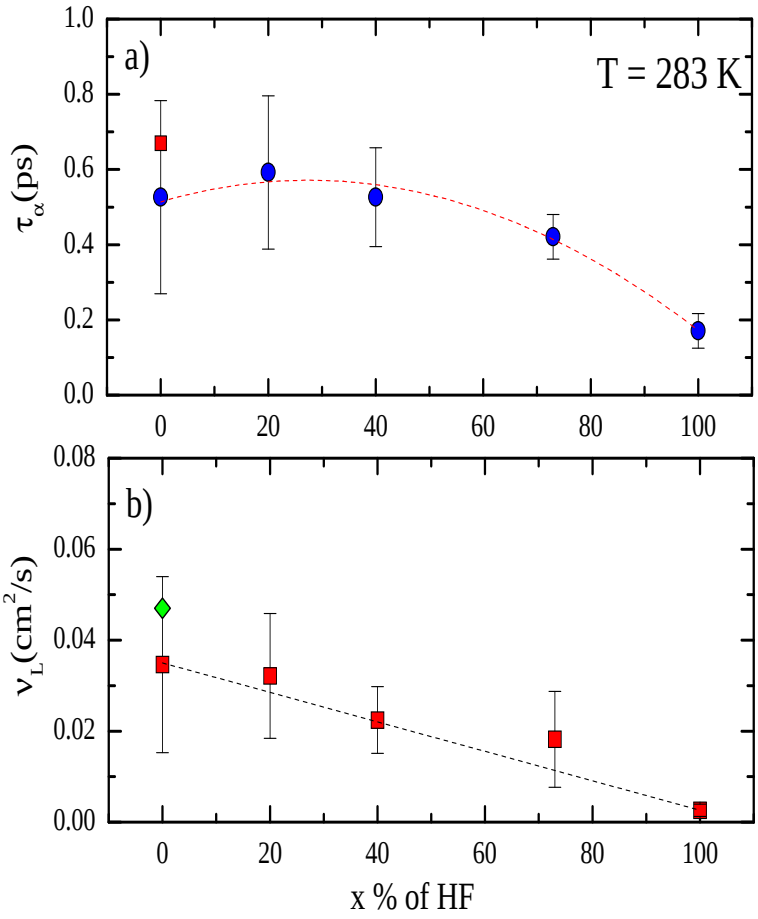

Figure 6.29. (a) Dependence on the concentration of the relaxation time $\tau_\alpha(0)$ in $(HF)_x(H_2O)_{1-x}$ solutions at $T = 283\ K$ as obtained from Figure 6.28 in the limit $Q \to 0$. The value for pure water (x=0) from ref [1] is also reported. The dashed line is a guide for the eye. (b) Dependence on the concentration of the kinematic longitudinal viscosity ν_L in $(HF)_x(H_2O)_{1-x}$ solutions at $T = 283\ K$ as obtain from Eq. 6.14 (squares); linear fit to the data (solid line); kinematic longitudinal viscosity as calculated from the Raoult's law of Eq. 6.15 (dashed line). The value for pure water (x=0) from ref [1], is also reported.

(T = 283 K). As preliminary analysis, we fitted the data with the DHO model, the derived dispersion curves show a linear behaviour in the low Q region with slopes decreasing at increasing concentration of hydrogen fluoride. The structural relaxation has been observed at higher concentration of HF and the ratio $c_{\infty\alpha}/c_0$ has been found almost independent on the concentration and close to two. A mass scaling model for the sound

velocity has been proposed, it allows to write an expression for the sound velocity c(x) as a function of the concentration x of HF. A more detailed analysis in term of the viscoelastic model supports the results found with the DHO model on the structural relaxation giving further informations on its time scale. A comparison between the two limit case, water and HF, shows that in HF the structural relaxation is faster than in water being $\tau_\alpha(Q \to 0)_{H_2O}/\tau_\alpha(Q \to 0)_{HF} \approx 3$. This is attributed to higher degree of freedom of the chain-like structure of HF respect to the three dimensional clusters of water.

Conclusions

In this Thesis we have presented a detailed study of the dynamic structure factor $S(Q,\omega)$ of two hydrogen bonded (HB) liquid systems: hydrogen fluoride HF and $(HF)_x(H_2O)_{1-x}$ solutions. The collective dynamics of HF has been investigated as a function of the temperature in the range $214 - 283\ K$ with two different techniques: Brillouin light scattering (BLS) and inelastic X-rays scattering (IXS). $(HF)_x(H_2O)_{1-x}$ solutions have been studied at fixed temperature ($T = 283\ K$) as a function of the concentration ($x = 0,\ 0.2,\ 0.4,\ 0.73,\ 1$). To characterize the relaxation phenomena of these associated liquids, we presented a comparative study of HF, the inorganic system with the strongest hydrogen bond, and water with the aim to establish a connection between the dynamical properties of these systems and the specific HB arrangement (number of bonds, strength, geometry). We found that similarly to liquid water, in the investigated temperature range, the collective dynamics of liquid hydrogen fluoride is characterized by a **structural** relaxation process in the sub-picosecond time scale. The data have been accurately analysed in terms of two different models: the DHO and the viscoelastic ones.

- The consistency of the two sets of results revealed the presence of a transition of the sound velocity from the low frequency limit to the high frequency one. This provided evidence for the existence of a relaxation process whose structural character was suggested by its temperature dependence.

- The measured relaxation time τ_α in the explored temperature range is comprised between 0.17 and 0.47 ps; as in water it lies in the sub-picosecond time scale [1]. Molecular dynamics simulations in water [67, 68] have shown that the bond lifetime is of the order of sub-picosecond and has an Arrhenius temperature dependence. This result leads to think that in HB liquid systems the structural relaxation time is related to the lifetime of the HB.

- The strength of the structural relaxation in HF is such that, as in water, $c_{\infty\alpha}/c_0 \approx 2$ and that this ratio is temperature independent. This showed that at difference with simple liquids where $c_{\infty\alpha}$ differs from c_0 by a few percent, the strengths of the structural relaxation process is much larger in HB liquid systems.

- The activation energy for the structural relaxation process, not only comes out to be associated with that of the H-bond, as previously observed in water [1], but it is strictly related to the number of H-bond to make and break more that to the strength of each bond. We found that the relation $E_{a-H_2O}/n_{HB-H_2O} \approx E_{a-HF}/n_{HB-HF}$ is fulfilled.

A comparison of our data with existing MD simulations [51] revealed a large difference between the measured $c_{\infty\alpha}$ and the calculated c_∞, implying the presence of a further relaxation, that we identify as the **microscopic** relaxation process.

- The strength of this process is such that in HF $c_{\infty\mu}/c_0 \approx 7$ and this value is compared to $c_{\infty\mu}/c_0 \approx 3$ in water. Since these ratios are larger than what found in simple monoatomic liquids, where $c_{\infty\mu}/c_0 \approx 1.2$ [5], we can conclude that the relative strengths of both the structural and microscopic relaxation processes seem to be larger in hydrogen bonded liquids.

- The comparison between BLS, IXS measurements and MD simulations, provides a strong indication that, similarly to simple and glass-forming liquids, also hydrogen bonded liquids present *two* relaxation processes affecting their high frequency collective dynamics.

The study of $(HF)_x(H_2O)_{1-x}$ solutions has helped to understand the evolution of the collective dynamics from the phenomenology of one liquid to that of the other. The main difference between the two liquids in fact, lies in the different HB arrangement: water is characterized by a tethraedral network with two hydrogen bonds for each molecule, while HF is organized in linear chains with one hydrogen bond per molecule. A preliminary analysis of the data in terms of the DHO model has shown a linear behaviour of the dispersion curves in the low Q region with slopes decreasing at increasing concentration of hydrogen fluoride. At higher concentration of HF the presence of the structural relaxation has been observed as a transition of the sound velocity from the low frequency limit to

the high frequency one and the ratio $c_{\infty\alpha}/c_0$ has been found almost independent on the concentration and close to two as the two limit cases. A more detailed analysis in term of the viscoelastic model supported the results found with the DHO model and gave further informations on the time scale of the $\alpha - relaxation$. A comparison between the two limit cases, water and HF, showed that in HF the structural relaxation is faster than in water being $\tau_{\alpha-H_2O}(Q \to 0)/\tau_{\alpha-HF}(Q \to 0) \approx 3$. This is attributed to higher the degree of freedom of the chain-like structure of HF respect to the three dimensional network of water.

The study of these two systems encourages the extention of our investigationsto other HB liquids. In particular, since an effort has been done to relate their main qualitative and quantitative differences to the particular arrangement of the hydrogen bond networks, it is tempting to consider systems with different number of HB per molecule, different strength of the bond and different geometries. This of course requires a large variety of HB systems to be investigated. In this respect measurements on liquid compounds of organic and inorganic nature as $HCOOH$ (formic acid) CH_3OH(methanol) have been planned.

Appendix1

HF sample cell drawings

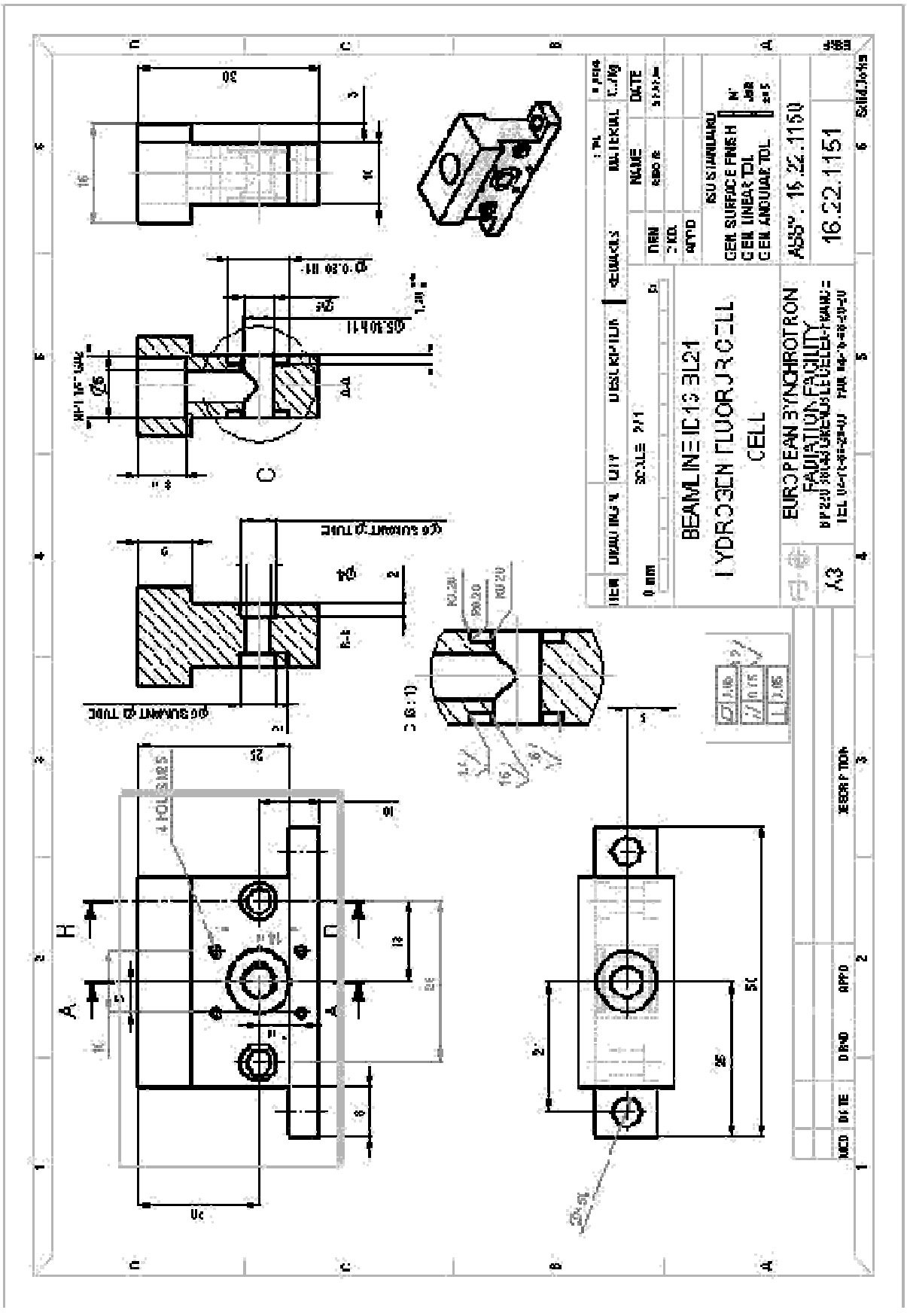
BEAMLINE IC13 3L21
HYDROGEN FLUORJROCELL
CELL
EUROPEAN SYNCHROTRON
RADIATION FACILITY
A3
16.22.1151
ASSY. 16.22.1160
DESCRIPTION
DRWD
APPD
DATE

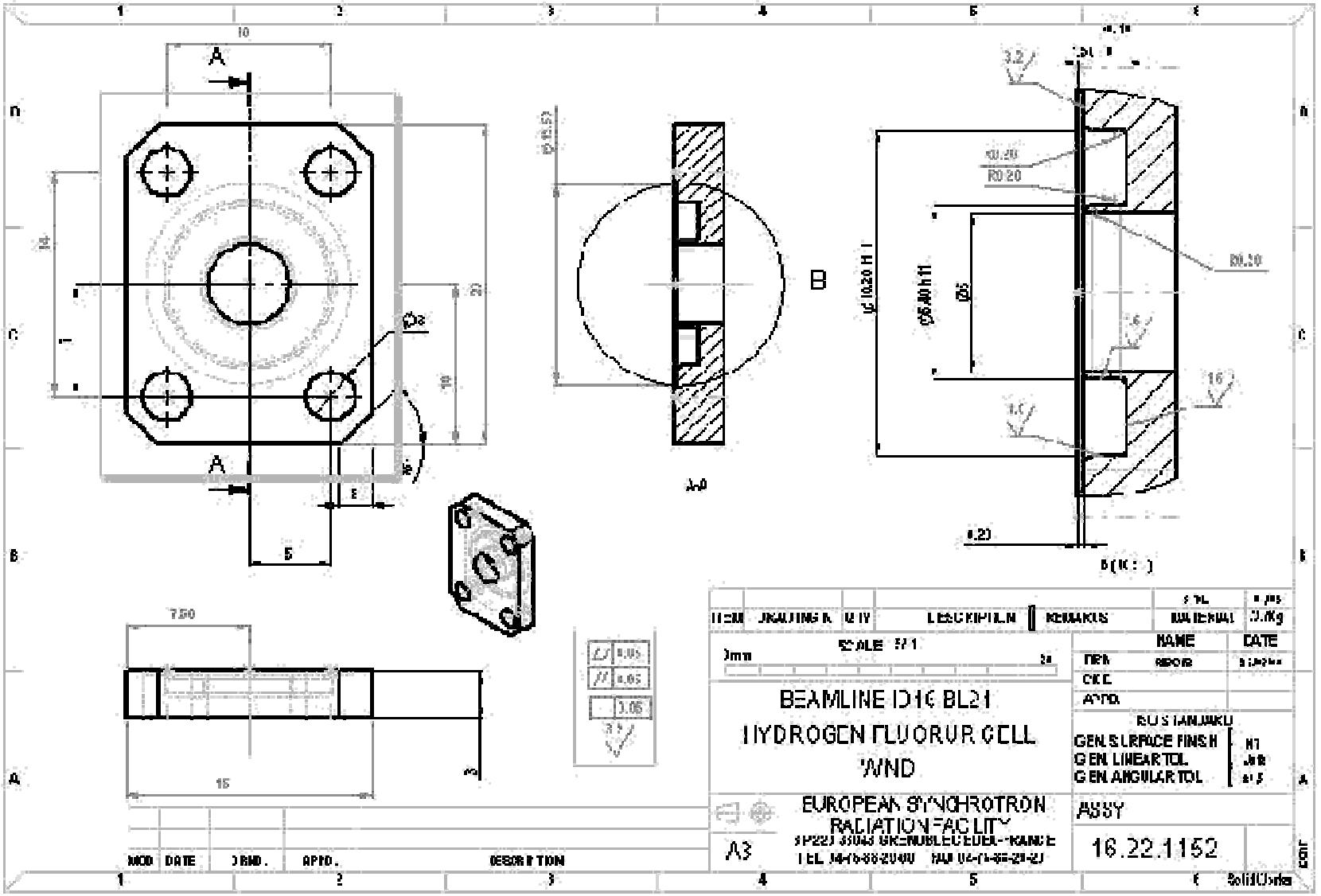
A
A
B
B
Ø8
Ø5
R0.20
R0.20
R0.20
3.2
1.6
16
6.20
5
7.50
15
3
BEAMLINE ID16 BL21
HYDROGEN FLUORUR CELL
MND
EUROPEAN SYNCHROTRON
RADIATION FACILITY
A3
ASSY
16.22.1152
SCALE 5/1
NAME
DATE
DES
CKD
APPD
GEN SURFACE FINISH
GEN LINEAR TOL
GEN ANGULAR TOL
ITEM
DRAWING NO
QTY
DESCRIPTION
REMARKS
MATERIAL
MOD
DATE
DRWD.
APPD.
DESCRIPTION

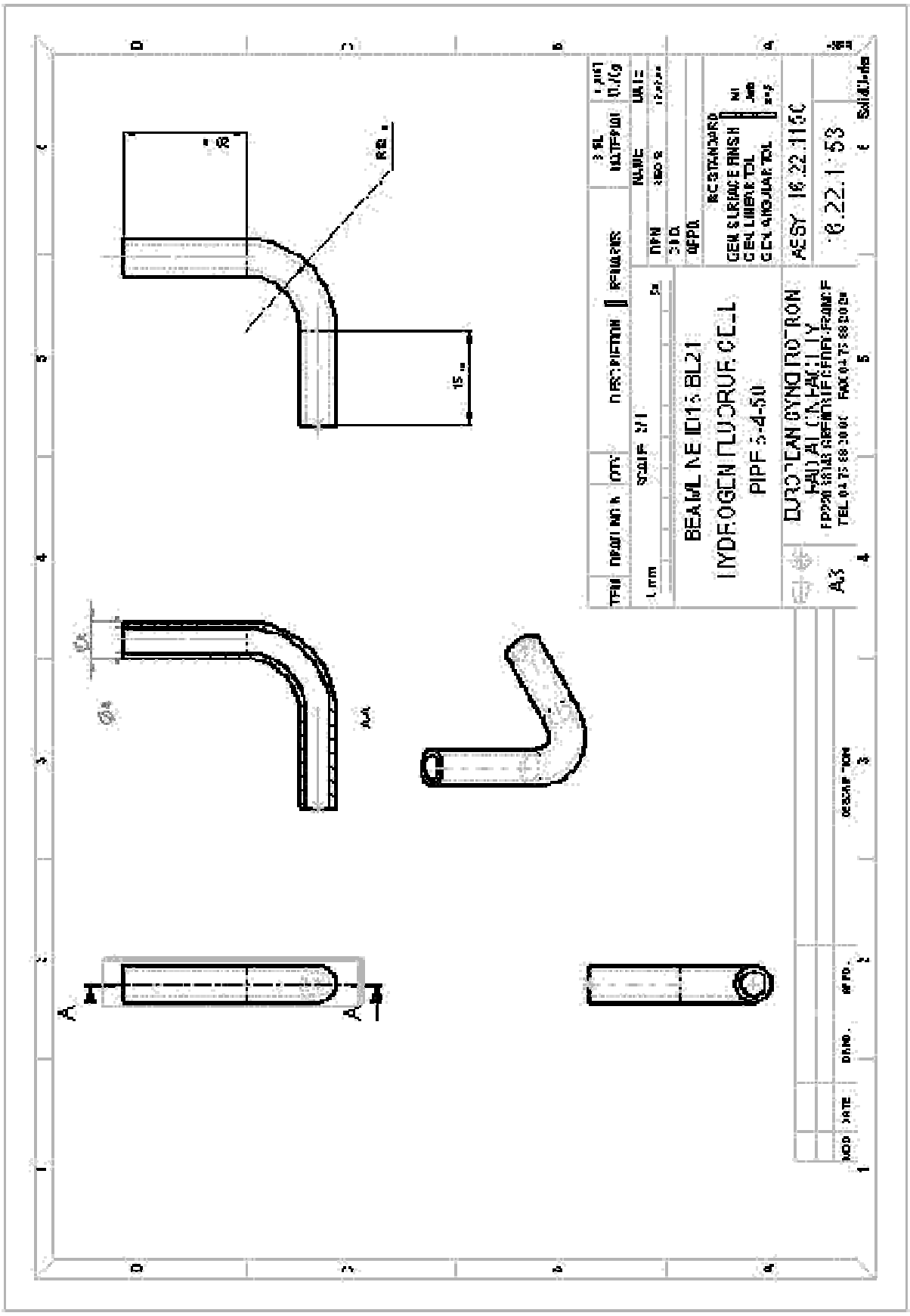
BEAMLINE ID16 BL21
HYDROGEN FLUORUF.CELL
PIPE 3-4-50
EUROPEAN SYNCHROTRON
A3
AESY 16.22.1150
16.22.1-53

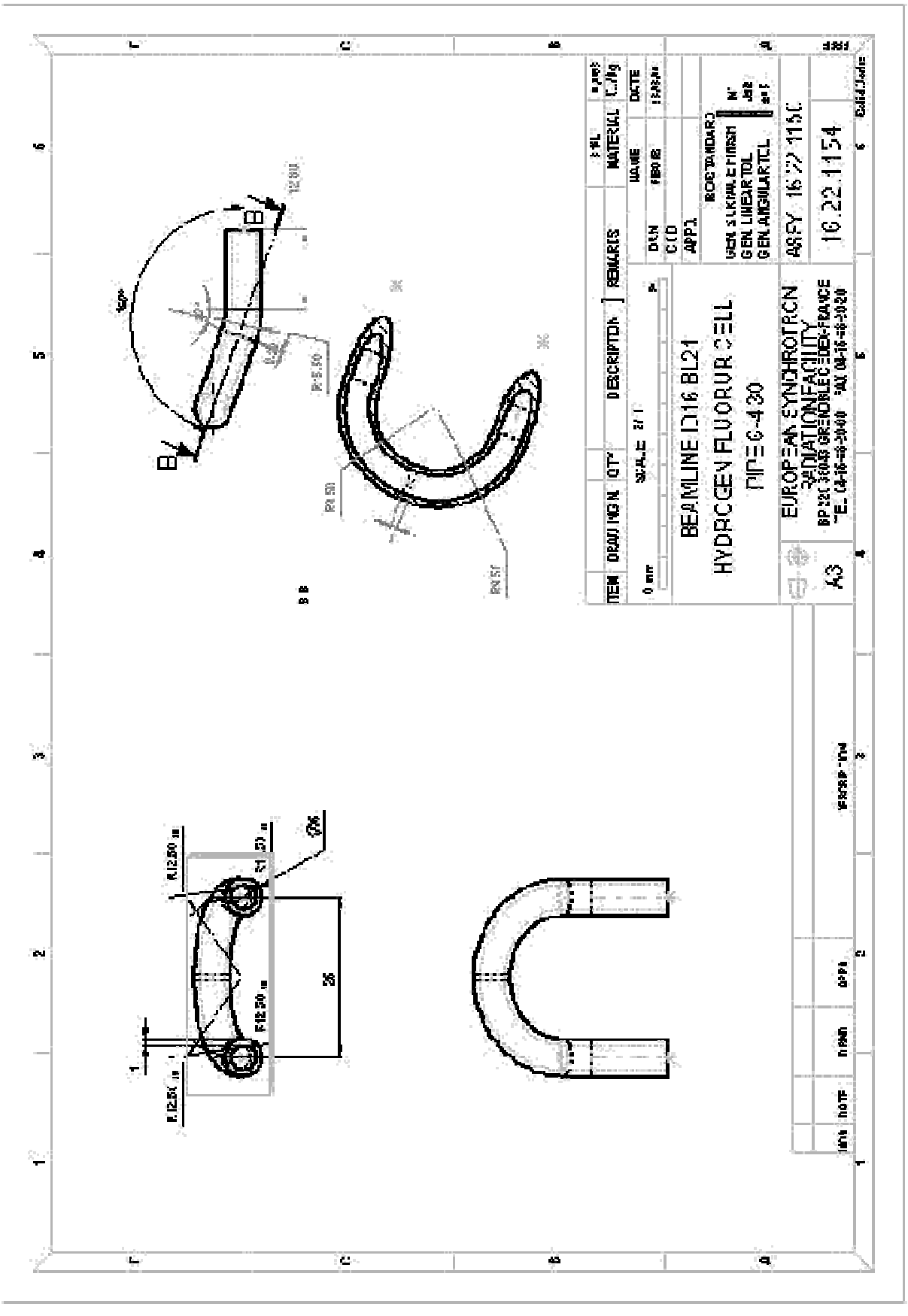
BEAMLINE ID16 BL21
HYDROGEN FLUORURE CELL
EUROPEAN SYNCHROTRON
RADIATION FACILITY
A3
16.22.1154
R12.50
R12.50
R12.50
R12.50
R15.50
R15.50
25
B
B

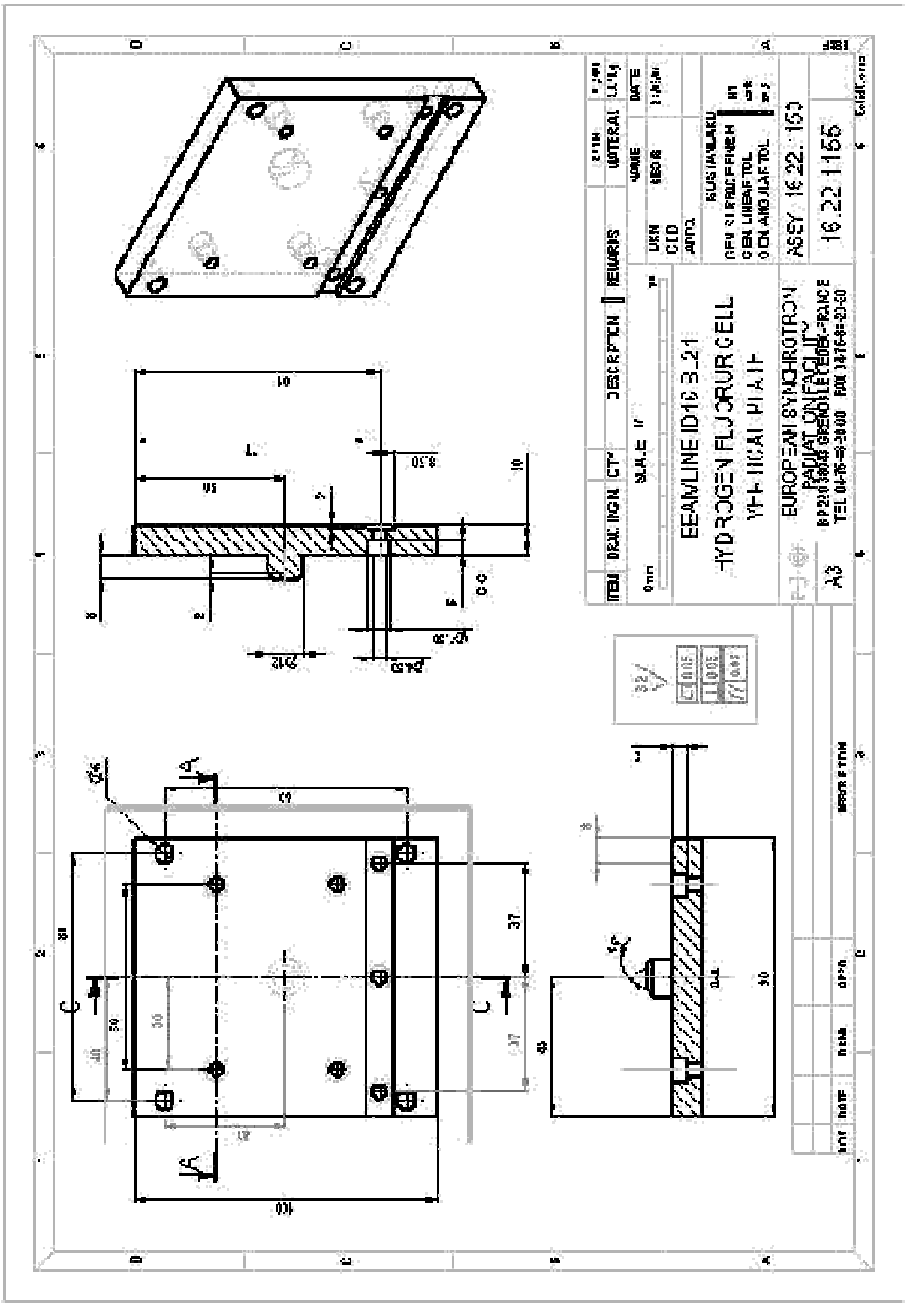
EUROPEAN SYNCHROTRON
RADIATION FACILITY
BP 220 38043 GRENOBLE CEDEX - FRANCE
TEL 04-76-88-20-00 FAX 04-76-88-20-20
ASSY 16.22.1155
16.22.1156
A3
BEAMLINE ID16.3_21
HYDROGEN FLUORURCELL
VERTICAL PLATE
DESCRIPTION
REMARKS
MATERIAL
DATE
SCALE
UNLESS OTHERWISE SPECIFIED
DIMENSIONS ARE IN MILLIMETERS
SURFACE FINISH
GENERAL LINEAR TOL
GENERAL ANGULAR TOL
100
37
30
50
A
B
C

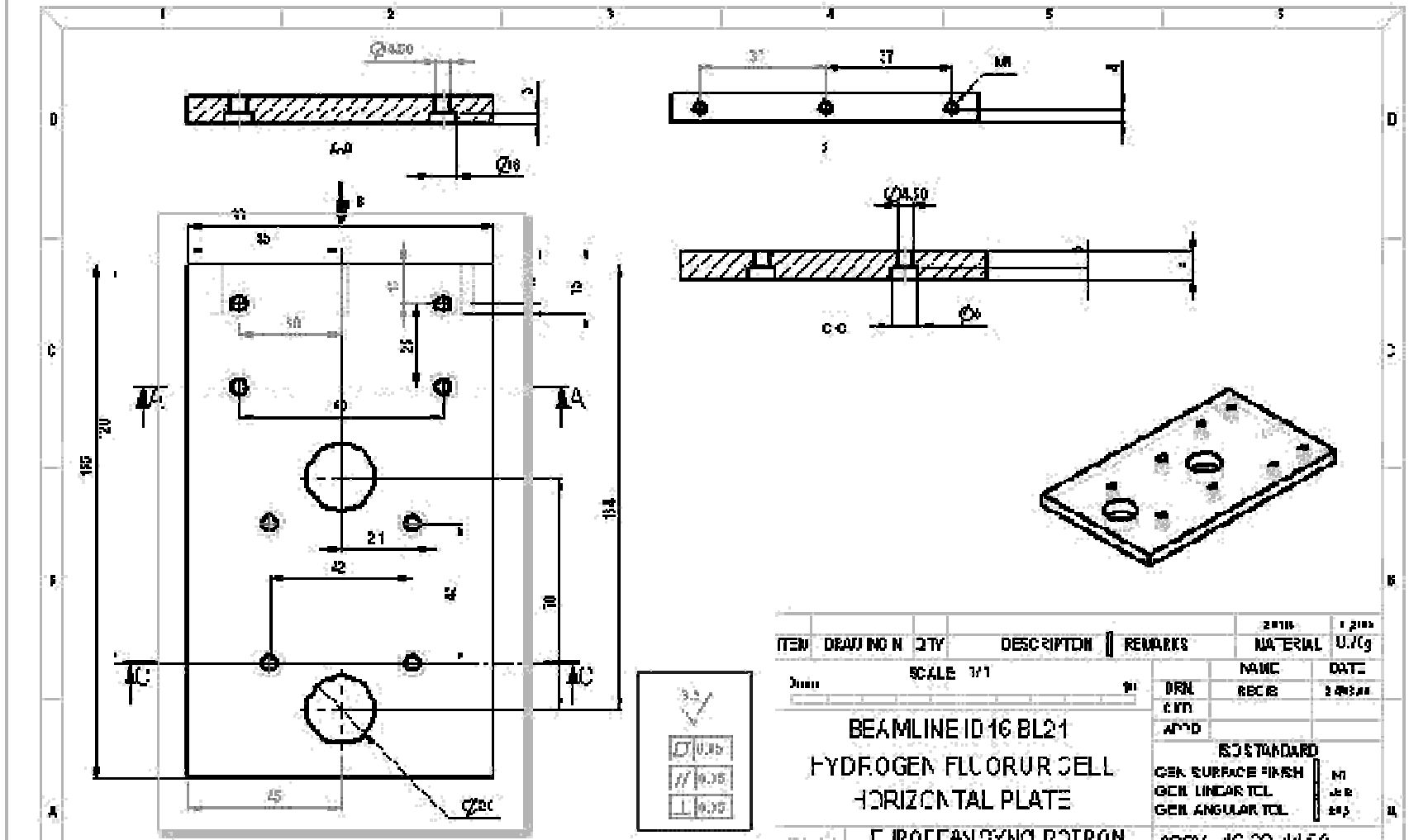
Ø4.50
Ø8
37
M8
C-C
Ø4.50
Ø8
35
10
25
21
42
45
Ø20
165
154
ITEM
DRAWING N
QTY
DESCRIPTION
REMARKS
MATERIAL
SCALE 1/1
BEAMLINE ID16 BL21
HYDROGEN FLUORUR CELL
HORIZONTAL PLATE
EUROPEAN SYNCHROTRON
RADIATION FACILITY
BP 220 38043 GRENOBLE CEDEX-FRANCE
NAME
DATE
DRN
CHK
APPD
ISO STANDARD
GEN. SURFACE FINISH
GEN. LINEAR TOL
GEN. ANGULAR TOL
ASSY. 16.22.1150
16.22.1156
AS

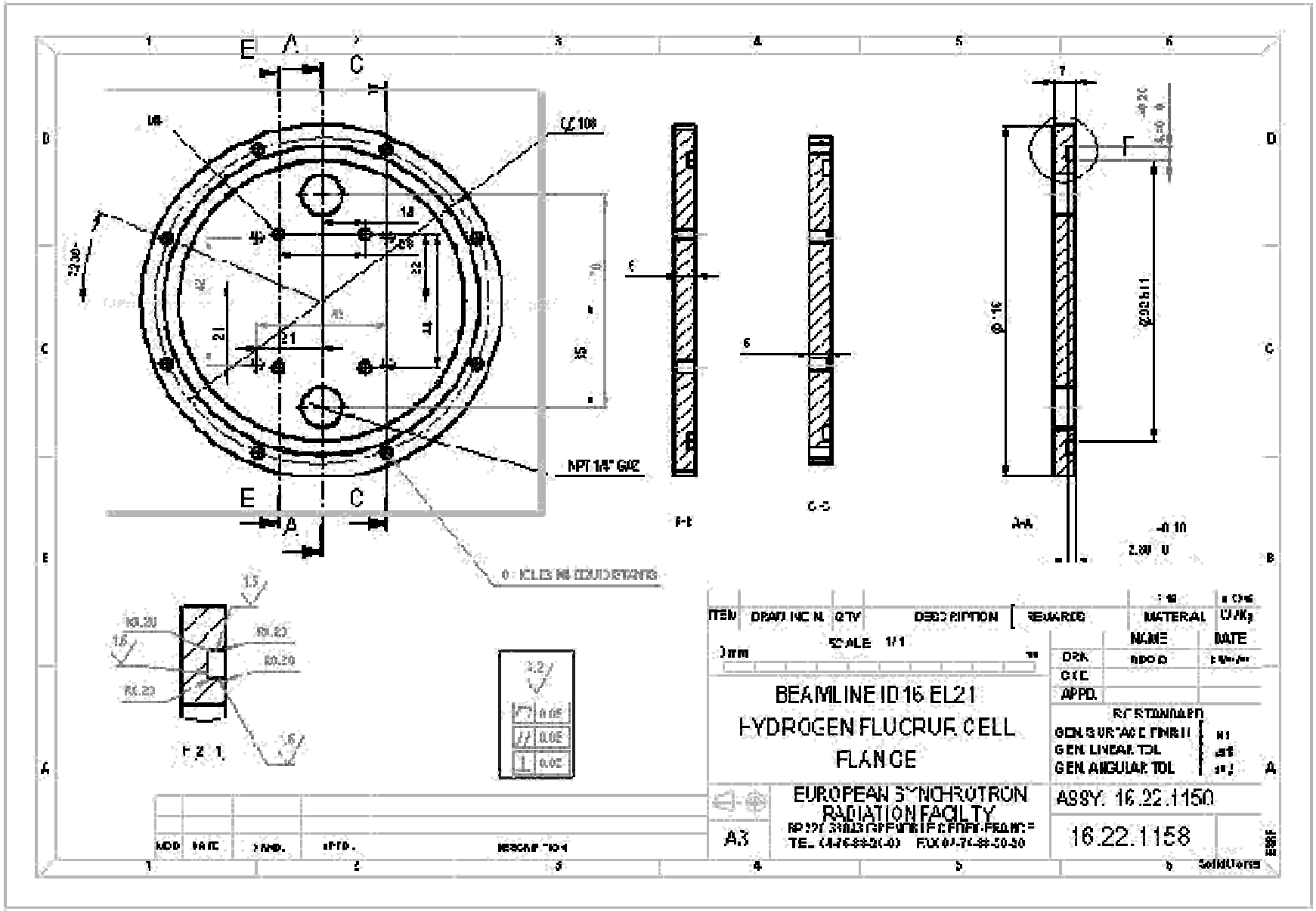
E
A
C
NPT 1/8" GAS
E
A
C
F
A-A
B-B
C-C
F 2 : 1
BEAMLINE ID16 EL21
HYDROGEN FLUCRUE CELL
FLANGE
EUROPEAN SYNCHROTRON
RADIATION FACILTY
A3
ASSY. 16.22.1150
16.22.1158
DRAWING N.
QTY
DESCRIPTION
REMARKS
MATERIAL
SCALE 1/1
NAME
DATE
DRN.
CKD.
APPD.
GEN. SURFACE FINISH
GEN. LINEAR TOL
GEN. ANGULAR TOL

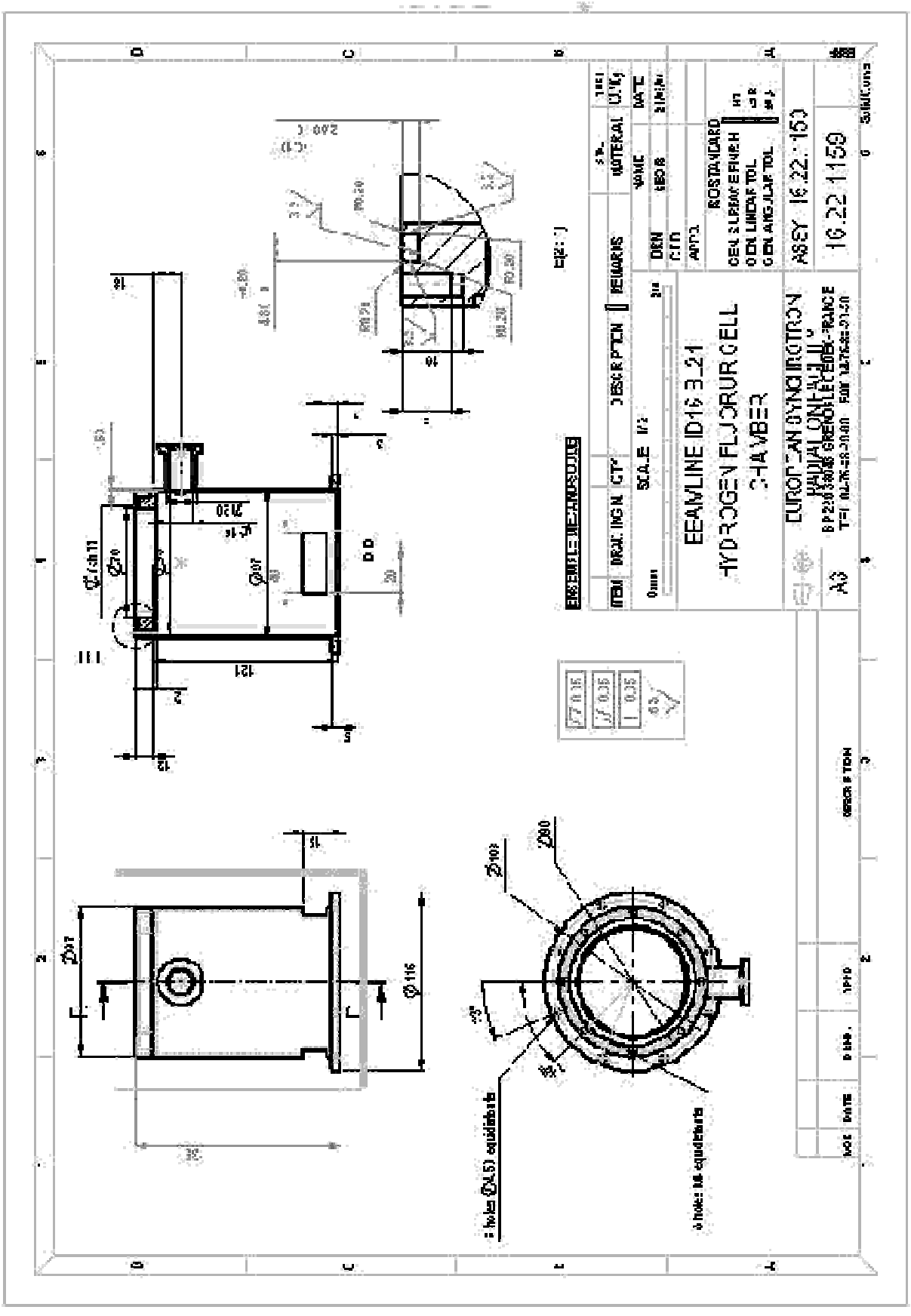
EBAWLINE ID16 3_21
HYDROGEN FLUORURGELL
CHAMBER
EUROPEAN SYNCHROTRON
ASSY 16.22.1150
16.22.1150
A3
ROSTANDARD
DESCRIPTION
REMARKS
MATERIAL
SCALE 1/2
DRAWING QTY
ITEM
EMBEDDED DIMENSIONS
121
Ø107
Ø116
Ø80
Ø100
Ø87
2 holes Ø4.5 equidistants
4 holes M6 equidistants

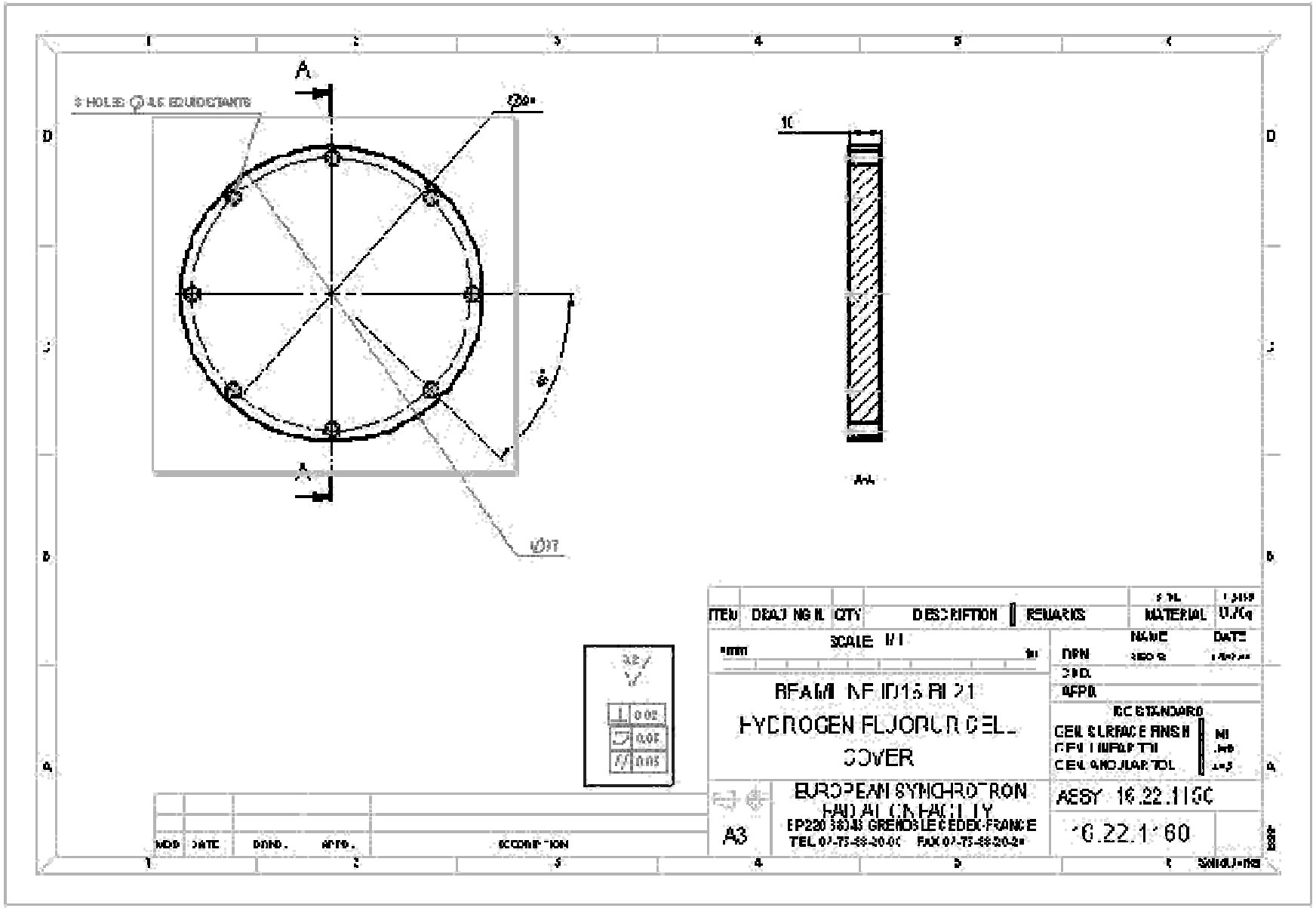
A
8 HOLES Ø 4.5 EQUIDISTANTS
Ø60
Ø77
A
10
A-A
ITEM
DRAWING N.
QTY
DESCRIPTION
REMARKS
MATERIAL
SCALE 1/1
mm
NAME
DATE
DRN
CHKD
APPD
BEAM INFLIGHT 21
HYDROGEN FLUORIDE CELL
COVER
EUROPEAN SYNCHROTRON
RADIATION FACILITY
A3
ASSY 16.22.1150
16.22.1160
MOD
DATE
DRWD.
APPD.
DESCRIPTION

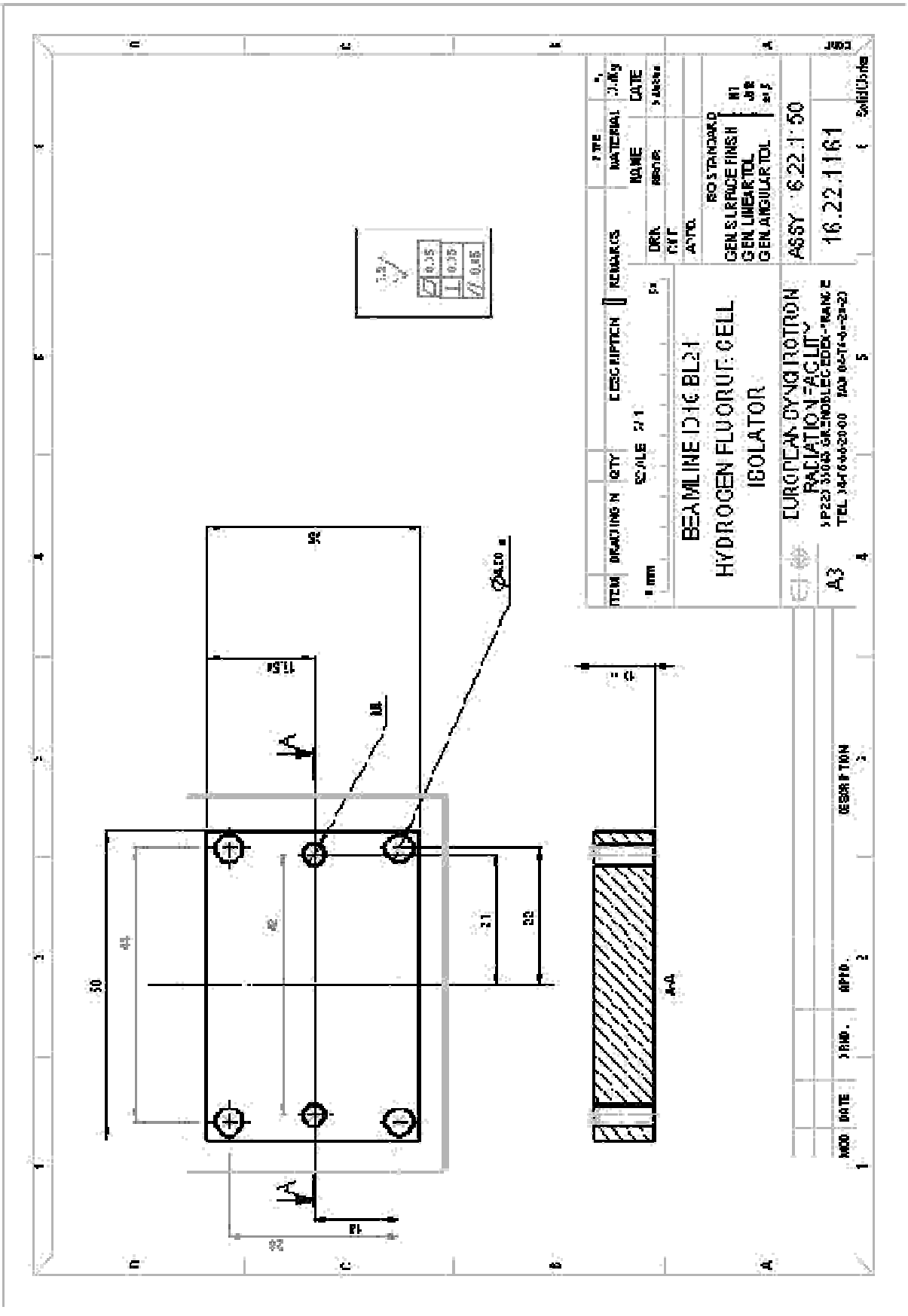
BEAMLINE ID16 BL21
HYDROGEN FLUORIDE CELL
ISOLATOR
EUROPEAN SYNCHROTRON
RADIATION FACILITY
A3
ASSY 6.22.1.50
16.22.1161
SCALE 2:1
50
43
40
21
23
Ø4.50
15.50
A-A

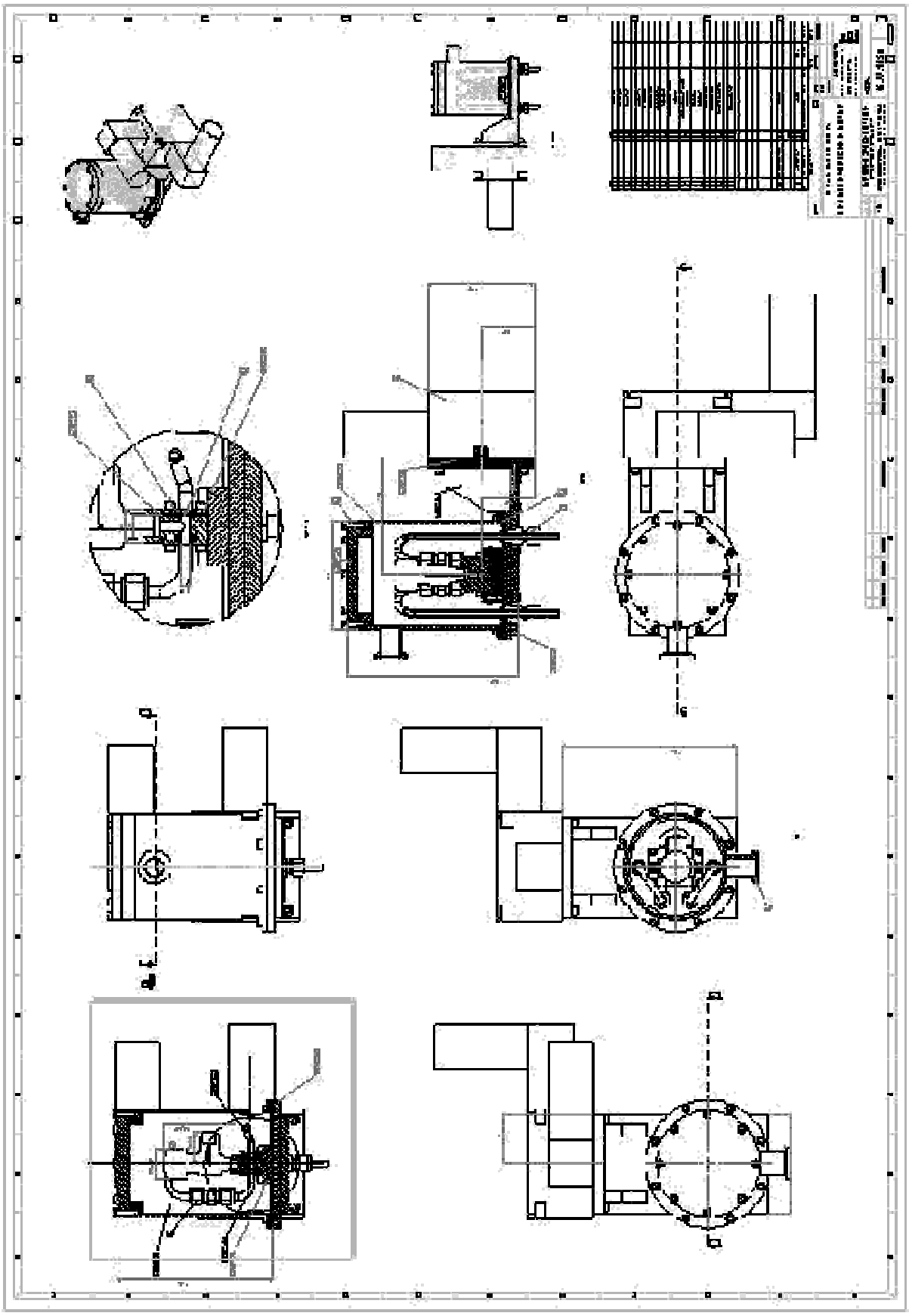

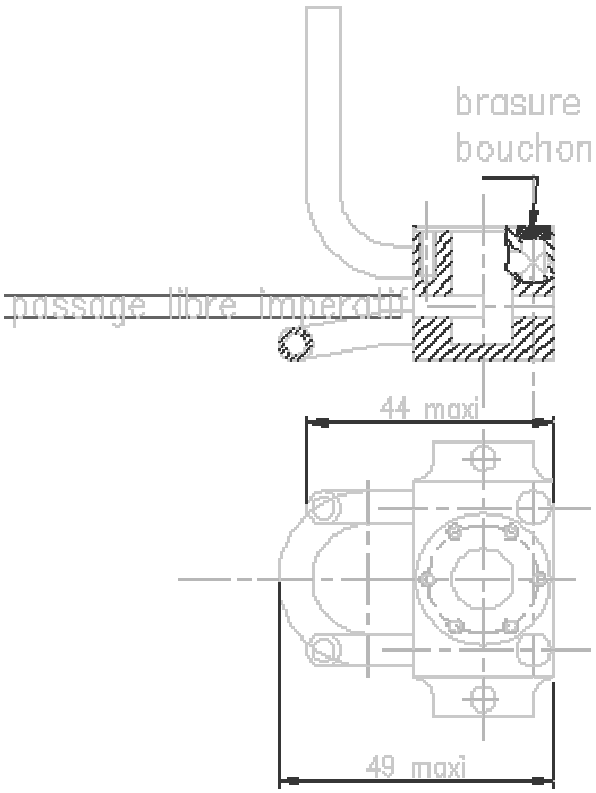

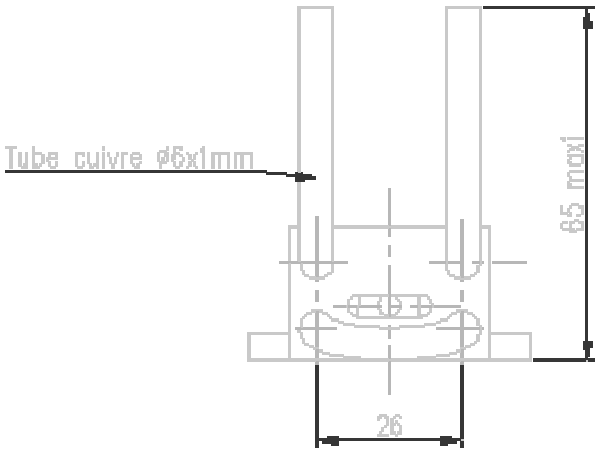

ITEM	DRAWING N.	QTY	DESCRIPTION / REMARKS	MATERIAL	W./kg

SCALE: 0mm

	NAME	DATE
DRN.	HENRIQUET	13.10.2000
CKD.		
APPD.		

CELLULE ACIDE FUORIDRIQUE

ISO STANDARD
GEN. SURFACE FINISH : N7
GEN. LINEAR TOL. : Js12
GEN. ANGULAR TOL. : ± 0.5°

EUROPEAN SYNCHROTRON RADIATION FACILITY
BP 220 38043 GRENOBLE CEDEX-FRANCE
TEL. 04-76-88-20-00 FAX. 04-76-88-20-20

ASSY.

A0

MOD	DATE/DRN.	CKD.	APPD.	DESCRIPTION
A				

AUTOCAD

Appendix2

$(HF)_x(H_2O)_{1-x}$ solutions sample cell drawings

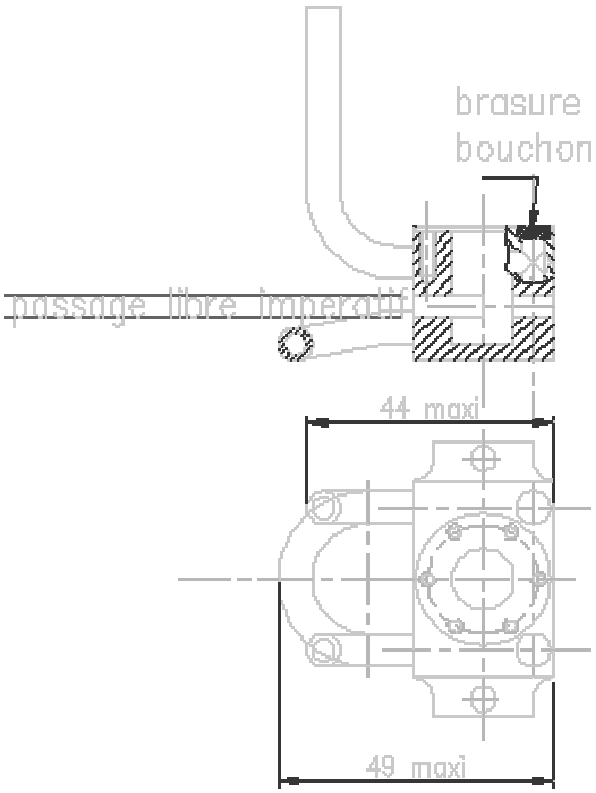

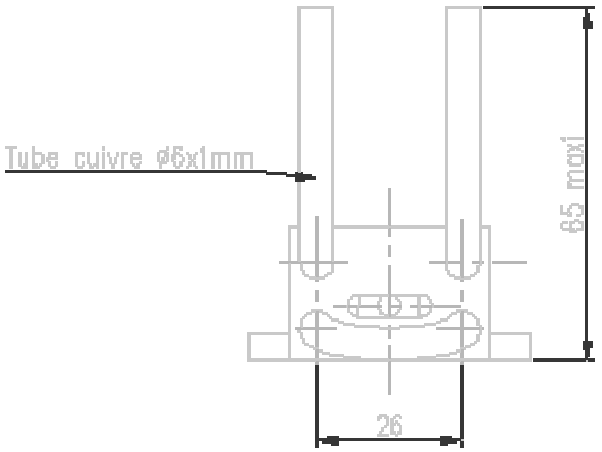

ITEM	DRAWING N.	QTY	DESCRIPTION / REMARKS	MATERIAL	W./Kg

SCALE: 0mm

	NAME	DATE
DRN.	HENRIQUET	13.10.2000
CKD.		
APPR.		

CELLULE ACIDE FUORIDRIQUE

ISO STANDARD
GEN. SURFACE FINISH : N7
GEN. LINEAR TOL. : Js12
GEN. ANGULAR TOL. : ± 0.5°

EUROPEAN SYNCHROTRON RADIATION FACILITY
BP 220 38043 GRENOBLE CEDEX-FRANCE
TEL. 04-76-88-20-00 FAX. 04-76-88-20-20

ASSY.

A0

MOD	DATE/DRN.	CKD.	APPD.	DESCRIPTION
A				

AUTOCAD

Bibliography

[1] G. Monaco, A. Cunsolo, G. Ruocco, and F. Sette. Viscoelastic behavior of water in the terahertz-frequency range: An inelastic x-ray scattering study. *Phys.Rev.E*, 60:5505, 1999.

[2] U. Balucani and M. Zoppi. *Dynamics of the Liquid State.* Clarendon Press - Oxford, 1994.

[3] A. Rahman. Density fluctuations in liquid rubidium.II.Molecular dynamics calculations. *Phys. Rev. A*, 9:1667, 1974.

[4] R. D. Mountain. Molecular-dynamics study of liquid rubidium. *Phys. Rev. A*, 26:2859, 1982.

[5] T. Scopigno, U. Balucani, G. Ruocco, and F. Sette. Density fluctuations in molten lithium: inelastic x-ray scattering study. *J. Phys.: Condens. Matter*, 12:8009, 2000. and references therein.

[6] W. Götze and M. R. Mayr. Evolution of vibrational excitations in glassy systems. *Phys. Rev. E*, 61:587, 2000.

[7] M. Blume. Magnetic scattering of x rays. *J. Appl. Phys.*, 57:3615, 1985.

[8] E. Burkel. *Inelastic Scattering of X-Rays with Very High Energy Resolution.* Springer Verlag - Berlin, Heidelberg, 1994.

[9] L. Van Hove. Correlations in space and time and Born approximation scattering in systems of interacting particles. *J. Appl. Phys.*, 95:249, 1954.

[10] H. Zachariasen. *Theory of X-Rays Diffraction in Crystals.* Dover - New York, 1944.

[11] M. Deutsch and M. Hart. Electronic charge distribution in silicon. *Phys. Rev. B*, 31:3846, 1985.

[12] M. Deutsch, M. Hart, and P. Sommer-Larsen. Thermal motion of atoms in crystalline silicon: beyond the Debye theory. *Phys. Rev. B*, 40:11666, 1989.

[13] V. E. Bottom. *A. Accad. Brasileira Ciencias*, 37:407, 1965.

[14] H. Maier-Leibniz. *Nucleonik*, 8:61, 1966.

[15] R. Verbeni. *Study of the collective excitations in super-critical ^4He and ^3He by using the inelastic x-ray scattering technique with meV energy resolution.* PhD thesis, Universitè Joseph Fourier, 1998.

[16] A. Caticha and S. Caticha-Ellis. Dynamical theory of x-ray diffraction at Bragg angles near $\pi/2$. *Phys. Rev. B*, 25:971, 1982.

[17] O. Brummer, H.R. H$\dot{}\cdot\cdot$oke, and J. Nieber. X-ray diffraction in the Bragg case at Bragg angles of about $\pi/2$. *Phys. Status Solidi A*, 53:565, 1979.

[18] W. Graeff and G. Materlik. Millielectronvolt energy resolution in Bragg backscattering. *Nuclear Inst. and Meth.*, 195:97, 1982.

[19] H. Ibach. Thermal expansion of silicon and and zinc oxide (I). *Phys. Status Solidi*, 31:625, 1969.

[20] G. Brown and W. Lavender. *Handbook of Synchrotron Radiation.* North Holland, 1991.

[21] C. Masciovecchio. *The inelastic X-ray scattering as a new technique to investigate the dynamics of glass-forming systems.* PhD thesis, Universitè Joseph Fourier, 1998.

[22] C. Masciovecchio, U. Bergmann, M. Krisch, G. Ruocco, F. Sette, and R. Verbeni. A perfect crystal X-ray analyser with 1.5 meV energy resolution. *Nucl. Instrum. Methods Phys. Res. B*, 117:339, 1996.

[23] C. Masciovecchio, U. Bergmann, M. Krisch, G. Ruocco, F. Sette, and R. Verbeni. A perfect crystal X-ray analyser with meV energy resolution. *Nucl. Instrum. Methods Phys. Res. B*, 111:181, 1996.

[24] C. Masciovecchio, U. Bergmann, M. Krisch, G. Ruocco, F. Sette, and R. Verbeni. A perfect crystal x-ray analyser with mev energy resolution. *Nucl. Instr. and Meth. in Phys. Res. B*, 111:181, 1996.

[25] C. Masciovecchio, U. Bergmann, M. Krisch, G. Ruocco, F. Sette, and R. Verbeni. A perfect crystal x-ray analyser with 1.5 mev energy resolution. *Nucl. Instr.and Meth. in Phys. Res. B*, 117:339, 1996.

[26] P. A. Egelstaff. *An introduction to the Liquid State.* Clarendon Press - Oxford.

[27] B. J. Berne and R. Pecora. *Dynamic Light Scattering.* John Wiley Sons Inc. - New York USA, 1940.

[28] G. Harrison. *The Dynamic Properties of Supercooled Liquid.* Academic Press - London, New York, San Francisco, 1976.

[29] J. P. Boon and S. Yip. *Molecular Hydrodynamics.* Dover Publications Inc.- New York USA, 1980.

[30] R. D. Mountain. Thermal relaxation and Brillouin scattering in liquids. *J. Res. Natl. Bu. Soc.*, 70A:207, 1966.

[31] T. Bodensteiner. PhD thesis, Technische Universitüt, München, Germany, 1990.

[32] U. Balucani and M. Zoppi. *Dynamics of the Liquid State.* Clarendon Press - Oxford, 1994.

[33] W. M. Latimer and W. H. Rodebush. Polarity and ionization from the standpoint of the lewis theory of valence. *J. Am. Chem. Soc.*, 42:1419, 1920.

[34] L. Pauling. The nature of chemical bond.IV.The energy of single bonds and relative electronegativity of atoms. *J. Am. Chem. Soc.*, 54:3570, 1932.

[35] L. Pauling. *The nature of the chemical bond.* Cornell University Press - Ithaca USA, 1939.

[36] A. Rahman and F. H. Stillinger. Propagation of sound in water. A molecular dynamic study. *Phys. Rev. A*, 10:368, 1974.

[37] J. Texeira, M. C. Bellisent-Funel, S. H. Chen, and B. Dorner. Observation of new short-wavelength collective excitations in heavy water by coherent inelastic neutron scattering. *Phys. Rev. Lett.*, 54:2681, 1985.

[38] F. Sette, G. Ruocco, M. Krisch, C. Masciovecchio, R. Verbeni, and U. Bergmann. Transition from normal to fast sound in liquid water. *Phys. Rev. Lett.*, 77:83, 1996.

[39] R. Verbeni, F. Sette, M. H. Krisck, U. Bergmann, B. Gorges, C. Halcoussis, K. Martel, C. Masciovecchio, J. F. Ribois, G. Ruocco, and H. Sinn. X-ray monochromator with 2×10^{-8} energy resolution. *J. Synchrotron Rad.*, 3:62, 1996.

[40] A. Cunsolo, G. Ruocco, F. Sette, C. Masciovecchio, A. Mermet, G. Monaco, M. Sampoli, and R. Verbeni. Experimental determination of the structural relaxation in liquid water. *Phys. Rev. Lett.*, 82:775, 1999.

[41] Götze. *Liquids, Freezing and Glass Transition*, pages 287–503. North Holland - Amsterdam, Oxford, New York, Tokio, 1991.

[42] M. Sampoli, G. Ruocco, and F. Sette. Mixing of longitudinal and transverse dynamics in liquid water. *Phys. Rev. Lett.*, 79:1678, 1997.

[43] U. Balucani, G. Ruocco, A. Torcini, and R. Vallauri. Fast sound in liquid water. *Phys.Rev. E*, 47:1677, 1993.

[44] www.mesalabs.com/nusonics/hydrofluoricacidanalyzerappli.shtml.

[45] Landolt-Boernestein. *Numerical Data and Functional Relationships in Science and Thecnology.* Springer Verlag - Berlin Germany, 1998.

[46] R. Angelini. *et al*, to be published.

[47] D. R. Lide. *Handbook of Chemistry and Physics - 79th edition.* CCR Press - Boca Raton USA, 1998.

[48] P.G. De Gennes. Liquid dynamics and inelastic scattering of neutrons. *Physica*, 25:825, 1959.

[49] B. Fak and B. Dorner, 1992. Institute Laue Langevin (Grenoble, France) Technical Report ILL 92FA008S1992.

[50] R. Angelini. *et al*, to be published.

[51] D. Bertolini, G. Sutmann, A. Tani, and R. Vallauri. Viscous versus elastic response of hydrogen-bonded liquids: collective dynamics in HF. *Phys. Rev. Lett.*, 81:2080, 1998.

[52] U. Balucani, D. Bertolini, A. Tani, and R. Vallauri. Transport properties of liquid hydrogen fluoride. *J. Chem. Phys.*, 112:9025, 2000.

[53] G. Garberoglio and R. Vallauri. Istantaneous normal mode analysis of liquid HF. *Phys. Rev. Lett.*, 84:4878, 2000.

[54] C. J. Montrose, J. A. Bucaro, J. Marshall-Croakley, and T. A. Litovitz. Depolaraized Rayleigh scattering and hydrogen bonding in liquid water. *J. Chem. Phys.*, 60:5025, 1974.

[55] F.J. Bermejo, F. Batallan, J.L. Martinez, M. Garcia-Hernandez, and E. Enciso. Collective excitations in liquid methanol studied by coherent inelastic neutron scattering. *J. Phys.: Condens. Matter*, 2:6659, 1990.

[56] A. Sillanpää, C. Simon, M.L. Klein, and K. Laasonen. Structural and spectral properties of aqueous hydrogen fluoride studied using ab initio molecular dynamics. *J. Phys.Chem. B*, 106:11315, 2002.

[57] K.Laasonen and M.L. Klein. Ab initio dynamics study of dilute hydrofluoric acid. *Mol. Phys.*, 88:135, 1995.

[58] L.Andrews and G.L. Johnson. FTIR spectra of water-hydrogen fluoride complexes in solid argon. evidence for inversion doubling in the HF librational mode of H_2O–HF. *J. Chem. Phys.*, 79:3670, 1983.

[59] V.D. Mootz, U. Ohms, and W. Poll. Schmelzdiagramm H_2O-HF und strukturen der 1:1 und 1:2-phase. *Z. Anorg. Allg. Chem.*, 479:75, 1981.

[60] P. A. Giguère and S. Turrel. The nature of hydrofluoric acid. A spectrocopic study of the proton-transfer complex $H_3O^+ \cdot F^-$. *J. Am. Chem. Soc.*, 102:5473, 1980.

[61] P. A. Giguère. Ion pair and strength of hydrofluoric acid. *Chem. Phys. Lett.*, 41:598, 1976.

[62] R. Férnandez-Perea, M. Alvarez, F. J. Bermejo, P. Verkerk, B. Roessli, and E. Enciso. Collective ionic dynamics in a molten binary alloy. *Phys. Rev. E.*, 58:4568, 1998.

[63] N. Anento and J. A. Padrò. Longitudinal collective modes in simple liquid binary alloys: A computer simulation study. *Phys. Rev. E.*, 62:1142, 1998.

[64] E. Enciso, N. G. Almarza, P. Dominguez, M. A. González, and F. J. Bermejo. Dynamic structure factor of a helium-neon dense gas mixture: Crossover from Hydrodynamics to microscopic regime. *Phys. Rev. Lett.*, 74:4233, 1995.

[65] A. Mukherjee, G. Srinivas, and B. Bagchi. Reentrant behavior of relaxation time with viscosity at varying composition in binary mixtures. *Phys. Rev. Lett.*, 86:5926, 2001.

[66] G. Srinivas, A. Mukherjee., and B. Bagchi. Nonideality in the composition dependence of viscosity in binary mixtures. *J. Chem. Phys.*, 114:6220, 2001.

[67] F. W. Starr, J. K. Nielsen, and H. E. Stanley. Fast and slow dynamics of hydrogen bonds in liquid water. *Phys. Rev. Lett.*, 82:2294, 1999.

[68] S. Chowdhuri and A. Chandra. hydrogen bonds in aqueous electrolyte solutions: Statistics and dynamics based on both geometric and energetic criteria. *Phys. Rev. E*, 66:041203, 2002.

Acknowledgements

I would like to acknowledge Dr. Francesco Sette, my scientific supervisor at the E.S.R.F. to have followed my thesis work. He gave me the possibility to learn and deepen everything about the inelastic x rays scattering technique from both experimental and theoretical point of view. I appreciated his scientific rigor and his dedication to work. At the same time I want to thank Prof. Giancarlo Ruocco from the University "La Sapienza" of Roma who introduced me to the inelastic scattering technique in the light scattering laboratory of University of L'Aquila and with whom I have continuously been in contact during all my stay in Grenoble. He gave me the possibility to meet Francesco Sette and his group.

I am very grateful to:

Dr. Paola Giura for the daily scientific discussions we had in the office we shared for more than two years. She arrived in the inelastic x ray scattering group nine months after me. We immediately discovered a working affinity and we started to collaborate.

Dr. Giulio Monaco who showed always much interest in my work, he gave me many suggestions and continuous scientific stimulations during this period.

Dr. Roberto Verbeni, Christian Henriquet and Christoph Lapras who solved any kind of technical problem related to the beamline and the experimental set-ups. They have always looked for and found the best solutions to guarantee the highest performances.

I acknowledge also Dr. Daniele Fioretto from the University of Perugia with whom I performed the light scattering measurements presented in this thesis and Dr. Harald Muller for useful suggestions and for his assistance during the sample preparation.

Particular thanks go to Prof. Christiane Alba-Simionesco from LCP of University of Paris and Prof. Gabriele Viliani from the University of Trento, the referees of my thesis, for the critical reading of the manuscript ; Prof. Jean Francois Legrand from the CEA of Grenoble who has been my thesis' director at the University of Grenoble and Prof. Marie Claire Bellisent-Funel from LLB CEA-Saclay, who has accepted to be member of the jury.

Finally I'm grateful to Dr. Barbara Ruzicka for the support in the very last days before the thesis defense and to all those persons (many friends) who encouraged me in this work.

Roberta Angelini